

1991

**Coincidence analyzing -power measurements of the reaction  
carbon(polarized proton,proton',photon)excited carbon through  
the 15.11 MeV state**

Christopher Robinson Lyndon  
*College of William & Mary - Arts & Sciences*

Follow this and additional works at: <https://scholarworks.wm.edu/etd>

---

**Recommended Citation**

Lyndon, Christopher Robinson, "Coincidence analyzing -power measurements of the reaction carbon(polarized proton,proton',photon)excited carbon through the 15.11 MeV state" (1991). *Dissertations, Theses, and Masters Projects*. William & Mary. Paper 1539623799. <https://dx.doi.org/doi:10.21220/s2-34jb-q712>

This Dissertation is brought to you for free and open access by the Theses, Dissertations, & Master Projects at W&M ScholarWorks. It has been accepted for inclusion in Dissertations, Theses, and Masters Projects by an authorized administrator of W&M ScholarWorks. For more information, please contact [scholarworks@wm.edu](mailto:scholarworks@wm.edu).

## INFORMATION TO USERS

This manuscript has been reproduced from the microfilm master. UMI films the text directly from the original or copy submitted. Thus, some thesis and dissertation copies are in typewriter face, while others may be from any type of computer printer.

**The quality of this reproduction is dependent upon the quality of the copy submitted.** Broken or indistinct print, colored or poor quality illustrations and photographs, print bleedthrough, substandard margins, and improper alignment can adversely affect reproduction.

In the unlikely event that the author did not send UMI a complete manuscript and there are missing pages, these will be noted. Also, if unauthorized copyright material had to be removed, a note will indicate the deletion.

Oversize materials (e.g., maps, drawings, charts) are reproduced by sectioning the original, beginning at the upper left-hand corner and continuing from left to right in equal sections with small overlaps. Each original is also photographed in one exposure and is included in reduced form at the back of the book.

Photographs included in the original manuscript have been reproduced xerographically in this copy. Higher quality 6" x 9" black and white photographic prints are available for any photographs or illustrations appearing in this copy for an additional charge. Contact UMI directly to order.

# U·M·I

University Microfilms International  
A Bell & Howell Information Company  
300 North Zeeb Road, Ann Arbor, MI 48106-1346 USA  
313/761-4700 800/521-0600



**Order Number 9127113**

**Coincidence analyzing-power measurements of the reaction <sup>12</sup>  
 $C(\bar{p}, p' \gamma)^{12}C^*$  through the 15.11 MeV state**

**Lyndon, Christopher Robinson, Ph.D.**

**The College of William and Mary, 1991**

**U·M·I**  
300 N. Zeeb Rd.  
Ann Arbor, MI 48106



COINCIDENCE ANALYZING-POWER MEASUREMENTS  
OF THE REACTION  $^{12}\text{C}(\bar{p}, p'\gamma)^{12}\text{C}^*$   
THROUGH THE 15.11 MEV STATE

---

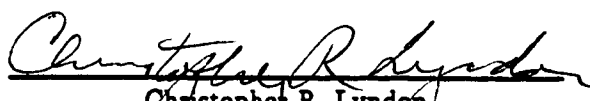
A Dissertation  
Presented to  
The Faculty of the Physics Department  
The College of William and Mary in Virginia

in Partial Fulfillment  
of the Requirements for the Degree of  
Doctor of Philosophy

---

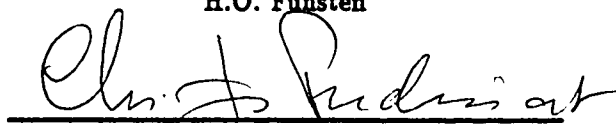
by  
Christopher R. Lyndon  
March 1991

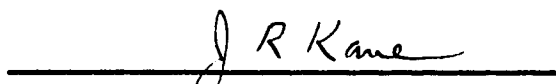
This dissertation is submitted in partial fulfillment of  
the requirements for the degree of  
Doctor of Philosophy

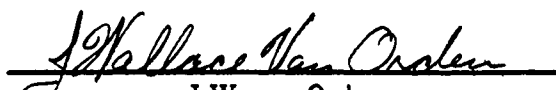
  
Christopher R. Lyndon

Approved, March 1991

  
H.O. Funsten

  
C.F. Perdrisat

  
J.R. Kane

  
J.W. van Orden  
CEBAF

  
R.L. Kiefer  
Dept. of Chemistry

## Table of Contents

Acknowledgements . . . . .	vi
List of Tables . . . . .	viii
List of Figures . . . . .	ix
Abstract . . . . .	xiii
1 Introduction . . . . .	2
2 Theoretical Background . . . . .	7
2.1 Derivation of the Coincidence Observables from the Singles Amplitudes . . . . .	8
2.2 Nonrelativistic DWIA Calculation . . . . .	12
2.3 Relativistic DWIA Calculation . . . . .	15
3 Experimental Set-up . . . . .	17
3.1 Detectors . . . . .	17
3.1.1 Scattered Proton Detection . . . . .	20
3.1.2 $\gamma$ -ray Detection . . . . .	24
3.1.3 Polarization and Beam Current . . . . .	24
3.2 Data Acquisition . . . . .	26
3.3 Electronics . . . . .	26
3.4 Calibration of the BGO Energy Spectra . . . . .	27
4 Data Analysis . . . . .	32
4.1 Data Analysis Hardware and Software . . . . .	32
4.2 Coincidence Analyzing Powers of $^{12}\text{C}(p, p' \gamma)^{12}\text{C}^*(15.11 \text{ MeV})$ . . . . .	33

4.2.1	Polarization . . . . .	34
4.2.2	Beam Current Correction and Scalers . . . . .	34
4.2.3	Measurement of the 15.11-MeV Peaks . . . . .	41
4.2.3.1	Doppler Correction . . . . .	42
4.2.3.2	Temperature Corrections . . . . .	43
4.2.3.3	S2 Timing Cuts . . . . .	44
4.2.3.4	Plastic Scintillator Pulse-height Information . . . . .	48
4.2.3.5	BGO Timing . . . . .	51
4.2.3.6	Pile-up . . . . .	55
4.2.3.7	Random Background Subtraction . . . . .	58
4.2.3.8	Background Identification . . . . .	59
4.2.3.9	Use of EGS4 to Find the 15.11-MeV Peak Amplitudes . . . . .	68
4.2.4	Uncertainty Analysis . . . . .	77
4.2.5	The Angular Correlation Function $W(\theta)$ and the 4.44-MeV State . . . . .	79
5	Results and Conclusions . . . . .	82
5.1	Presentation of the Results . . . . .	82
5.2	Parity Constraints . . . . .	87
5.3	Discussion of the Results . . . . .	88
5.4	Use of Symmetries to Combine Data . . . . .	95
5.5	Conclusion . . . . .	98
A	Evaluation of the Polarization Averaging Approximation . . . . .	101
B	The Monte Carlo Program BGOPI0MC . . . . .	103
C	The Monte Carlo Program NEUPNAD . . . . .	109
D	Tables of Asymmetries Measured . . . . .	114

<b>References . . . . .</b>	<b>117</b>
<b>VITA . . . . .</b>	<b>120</b>

## Acknowledgements

I would like to express thanks and appreciation toward those who made this work possible:

To my advisor Dr. Herbert Funsten, who initiated this experiment, for affording me the opportunity to take part in this project and thereby to learn what I have of physics and experimental science these past few years, and for his patience, guidance and instruction;

To Dr. Charles Perdrisat for his willingness to be available for help and for his many contributions to this project;

To Dr. J. Wallace Van Orden, Dr. John Kane, and Dr. Richard Kiefer for reading the manuscript and being on the PhD. committee;

To those who participated in the experimental runs, and especially to Dr. B.J. Lieb and John Mackenzie who made such substantial contributions;

To Dr. John Bensei, Melvin Woods, and Dr. Guo Fu Chen, who constructed the scintillator detectors;

To Dr. Michael McNaughton for his help during the experiment, and the staff at LAMPF especially Ron Richardson and others at LEEP;

To Dr. Rob Whyley for his help in the early stages of data analysis;

To Dr. Jorge Piekarewicz for supplying the theoretical amplitudes and the codes for calculating the observables, and also for his helpfulness in conversations about the theory;

To those who read and offered comments and suggestions on the paper written about this project, especially Dr. Joseph Comfort, Dr. Hans Plendl

and Dr. Carey Stronach;

To my good friend Dr. Rahman Pourang for all his help, especially with the graphics quality of this document;

To my friends presently and formerly students in the Physics Department of William & Mary, especially Dr. Chengwei Sun and Yohanes Surya;

To my friends associated with Williamsburg New Testament Church, for their encouragement, prayers, and support, and especially to Matilda Hawk;

To my family, especially to my mother; and to my father, who encouraged me to learn about physics;

And finally to the Lord, who framed all the laws of nature that we are trying to discover (but who strangely is seldom<sup>1</sup> acknowledged in the literature), and who enabled me to complete this task.

This work was supported in part by the National Science Foundation.

---

<sup>1</sup>but see, for example, [Gol80], x.

**List of Tables**

<b>3-1</b>	<b>BGO angles relative to beam direction and distances from the front face to the target center. . . . .</b>	<b>21</b>
<b>5-1</b>	<b>Combinations of the asymmetries that should equal zero by parity invariance, divided by their standard deviations. See text. . . . .</b>	<b>91</b>
<b>D-1</b>	<b>These are the asymmetries or coincidence analyzing powers measured in the experiment. . . . .</b>	<b>115</b>
<b>D-2</b>	<b>These are the parity-combined asymmetries or coincidence analyzing powers measured in the experiment (except that the points for <math>0^\circ</math> and <math>180^\circ</math> are not combined). BGO A is a composite of BGO's 1 and 2 as described in the text. . . . .</b>	<b>116</b>

### List of Figures

3-1	Plan of beam areas at LAMPF including EPB. . . . .	18
3-2	Schematic plan view of experiment 832. . . . .	19
3-3	Target and target-changer. . . . .	20
3-4	Schematic drawing of the phi paddles part of S2. . . . .	22
3-5	Schematic drawing of the ring detectors part of S2. The light guides and photomultiplier tube for R3 is shown, with R1 and R2 having similar arrangements. . . . .	23
3-6	S2 electronics. . . . .	28
3-7	Schematic diagram of the events triggers. . . . .	29
3-8	BGO electronics in 1985. . . . .	30
3-9	BGO electronics in 1986. . . . .	31
4-1	Percent-live-times of various scalers. The busy wire is disconnected for the times on the left-hand side of these plots, until minute number 5030. During this time the scalers should read one, but scalers S1, A2, and A3 do not. . . . .	38
4-2	Average counts in two scalers <i>vs.</i> ion chamber counts for the same time.	40
4-3	S1-S2 timing spectrum for P1 sideways polarization data. . . . .	45
4-4	S1-S2 timing spectrum for data where the BGO ADC spectra (see Figure 4-5) were generated for each of the 8 small cuts indicated by the dotted lines. The crosses are the relative areas of the peak sizes found by a fitting procedure. See the text. . . . .	46

4-5	The BGO ADC spectra for the narrow timing cuts shown in Figure 4-4. The horizontal axis is in channels and the vertical axis is in counts. Part a) corresponds to the leftmost or first timing cut, b) is the second, <i>etc.</i> The 15.11-MeV peak (near channel 660) has been fitted as described in the text and the peak areas plotted in Figure 4-4. . . . .	47
4-6	Pulse-height spectra for a paddle and for S1. . . . .	49
4-7	Scatter plot of pulse-height (dE/dx) in one paddle <i>vs.</i> S1-S2 timing for that paddle. . . . .	50
4-8	Sample BGO timing spectrum. Both on-time and off-time cuts are shown.	52
4-9	BGO timing spectrum where microstructure of the beam is evident. . .	53
4-10	Scatter plot of S1-S2 timing on the <i>y</i> axis <i>vs.</i> BGO timing. The beam microstructure can be seen in the horizontal band. . . . .	54
4-11	The top spectrum is the uncut BGO 3 timing in summer 1986. The bottom spectrum has had cuts made on the BGO pulse-height spectrum in the neighborhood of the 15.11-MeV peak. . . . .	56
4-12	The energy spectrum of pile-up counts for the 1985 normal polarization data. . . . .	57
4-13	Longitudinal polarization on-time raw, off-time and randoms-subtracted spectra for BGO 2. . . . .	60
4-14	Same as Figures 4-13 and 4-8 for BGO 3 sideways polarization. . . . .	61
4-15	EGS4 spectrum of 68.74 MeV $\gamma$ 's in BGO (one-half the $\pi_0$ mass). . . .	63
4-16	Comparison of expected background from $\pi_0$ decay and real data for the most forward BGO (BGO 1) and the most backward one (BGO 4). . .	65
4-17	Comparisons of BGO spectra for protons scattered to the left and protons scattered to the right for the four BGO's. See the text. These are spectra before the randoms are subtracted. . . . .	67

4-18	Results of a Monte Carlo calculation for neutron knockout on $^{12}\text{C}$ (including Fermi momentum) showing neutron momentum <i>vs.</i> outgoing proton $\phi$ angle. See text. . . . .	69
4-19	Same as Figure 4-18 but now <i>vs.</i> outgoing proton $\theta$ angle. S2 acceptance angles are indicated by dashed lines. See text. . . . .	70
4-20	BGO response to neutrons of the energies indicated from Ref. [HLAK83].	71
4-21	Basic 15.11-MeV spectrum in BGO from EGS4. . . . .	72
4-22	Example of result of convoluting the basic EGS4 15.11MeV spectrum with a gaussian to represent resolution. . . . .	73
4-23	Fit of the basic 4.44-MeV EGS4 spectrum convoluted with a gaussian to some 4.44-MeV source calibration data. . . . .	74
4-24	The top spectrum and fit is for 1986 BGO 2 of all azimuthal proton directions and both polarizations to get the gaussian width and centroid position, and the lower spectrum is a for a single azimuthal direction and polarization. The on-time background is shown as a dotted line. See the text. . . . .	76
4-25	Two-parameter fit corresponding to Figure 4-24. The on-time background is shown as a dotted line. . . . .	78
4-26	A typical 4.44-MeV peak. This is BGO 2 from summer 1986 longitudinal data. . . . .	81
5-1	$A_n^{coinc}$ for 1985 normal polarization data. The solid lines are DREX and the dashed lines are DW81. The solid points are data from Hicks <i>et al.</i> [Hic88]. . . . .	83
5-2	$A_p^{coinc}$ for 1985 sideways polarization data. The solid lines are DREX and the dashed lines are DW81. . . . .	84

5-3	$A_f^{coinc}$ for 1986 longitudinal polarization data. The solid lines are DREX and the dashed lines are DW81. . . . .	85
5-4	$A_n^{coinc}$ for 1986 normal polarization data. The solid lines are DREX and the dashed lines are DW81. The solid points are data from Hicks <i>et al.</i> [Hic88]. . . . .	86
5-5	Regular and parity inverted schematic views of scattering to top and bottom parts of S2 with sideways polarization. (In the elevation views $\otimes$ and $\odot$ signify polarization direction into and out of the page respectively, and the BGO's are not shown for clarity.) . . . . .	89
5-6	Distribution of the values in Table 5-1. These are combinations of the asymmetries for all directions of polarization, divided by their standard deviations. See text. . . . .	92
5-7	The off-time asymmetries (whole spectrum) for normal and sideways polarizations, 1985. The dashed lines are $0.43 \cos$ and $-0.43 \sin$ . . . . .	93
5-8	The off-time asymmetries (whole spectrum) for longitudinal and normal polarizations, 1986. The dashed line is $0.4 \cos$ . . . . .	94
5-9	BGO's 1 and 2 have been combined into BGO A as described in the text. BGO's 3 and 4 are the same as in Figures 5-1 and 5-2, reproduced here to aid in seeing any trends. See the text. . . . .	97
5-10	Data of Hicks <i>et al.</i> The BGO's are in the horizontal plane and $\theta_\gamma$ is in the lab frame measured from the beam direction (counter-clockwise looking down). The proton is scattered to the left. . . . .	99

## ABSTRACT

Analyzing-power measurements  $A_n^{coinc}$ ,  $A_s^{coinc}$ , and  $A_l^{coinc}$  are presented for the reaction  $^{12}\text{C}(\bar{p}, p'\gamma)^{12}\text{C}^*$  (15.11 MeV). A polarized proton beam at 318 MeV was used and data were taken for 3 mutually perpendicular directions of polarization. A scintillator hodoscope was used for scattered proton detection and 4 BGO detectors for the 15.11 MeV  $\gamma$ -ray. Data are presented for 8 azimuthal directions of the scattered proton around the beam direction, and for the polar angles averaged between  $3.3^\circ$  and  $11.2^\circ$ . The data are compared with non-relativistic calculations (DW81) and relativistic calculations with explicit treatment of exchange (DREX). The average size of the asymmetries measured is comparable to these predictions but does not agree closely with either prediction.

COINCIDENCE ANALYZING-POWER MEASUREMENTS  
OF THE REACTION  $^{12}\text{C}(\bar{p}, p'\gamma) ^{12}\text{C}^*$   
THROUGH THE 15.11 MEV STATE

## Chapter 1

### Introduction

There have been numerous comparisons in recent years of relativistic versus non-relativistic treatments of proton scattering on nuclei. The first comparisons of proton elastic scattering data with relativistic calculations of differential cross sections and analyzing powers  $A_y$  showed remarkable agreement, although nonrelativistic distorted-wave Born-approximation (DWBA) calculations also gave good results [SMW83]. As more calculations of inelastic proton scattering to various states of different targets have become available, the picture that has so far emerged is not as clear as in the elastic case. In the case of some transitions, such as for low-energy natural-parity states in even-even nuclei ( $^{24}\text{Mg}$  and  $^{28}\text{Si}$ ), relativistic distorted-wave calculations gave excellent agreement [HJL\*88] and, on the whole, relativistic calculations have tended to give somewhat better results than nonrelativistic calculations. But in some other transitions, nonrelativistic DWBA calculations have done as well or better than their relativistic counterparts, or neither has been able to fit the data well. For instance, relativistic  $A_y$  calculations for the  $5^-(4.49 \text{ MeV})$  state of  $^{40}\text{Ca}$  at  $E_p=362 \text{ MeV}$  only fit the data out to a  $\theta_{cm}$  of  $30^\circ$ , whereas a nonrelativistic DWBA calculation (using the Love-Franey NN interaction) does better beyond that point (although still not with very good agreement) [FWA\*87].

In the case of  $^{12}\text{C}$ , the target investigated in this experiment, the situation is particularly unclear. Neither type of calculation of  $A_y$  for natural-parity states shows good agreement with the data from previous experiments, at least for higher momentum transfers beyond the first minimum.[HJL\*88, CMF\*82, RS87] Two transitions to

unnatural-parity states (therefore indicating spin flip) have been studied so far at intermediate energies. In the case of the 12.71-MeV  $J^\pi, T=1^+, 0$  state, a nonrelativistic distorted-wave calculation (DW81) of  $A_y$  does better than a relativistic treatment (DREX) at 400 MeV [HHA\*88]; for 200 MeV data, a relativistic calculation with explicit treatment of exchange between projectile and target nucleons (DREX) does worse than another relativistic calculation (DRIA) without exchange terms in the transition amplitude (Ref. 5). The situation is also unclear for the 15.11-MeV  $J^\pi, T=1^+, 1$  state at 200 MeV. Neither the nonrelativistic calculation for  $A_y$  (DW81) nor the full relativistic treatment with exchange (DREX) fit the data well, although a calculation of DW81 with one of the four Cohen and Kurath transition densities (see section 2.2) set to zero resembles the relativistic treatment without exchange (DRIA), and they fit the  $A_y$  data much better than the fuller treatments. Other evidence, however, including calculations of  $P-A_y$  (polarization minus analyzing power) indicates that the Cohen and Kurath transition density should be kept. Measurements of  $P-A_y$ , a combination of observables that is sensitive to particular parts of the inelastic transition that are known to be linked to non-local, velocity dependent forces and exchange effects, do not clearly favor either type of model for the 12.71 and 15.11 MeV states at 400 MeV [HHA\*88].

This experiment, a  $(\bar{p}, p'\gamma)$  coincidence study of the 15.11-MeV state of  $^{12}\text{C}$ , was undertaken to obtain greater sensitivity to the reaction models.  $(p, p'\gamma)$  coincidence studies such as this one give spin information that is not available from  $(p, p')$  singles experiments. Singles experiments, which do not detect the spin substate of the target nucleus, determine at most eight observables, which for a given incident proton energy and scattering angle are the unpolarized cross section, the polarization  $P$  produced in the scattering, the analyzing power  $A_y$ , and five of the nine components of the spin transfer tensor  $D_{ij}$  (the other components are zero because of parity and rotational invariance). However, the excitation by an incident proton of a  $J^\pi = 0^+$  ground state nucleus to

a state whose angular momentum is  $J$  is determined by a total of  $8J + 3$  independent quantities, which comes about as follows. There are 2 initial states corresponding to the two spin states of the projectile, and  $2(2J + 1)$  final states corresponding to possible combinations of the 2 final spin states of the proton and the  $2J + 1$  possible spin states of the excited nucleus. This gives, for each scattering angle and proton bombarding energy,  $4(2J + 1)$  complex numbers for the scattering amplitude. However, parity and rotational invariance, which hold true for the case of strong interactions, cause half of these to be zero (with the proper choice of axes) [MWZ86]. The real and imaginary components of the remaining  $2(2J + 1)$  complex numbers are a possible  $8J + 4$  independent real quantities, which become  $8J + 3$  when an arbitrary overall phase is subtracted. There are thus a minimum of  $8J + 3$  possible independent experiments for such a reaction at each scattering angle and incident proton energy. Singles experiments thus cannot supply complete information, for example, for a  $1^+$  excitation such as the 15.11-MeV state where there are a minimum of 11 possible independent observables. However, the angular correlation of the direction of the  $\gamma$  from de-excitation of the state with the proton scattering direction can supply information on the target spin final state, therefore allowing access to more information.

An example of this is the case of analyzing-power measurements. For singles measurements, if one uses a coordinate system where one axis is normal to the scattering plane and makes analyzing-power measurement after polarizing the proton in the direction of each axis, parity and rotational invariance require that a non-zero measurement can be made only when the polarization is normal to the scattering plane. Once there is a de-excitation  $\gamma$  measured, however, the possibility of analyzing-power measurements in the other two directions now exists. (Parity and rotational invariance will be discussed further in section 5.2.)

This experiment is the first to measure longitudinal and sideways analyzing powers,

besides the analyzing power normal to the scattering plane ( $A_y$ ). Another  $(\vec{p}, p'\gamma)$  measurement on  $^{12}\text{C}$  has been done at 400 MeV with incident protons polarized normal to the  $p-p'$  plane by Hicks *et al.* who found evidence in favor of relativistic models [HAC\*88, Hic88]. Their experiment detected  $\gamma$  rays with an array of detectors in the scattering plane at angles greater than  $90^\circ$  with respect to the beam and also two other detectors located perpendicular to the scattering plane directly above and below the target. A magnetic spectrometer was used to detect the scattered protons. In our experiment we used a scintillator hodoscope for the scattered proton detection and took data for several proton scattering angles simultaneously, so that various geometries with the  $\gamma$  out-of-plane were measured.

The 15.11-MeV state of  $^{12}\text{C}$  has been studied frequently in the past. The fact that  $^{12}\text{C}$  has an even-even  $0^+$  ground state restricts orbital and spin angular momentum transfers. Also, it is an unnatural parity state ( $1^+$ ) and this restricts the form of the interaction to include only terms involving spin flip. Similarly, the interaction includes only terms involving isospin flip because the transition to the 15.11-MeV state is  $\Delta T = 1$ . Finally, the state lies near the proton separation energy (the binding energy of a proton in  $^{12}\text{C}$  is 15.96 MeV), and therefore feeding from higher energy levels is not expected to be a problem. (This enables us to use a scintillator hodoscope rather than a magnetic spectrometer to detect the scattered proton.)

The experiment was done with 318 MeV incident protons at an energy that is high enough that the impulse approximation is valid. This approximation, which neglects multiple interactions in the nucleus and uses the free nucleon-nucleon interaction to approximate the interaction of the projectile with the struck target nucleon, enables the reaction to be described in a simple way. Both the theoretical calculations to which our results are compared use the impulse approximation.

The incident proton energy is not far above the pion threshold (280 MeV for  $\pi_0$ ).

and 292 MeV for  $\pi_+$  and  $\pi_-$  in NN collisions). The cross section for both charged and neutral pion production is approximately  $80 \mu\text{b}$  [LM70] (about 100 times smaller than the 15.11 - MeV state cross section), and thus contamination should not be a problem either in detecting the proton, or in detecting the  $\gamma$  (in spite of the fact that every  $\pi_0$  decays into  $\gamma$ 's.)

The questions addressed by our experiment are both of the detailed nature of the nucleon-nucleus interaction and the broader picture of the need for a Lorentz-covariant description of processes on the nuclear level. It has been pointed out [PAS85] that since the Dirac formalism has given an explanation of spin as a natural by-product of insuring Lorentz covariance, it is natural that relativistic effects be most obvious in spin observables. Much of the analysis of nuclear interactions has been based on nonrelativistic models up until this point, and it is important to determine to what extent a more relativistically covariant treatment is needed. It is hoped that this experiment will be helpful in answering these questions.

## Chapter 2

### Theoretical Background

The theoretical calculations to which our coincidence analyzing powers are compared are derived from distorted wave impulse approximation calculations using both nonrelativistic (program DW81) and relativistic (program DREX) models. As we will discuss below, the coincidence observables can be expressed as functions of the  $(p, p')$  singles amplitudes for excitation of the 15.11-MeV state and the  $\gamma$ -ray direction [PRS90], and therefore can be derived from existing codes which calculate the singles amplitudes. The formalism involved in this factorization is independent of the way in which the amplitudes are calculated, *e.g.* it can be used with amplitudes derived from either DW81 or DREX. The DW81 and DREX amplitudes and the program which computes the observables were supplied by J. Piekarewicz [She]. Some modifications and corrections to the program were done by the author. The amplitudes were calculated for incident proton energy of 400 MeV. (The amplitudes do not change greatly with incident proton energy [Pie89], and a request has been made for the amplitudes for 318 MeV incident proton energy.)

Our discussion of the theoretical background will be divided into three parts. In section 2.1 we will discuss how the  $(p, p'\gamma)$  observables can be calculated with the  $(p, p')$  singles amplitudes for the excitation of the same state. In section 2.2 we will discuss the process of arriving at the singles amplitudes using a nonrelativistic distorted wave impulse approximation. Finally in section 2.3 we will discuss the relativistic distorted wave impulse approximation.

## 2.1 Derivation of the Coincidence Observables from the Singles Amplitudes

In this section we will summarize the treatment of Piekarewicz *et al.* [PRS90]. In the proton-nucleus center of mass system one can define coordinate axes along  $\mathbf{n} = \mathbf{p} \times \mathbf{p}'$ ,  $\mathbf{K} = \mathbf{p} + \mathbf{p}'$  and  $\mathbf{q} = \mathbf{n} \times \mathbf{K}$ . The coincidence analyzing powers are special cases of the spin transfer coefficients  $D_{\alpha\beta}(\hat{\mathbf{k}})$  where  $\alpha$  and  $\beta$  refer to the spin of the outgoing and incoming projectile respectively and  $\hat{\mathbf{k}}$  is in the direction of the detected  $\gamma$  ray. These are generalizations of the singles spin transfer coefficients or Wolfenstein depolarization tensor [Wol56] (see chapter 1), which give the contribution to the final polarization of the projectile from each component of the initial projectile polarization (see equation 2-8 below). The analyzing powers are special cases of  $D_{\alpha\beta}(\hat{\mathbf{k}})$  with  $\alpha = 0$  and are calculated in the program mentioned above using the equation:

$$D_{\alpha\beta}(\hat{\mathbf{k}}) = \frac{\sum_{ij\mu\nu} A_{i\mu} A_{j\nu}^* t_{ij}(\hat{\mathbf{k}}) \text{Tr}[\sigma_\alpha \sigma_\mu \sigma_\beta \sigma_\nu]}{2 \sum_{ij\mu} A_{i\mu} A_{j\mu}^* t_{ij}(\hat{\mathbf{k}})} \quad i, j = n, K, q; \quad \alpha, \mu, \beta, \nu = 0, n, K, q. \quad (2-1)$$

The  $A$ 's are components of the  $(p, p')$  scattering amplitude, the  $t_{ij}(\hat{\mathbf{k}})$  tensor includes the effects of the  $\gamma$ -ray de-excitation amplitude, and the  $\sigma$ 's are Pauli spin operators ( $\sigma_0$  is the  $2 \times 2$  unit matrix). The derivation of equation 2-1 is as follows.

The most general form of the  $(p, p')$  singles amplitude for the  $0^+$  to  $1^+$  transition consistent with rotational and parity invariance is [Ama82]:

$$\begin{aligned} \hat{T}^p(\mathbf{p}, \mathbf{p}') = & A_{n0}(\hat{\Sigma} \cdot \hat{\mathbf{n}}) + A_{nn}(\hat{\Sigma} \cdot \hat{\mathbf{n}})(\sigma \cdot \hat{\mathbf{n}}) + A_{KK}(\hat{\Sigma} \cdot \hat{\mathbf{K}})(\sigma \cdot \hat{\mathbf{K}}) \\ & + A_{Kq}(\hat{\Sigma} \cdot \hat{\mathbf{K}})(\sigma \cdot \hat{\mathbf{q}}) + A_{qK}(\hat{\Sigma} \cdot \hat{\mathbf{q}})(\sigma \cdot \hat{\mathbf{K}}) + A_{qq}(\hat{\Sigma} \cdot \hat{\mathbf{q}})(\sigma \cdot \hat{\mathbf{q}}) \end{aligned} \quad (2-2)$$

which can be cast in compact form as

$$\hat{T}^p(\mathbf{p}, \mathbf{p}') = \sum_{i\mu} A_{i\mu} \hat{\Sigma}_i \sigma_\mu \quad i = n, K, q; \quad \mu = 0, n, K, q. \quad (2-3)$$

Here

$$\hat{\Sigma}^M = |1^+ M\rangle \langle 0^+|$$

is the polarization operator of the target, the  $\sigma$ 's refer to the projectile ( $\sigma_0$  is the  $2 \times 2$  unit matrix), and the hat on  $\hat{T}^p$  and  $\hat{\Sigma}$  denotes an operator. There are only six terms in equation 2-2 because the transition amplitude must be a scalar for a  $1^+$  transition—the other 6 pseudoscalar terms contribute to the  $1^-$  transition.

Using the density matrix expression for the unpolarized cross section [RT67]:

$$\left(\frac{d\sigma}{d\Omega_p}\right)_0 = \frac{1}{2} \text{Tr}[\hat{T}^p \hat{T}^{p\dagger}] = \frac{1}{2} \text{Tr}[\sum_{i\mu\nu} A_{i\mu} A_{j\nu}^* \hat{\Sigma}_i \hat{\Sigma}_j^\dagger \sigma_\mu \sigma_\nu] \quad .$$

Since  $\text{Tr}(\sigma_\mu \sigma_\nu) = 2\delta_{\mu\nu}$  and  $\text{Tr}[\hat{\Sigma}_i \cdot \hat{e}_i](\hat{\Sigma}_j \cdot \hat{e}_j) = \hat{e}_i \cdot \hat{e}_j = \delta_{ij}$  this reduces to

$$\left(\frac{d\sigma}{d\Omega_p}\right)_0 = \sum_{i\mu} |A_{i\mu}|^2 \quad .$$

The singles analyzing powers  $A_y$ ,  $A_x$ , and  $A_z$  which are defined experimentally as [CMF\*82]

$$A_i = \frac{(\frac{d\sigma}{d\Omega_p})_{\uparrow} - (\frac{d\sigma}{d\Omega_p})_{\downarrow}}{p_{\downarrow}(\frac{d\sigma}{d\Omega_p})_{\uparrow} + p_{\uparrow}(\frac{d\sigma}{d\Omega_p})_{\downarrow}} \quad , i = x, y, z, \quad (2-4)$$

are derived from the density matrix formalism as follows. The density matrix for the initial state is [Ohl72]

$$\rho_i = \frac{1}{2} \left(1 + \sum_{j=1}^3 p_j \sigma_j\right)$$

(where the trace of  $\rho_i$  is unity and the  $p_j$ 's are the components of the beam polarization), and for the final state is

$$\rho_f = \hat{T}^p \rho_i \hat{T}^{p\dagger} = \frac{1}{2} \hat{T}^p \hat{T}^{p\dagger} + \frac{1}{2} \sum_{j=1}^3 p_j \hat{T}^p \sigma_j \hat{T}^{p\dagger} \quad . \quad (2-5)$$

The cross section is

$$\frac{d\sigma}{d\Omega} = \text{Tr}(\rho_f) = \left(\frac{d\sigma}{d\Omega_p}\right)_0 \left(1 + \sum_{j=1}^3 p_j A_j\right) \quad (2-6)$$

where again  $(\frac{d\sigma}{d\Omega_p})_0$  is the cross section for an unpolarized beam and

$$A_j = \frac{\text{Tr}(\hat{T}^p \sigma_j \hat{T}^{p\dagger})}{\text{Tr}(\hat{T}^p \hat{T}^{p\dagger})} \quad . \quad (2-7)$$

Using equation 2-6 in equation 2-4 (and being careful about the signs of the  $p_j$ ) verifies that 2-7 is equivalent to the analyzing power.

The  $(p, p')$  spin transfer coefficients are given by

$$p_{k'} \frac{d\sigma}{d\Omega} = \left( \frac{d\sigma}{d\Omega_p} \right)_0 (P_{k'} + \sum_{j=1}^3 p_j D_{jk}) \quad (2-8)$$

which comes from 2-5, 2-6 and

$$p_{k'} \equiv \langle \sigma_{k'} \rangle = \frac{\text{Tr}(\rho_f \sigma_{k'})}{\text{Tr}(\rho_f)}$$

so that

$$D_{\alpha\beta} = \text{Tr}[\sigma_\alpha \hat{T}^p \sigma_\beta \hat{T}^{p\dagger}] / \text{Tr}[\hat{T}^p \hat{T}^{p\dagger}] ,$$

where also the polarization

$$P_{k'} = \frac{\text{Tr}(\hat{T}^p \hat{T}^{p\dagger} \sigma_{k'})}{\text{Tr}(\hat{T}^p \hat{T}^{p\dagger})}$$

Using 2-3, the  $D_{\alpha\beta}$  become for the  $0^+ \rightarrow 1^+$

$$D_{\alpha\beta} = \frac{\sum_{i\mu\nu} A_{i\mu} A_{i\nu}^* \text{Tr}[\sigma_\alpha \sigma_\mu \sigma_\beta \sigma_\nu]}{2 \sum_{i\mu} |A_{i\mu}|^2}$$

For singles measurements there is only one analyzing power,  $D_{0n} \equiv A_y$ , because of parity and rotational invariance.

To represent the  $\gamma$ -ray coincidence observables, the de-excitation amplitude must be included. This amplitude for de-excitation from a state with angular momentum  $J$  can be expressed as

$$\hat{T}_{J\lambda}^\gamma(\mathbf{k}) = \sum_M T_{JM\lambda}^\gamma(\mathbf{k}) \hat{\Sigma}_{J^\pi M}^\dagger$$

where

$$T_{JM\lambda}^\gamma = \langle 0^+ | J_\lambda(\mathbf{k}) | J^\pi M \rangle$$

and where  $\mathbf{k}$  is the  $\gamma$ -ray momentum and  $\lambda = \pm 1$  is its polarization. Here

$$J_\lambda(\mathbf{k}) = \int d^3x e^{-i\mathbf{k}\cdot\mathbf{x}} \mathbf{J}(\mathbf{x}) \cdot \hat{\mathbf{e}}_\lambda(\mathbf{k})$$

and  $\mathbf{J}(\mathbf{x})$  is the electromagnetic current in the nucleus and  $e^{-i\mathbf{k}\cdot\mathbf{x}}\hat{\mathbf{e}}_\lambda$  is the vector potential associated with a  $\gamma$ -ray along the  $\mathbf{k}$  direction ( $\hat{\mathbf{e}}_\lambda(\mathbf{k}) \perp \mathbf{k}$ ). After an expansion in terms of electric and magnetic multipole operators and Wigner  $\mathcal{D}$ -functions (see Ref. [PRS90] for details), the amplitude coefficients take the form

$$T_{JM\lambda}^\gamma(\mathbf{k}) = T_{J\lambda}^\gamma(k)\mathcal{D}_{M-\lambda}^{J*}(\mathbf{k})$$

where  $T_{J\lambda}^\gamma(k)$  is a reduced matrix element. For the  $1^+ \rightarrow 0^+$  de-excitation

$$\mathcal{D}_{M\lambda}^1(\mathbf{k}) = \hat{\mathbf{e}}_M^* \cdot \hat{\mathbf{e}}_\lambda(\hat{\mathbf{k}})$$

and

$$\hat{T}_{J\lambda}^\gamma(\mathbf{k}) = T_{J\lambda}^\gamma(k) \left[ \sum_M \hat{\mathbf{e}}_M^* (\hat{\Sigma}_M \cdot \hat{\mathbf{e}}_{-\lambda}(\hat{\mathbf{k}}))^\dagger \right] = T_\lambda^\gamma(k) [\hat{\Sigma} \cdot \hat{\mathbf{e}}_{-\lambda}(\hat{\mathbf{k}})]^\dagger$$

The transition amplitude for the  $1^+$  excitation followed by the de-excitation to the  $0^+$  ground state is the product of the two transition amplitudes:

$$\begin{aligned} \hat{T}_\lambda^{\mathcal{P}\gamma}(\mathbf{k}) &= \hat{T}_\lambda^\gamma(\mathbf{k}) \hat{T}^{\mathcal{P}}(\mathbf{p}, \mathbf{p}') \\ &= T_\lambda^\gamma(k) [\hat{\Sigma} \cdot \hat{\mathbf{e}}_{-\lambda}(\hat{\mathbf{k}})]^\dagger \sum_{i\mu} A_{i\mu} [\hat{\Sigma} \cdot \hat{\mathbf{e}}_i] \sigma_\mu \\ &= T_\lambda^\gamma(k) \sum_{i\mu} A_{i\mu} [\hat{\mathbf{e}}_i \cdot \hat{\mathbf{e}}_{-\lambda}(\hat{\mathbf{k}})] \sigma_\mu \end{aligned}$$

The coincidence observables  $\frac{d^2\sigma}{d\Omega_p d\Omega_\gamma}$  and  $D_{\alpha\beta}(\mathbf{k})$  for excitation to the  $1^+$  state take on a form similar to the  $(p, p')$  singles:

$$\frac{d^2\sigma}{d\Omega_p d\Omega_\gamma} = |T_\lambda^\gamma(k)|^2 \sum_{ij\mu} A_{i\mu} A_{j\mu}^* t_{ij}(\hat{\mathbf{k}})$$

and

$$D_{\alpha\beta}(\hat{\mathbf{k}}) = \frac{\sum_{ij\mu\nu} A_{i\mu} A_{j\nu}^* t_{ij}(\hat{\mathbf{k}}) T\tau[\sigma_\alpha \sigma_\mu \sigma_\beta \sigma_\nu]}{2 \sum_{ij\mu} A_{i\mu} A_{j\mu}^* t_{ij}(\hat{\mathbf{k}})}$$

where

$$t_{ij}(\hat{\mathbf{k}}) \equiv \sum_{\lambda=\pm 1} [\hat{\mathbf{e}}_i \cdot \hat{\mathbf{e}}_\lambda(\hat{\mathbf{k}})] [\hat{\mathbf{e}}_j \cdot \hat{\mathbf{e}}_\lambda^*(\hat{\mathbf{k}})] = \delta_{ij} - (\hat{\mathbf{k}} \cdot \hat{\mathbf{e}}_i)(\hat{\mathbf{k}} \cdot \hat{\mathbf{e}}_j) \quad (2-9)$$

The reduced matrix element cancels in the spin transfer coefficients. Also, in addition to  $D_{0n}(\hat{\mathbf{k}})$ ,  $D_{0q}(\hat{\mathbf{k}})$  and  $D_{0K}(\hat{\mathbf{k}})$  exist and are related to the longitudinal and sideways coincidence analyzing powers measured in this experiment by a rotation of coordinate axes.

## 2.2 Nonrelativistic DWIA Calculation

Since a description of the complex phenomenon of inelastic proton scattering from a nucleus cannot yet be fully derived from first principles, a phenomenological approach has to be taken wherein general forms are constrained by the available experimental information. The nonrelativistic phenomenological description that is compared to our data is a form of the distorted-wave impulse approximation (DWIA). In the impulse approximation, the interaction of the projectile is taken to be  $t^{NN}$ , the  $t$  matrix or transition matrix for the free nucleon-nucleon interaction, and the projectile is considered to scatter from at most one nucleon. This approximation has been shown to be not too severe if projectile energies are high enough,  $\gtrsim 100$  MeV, for then the wavelength of the projectile is short (thus it interacts with only one nucleon at a time) and also the mean free path in the nucleus is long enough that multiple interactions are not very important.

The DWIA study used here is also a distorted-wave Born approximation (DWBA) as we will now discuss. Although the program DW81 [RS77] is somewhat different than a standard distorted-wave Born approximation in that it uses a helicity representation where the spin of each particle is quantized along its direction of motion, the main features of the standard DWBA are as follows. The potential for which a solution to the Schrodinger equation is sought is divided into two parts — the first part  $U_1$  is the Coulomb interaction between the projectile and the target nucleus which has a known solution, and the second part  $U_2$  is an optical potential, *i.e.* a phenomenological representation of the overall effective potential on the projectile from the strong interactions

with the nuclear medium, for which we do not know the solution. If  $\chi_1^\pm(\mathbf{k}, \mathbf{r})$  are the known outgoing (+) and incoming (-) spherical wave solutions to the Schroedinger equation for the potential  $U_1$ , the total solution at large values of  $r$  can be expressed [Sat80] as

$$\chi(\mathbf{k}, \mathbf{r}) = \chi_1^+(\mathbf{k}, \mathbf{r}) - \frac{e^{ikr}}{4\pi r} \int \chi_1^-(\mathbf{k}', \mathbf{r}')^* U_2(r') \chi(\mathbf{k}, \mathbf{r}') d\mathbf{r}'$$

which can be solved by a Born approximation by substituting  $\chi_1^+(\mathbf{k}, \mathbf{r})$  for  $\chi(\mathbf{k}, \mathbf{r})$  on the right hand side of the equation:

$$\chi(\mathbf{k}, \mathbf{r}) = \chi_1^+(\mathbf{k}, \mathbf{r}) - \frac{e^{ikr}}{4\pi r} \int \chi_1^-(\mathbf{k}', \mathbf{r}')^* U_2(r') \chi_1^+(\mathbf{k}, \mathbf{r}') d\mathbf{r}' \quad . \quad (2-10)$$

The form of the potential in our case is a Woods-Saxon shape,

$$U(r) = \frac{-V}{e^{(r-R)/a} + 1}$$

where  $V$ ,  $R$ , and  $a$  are parameters to be determined from elastic scattering data. Equation 2-10 then yields the distorted waves that are needed for the DWIA calculation. (Note that these waves include effects of multiple scattering as well.)

The impulse approximation then consists of forming the transition matrix  $(\hat{T}^p)_{fi}$ ; (as in 2-2) from a sum of the effects of  $t^{NN}$  on each nucleon involved in the transition [CG52]

$$(\hat{T}^p)_{fi} = \sum_{j=1}^{N_p} \langle \chi_f \phi_f | t_j^{NN} | \chi_i \phi_i \rangle$$

where  $i$  and  $f$  stand for initial and final and the sum is over the  $p$  shell target nucleons. Two elements are still needed for this prescription— one is the wave functions for the bound states of the nucleus and the other is the form for the NN interaction. Each of these involves a phenomenological fit to experimental data. The bound state wave functions are taken from Cohen and Kurath [CK65, LK80], who have determined transition densities for the  $1p$  states from fitting energy levels of various nuclei. (Transitions from the  $S$  state are ruled out for the 15.11 MeV  $J^\pi = 1^+$  transition because of parity

arguments.) These densities are used in the programs DW81 and DREX in conjunction with harmonic oscillator radial functions, with size parameter  $\lambda$  given by electron scattering data.

Finally the  $t^{NN}$  has been approximated in the nonrelativistic case by Love and Franey [FL85, LF81] through a process of fitting the phase shifts from available nucleon-nucleon data. They assume the general form

$$V_{12} = V^C(r_{12}) + V^{LS}(r_{12})\mathbf{L} \cdot \mathbf{S} + V^T(r_{12})S_{12} \quad .$$

Here  $V^C$  is the central term,  $\mathbf{L} \cdot \mathbf{S}$  is the spin-orbit angular momentum operator and  $S_{12}$  is the tensor operator

$$S_{12} = 3(\sigma_1 \cdot \hat{\mathbf{a}})(\sigma_2 \cdot \hat{\mathbf{a}}) - \sigma_1 \cdot \sigma_2$$

where  $\sigma_1/2$  and  $\sigma_2/2$  are the spin operators of the projectile and target nucleons respectively and  $\hat{\mathbf{a}}$  is any direction. Each  $V^i(r_{12})$  is assumed to be a sum of Yukawa forms

$$V^C(r) = \sum_{i=1}^{N_C} V_i^C Y(r/R_i) \quad , Y(x) = e^{-x}/x$$

$$V^{LS}(r) = \sum_{i=1}^{N_{LS}} V_i^{LS} Y(r/R_i) \quad ,$$

$$V^T(r) = \sum_{i=1}^{N_T} V_i^T r^2 Y(r/R_i) \quad ,$$

and then, with

$$t^{NN}(E, q) = \int d^3r e^{-\mathbf{k} \cdot \mathbf{r}} V_{12} [1 + (-)^l P^x] e^{-\mathbf{k} \cdot \mathbf{r}} \quad ,$$

the parameters ( $V_i$ ) are varied until the best fit to the experimental data is obtained.  $P^x$  is the exchange operator which here changes  $\mathbf{r}$  to  $-\mathbf{r}$  and the second term in the integrand insures that there is antisymmetrization. (The  $(-1)^l$  takes care of the spin and isospin dependence since for two nucleons  $(-1)^l = (-1)^{S+T+1}$ .) It may be noted that in the nucleon-nucleus CM frame, scattering to angles greater than  $\sim 60^\circ$  produces momentum

transfers of  $q > 2k$ , the maximum allowed momentum transfer in the nucleon-nucleon CM frame ( $k$  is the momentum of each nucleon in the NN center of mass frame). The use of  $t^{NN}$  for nucleon-nucleus scattering for high momentum transfers therefore involves extrapolating  $t^{NN}$  off-shell.

### 2.3 Relativistic DWIA Calculation

The relativistic distorted wave impulse approximation shares many similarities in approach to its nonrelativistic counterpart. A complete treatment of the formalism, however, is quite complex and we only repeat some of the highlights here (see [SRP84] and [RS87]). The distorted waves are obtained from an integral form of the Dirac equation corresponding to equation 2-10. With  $\hat{U}$  being the phenomenological optical potential for elastic scattering and  $\psi_{\mathbf{k},s}$  having four components

$$[\not{p} - m - \hat{U}(E)]\psi_{\mathbf{k},s}(\mathbf{r}) = 0 \quad .$$

Using a decomposition of the potential into Coulomb ( $U_1$ ) and hadronic force part ( $U_2$ ) as before, the asymptotic integral equation as  $r \rightarrow \infty$  is given by [MSW83, Sat80]

$$\psi_{\mathbf{k},s}(\mathbf{r}) = \chi_1^+(\mathbf{k}, \mathbf{r})u_s - \frac{me^{ikr}}{2\pi} \sum_{s'} u_{s'} \bar{u}_{s'} \int d^3r' \chi_1^-(\mathbf{k}, \mathbf{r}')U_2(\mathbf{r}')\chi_1^+(\mathbf{k}, \mathbf{r}')u_s$$

where  $\chi_1^\pm$  are the known (four component) solutions to the Dirac equation for the Coulomb part of the potential. The distorted waves can be obtained from this equation using an optical potential which is derived phenomenologically.

The transition amplitude (as in 2-2) for N-nucleus scattering in the impulse approximation can be expressed as [RS87]

$$\begin{aligned} (\hat{T}^p)_{fi} &= \frac{-8\pi i p_{NN}}{E_{NN}} \sum_{n=1}^{N_p} \sum_{I_{NN}} \int d\mathbf{x} d\mathbf{y}_n \psi_{\mathbf{k}',s'}^{(-)}(\mathbf{x}') \Psi_{J_f M_f}^\dagger(\mathbf{y}_1, \dots, \mathbf{y}_A) \gamma^0(0) \gamma^0(n) \\ &\quad \times [\hat{F}_{NN}(|\mathbf{x} - \mathbf{y}|) \psi_{\mathbf{k}_s}^{(+)}(\mathbf{x}) \Psi_{J_i M_i}(\mathbf{y}_1, \dots, \mathbf{y}_n, \dots, \mathbf{y}_A) \\ &\quad + (-1)^T \hat{F}_{NN}(|\mathbf{x} - \mathbf{y}|) \psi_{\mathbf{k}_s}^{(+)}(\mathbf{y}_n) \Psi_{J_i M_i}(\mathbf{y}_1, \dots, \mathbf{x}, \dots, \mathbf{y}_A)] \end{aligned} \quad (2-11)$$

where

$$\hat{F}_{NN} = \frac{-8\pi i p_{NN} t^{NN}}{E_{NN}}$$

(see below), and  $\mathbf{x}$  refers to the projectile space and spin coordinates and the  $\mathbf{y}$  refer to the coordinates of the nucleons involved in the transition. The second term in the integrand is the exchange term. (The factor  $(-1)^T$  takes care of the isospin dependence and the space and spin coordinates are interchanged.)

The NN operator  $\hat{F}_{NN}$  is expressed in the most general Lorentz- invariant form in terms of Dirac  $\gamma$  matrices:

$$\begin{aligned} \hat{F} = & \hat{F}_S + \gamma(1) \cdot \gamma(2) \hat{F}_V + \gamma^5(1) \frac{\not{d}}{2M}(1) \gamma^5(2) \frac{\not{d}}{2M}(2) \hat{F}_P \\ & + \gamma^5(1) \gamma^5(2) \gamma(1) \cdot \gamma(2) \hat{F}_A + \sigma^{\mu\nu}(1) \sigma_{\mu\nu}(2) \hat{F}_T \end{aligned}$$

The  $\hat{F}$ 's are operators in the NN isospin space that depend on  $q^2$  and  $Q^2$  and their subscripts refer to the scalar, vector, pseudoscalar, axial vector and tensor transformation properties of their respective coefficients. In the case of elastic scattering from a spin-saturated nucleus such as the ground state of  $^{12}\text{C}$ , there is a trace over the struck nucleon spins which results in all but the scalar and time-like component of the vector term dropping out, but in the inelastic case all the terms must be kept. The strengths of the complex  $\hat{F}$ 's coefficients are obtained phenomenologically [Hor85] by assuming a parameterized form for the coefficients aimed at approximating the exchange of mesons of various masses and transformation properties and fitting the scattering data [Hor85]. Exchange terms are included in this process as well.

The program DREX which did the relativistic DWIA calculation uses the same helicity formalism as DW81, modified to handle four component spinors. The transition densities are from Lee and Kurath, and both DREX and DW81 use NN interactions which are fit to the same phase shifts [AR].

## Chapter 3

### Experimental Set-up

The experiment was done at LAMPF as experiment 832 during three periods: one in the fall of 1985, and one in each of the summer and fall of 1986. The experiment was done at the EPB experimental area using 318 MeV protons polarized in one of three mutually perpendicular directions: normal<sup>1</sup> (vertical), sideways (horizontal and perpendicular to the beam) and longitudinal (along the beam direction). During the first run in fall of 1985 we took data for normal and sideways polarizations, during the summer of 1986 we took longitudinal polarization data, and during fall of 1986 we took additional normal polarization data. A plan of the EPB area is shown in figure 3-1. Figure 3-2 shows a plan view of the experimental apparatus.

The target used was a 1.62 g/cm<sup>2</sup> (1/4 in. thick) carbon target. It was mounted at an angle of 63° with the beam on a device that could place the target in and out of the beam by remote control (see figure 3-3). A closed-circuit TV camera monitored the target position.

#### 3.1 Detectors

The experiment was a double-armed experiment: the first arm detected the scattered proton, and the second arm detected the  $\gamma$ -ray from the de-exciting nucleus. We will consider the two arms in turn.

---

<sup>1</sup>The word "normal" is also used to refer to one of the two 180°-apart directions within each of the three types of polarization, and this sometimes causes confusion. However, since the usage is standard for both meanings of the word, we will also use "normal" for both meanings, and it should be clear from the context which meaning is intended.

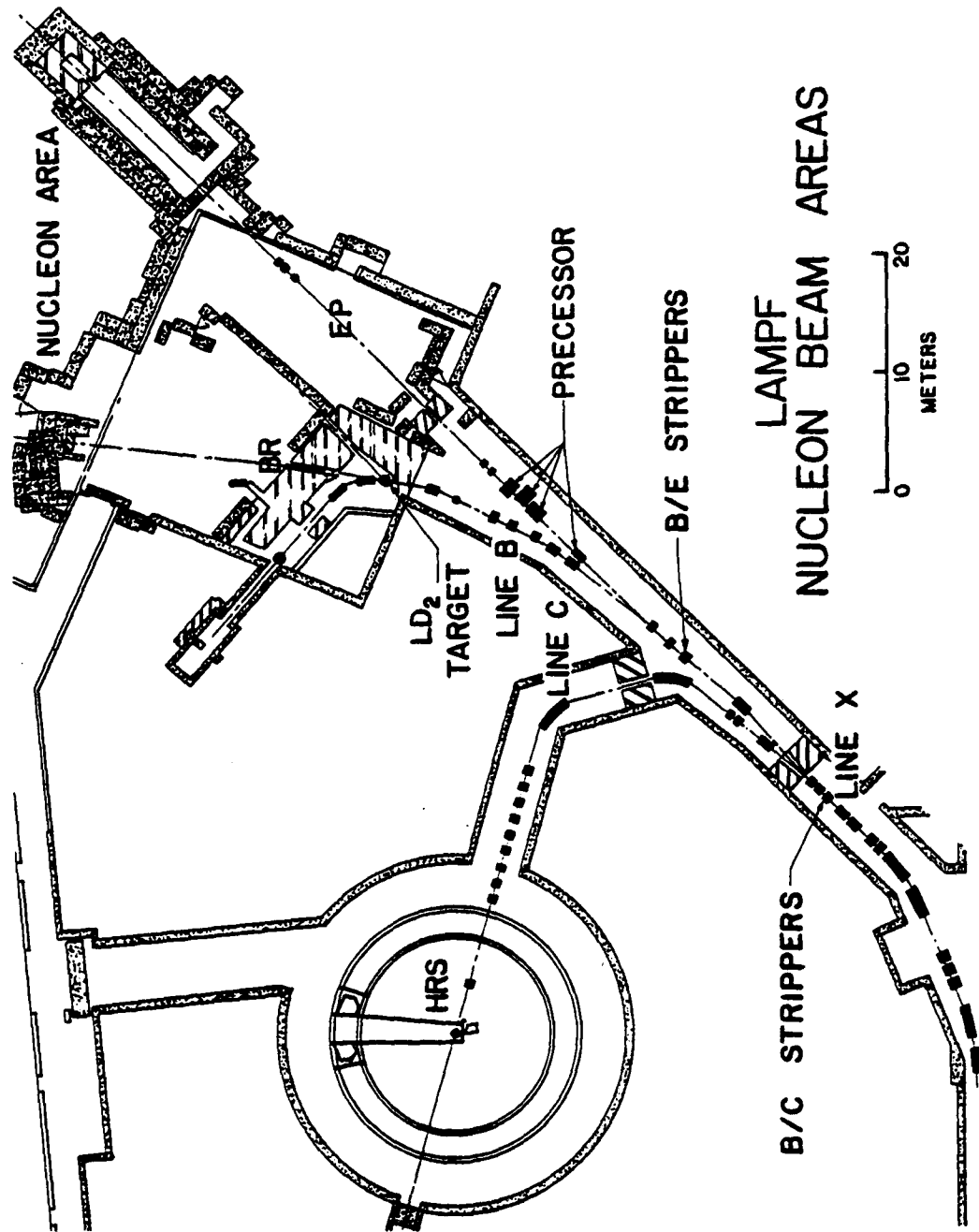


Figure 3-1: Plan of beam areas at LAMPF including EPB.

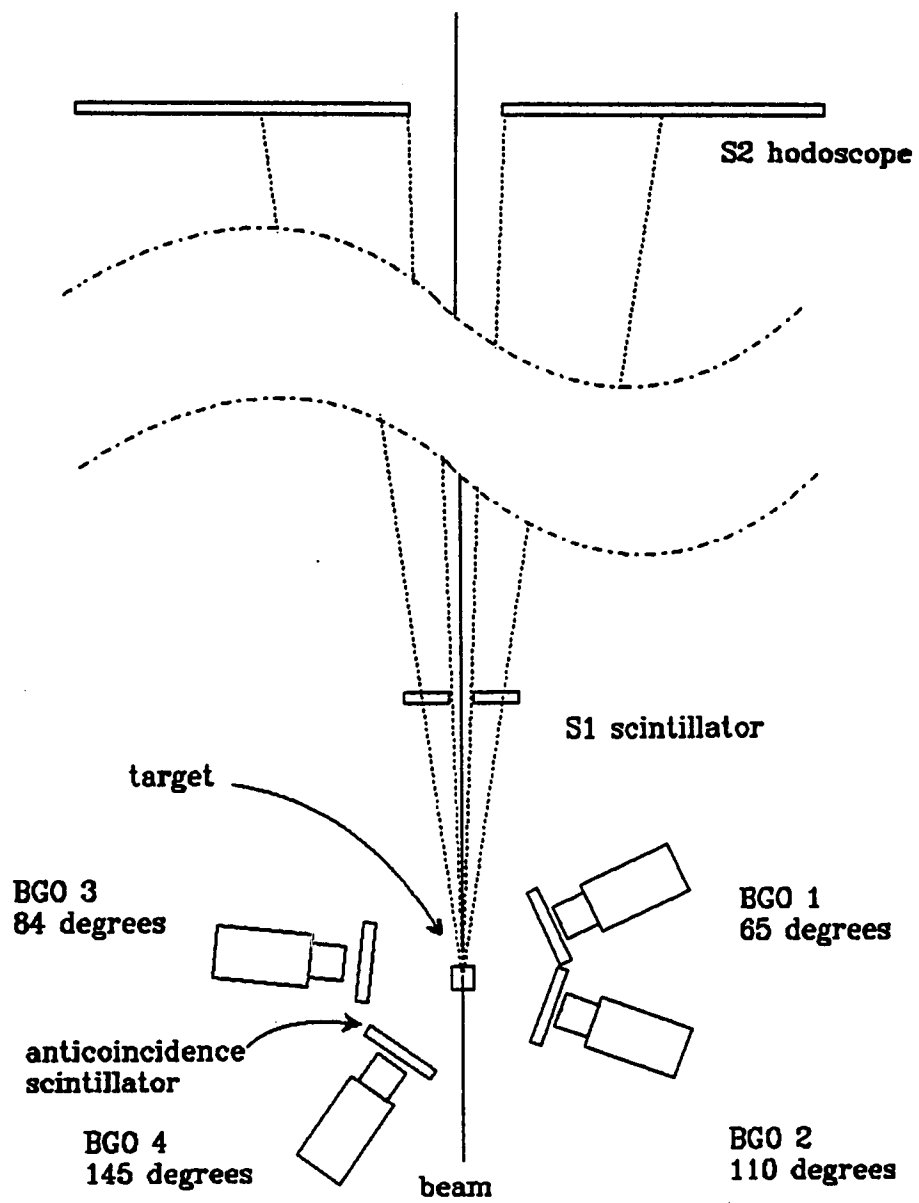


Figure 3-2: Schematic plan view of experiment 832.

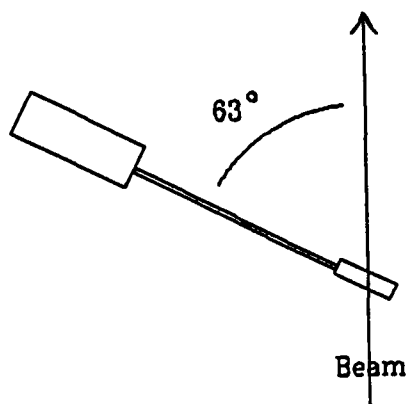


Figure 3-3: Target and target-changer.

### 3.1.1 Scattered Proton Detection

The scattered proton was detected by a plastic scintillator S1 located 18 inches downstream of the target, in coincidence with a plastic scintillator hodoscope S2 whose side nearest the target center was located  $82 \frac{1}{8}$  in. downstream of the target center (This was for the 1985 data. For summer 1986 this measurement was recorded to be  $81 \frac{1}{4}$  in. and for fall 1986 it was recorded to be  $82 \frac{3}{8}$  in.) S1 was a  $\frac{3}{8}$  in. thick circular scintillator centered around the beam with a hole in its center to allow the beam to pass through without firing it. It was located 18 in. downstream of the target center. The outer diameter of S1 was 9 in. and the diameter of the inside hole was  $1 \frac{1}{2}$  in.

S2 was made up of  $8 \frac{3}{8}$  in. thick "phi" scintillator paddles and labeled P1 to P8 (see figure 3-4), and three "ring" scintillators called R1 to R3 (see figure 3-5). The phi paddles overlapped in such a way as to form 16 different azimuthal angle elements. The ring scintillators overlapped to form five different polar or  $\theta$  angle elements. It was necessary to make v-shaped cuts in the ring scintillators where the light guides were attached to allow light to be reflected to the light guides and PMT's (see figure 3-5). The ring scintillators were attached on the upstream side of the aluminum frame that supported the hodoscope and the phi paddles were attached on the downstream side so that there was an additional  $8 \frac{1}{16}$  in. from the upstream side of R1 to the middle plane of the phi scintillators. The diameter of the hole in the center of S2 for the beam

BGO	Fall 1985		Summer and Fall 1986	
	angle	distance	angle	distance
1	69°	7 7/8 in.	65°	8 11/16 in.
2	117°	7 7/8 in.	110°	8 7/16 in.
3	89°	8 9/16 in.	84°	8 1/4 in.
4	131°	8 7/16 in.	145°	9 1/2 in.

Table 3-1: BGO angles relative to beam direction and distances from the front face to the target center.

was 10 1/2 inches. The lower limit of polar angle for protons detected by S2 was 3.33° for the fall of 1985, 3.36° for the summer of 1986, and 3.32° for the fall of 1986.

The discriminator thresholds were set by observing the “band” of pulses from elastic protons on an oscilloscope and setting the thresholds below this level. The same method was used for the BGO anticoincidence scintillators mentioned below in section 3.1.2.

As can be seen in figure 3-4, the outer edge of the scintillating material for the phi paddles is not circular, and this means that the maximum polar angle varies somewhat with the azimuthal angle  $\theta$  around the beam direction. The distance from the beam center to the outer edge of the scintillating material for the S2 paddles ranged from 16 1/2 in. to 18 15/16 in., so that the maximum polar angles of protons for a given azimuthal angle  $\phi$  ranged between 10.39° and 11.84° for data from the fall of 1985, between 10.49° and 11.96° for data from the summer of 1986, and between 10.36° and 11.81° for data from the fall of 1986. An additional problem is that small areas in the outer corners of the scintillating areas of each paddle are assigned the wrong  $\phi$  angle. Referring to figure 3-4, if a proton passes through one of the 16 small triangles in the outer corners of the paddles, it will be assigned a wrong  $\phi$  angle. For example, a proton passing through the triangle at the top left-hand side of P8 will fire P8 but not P1, since

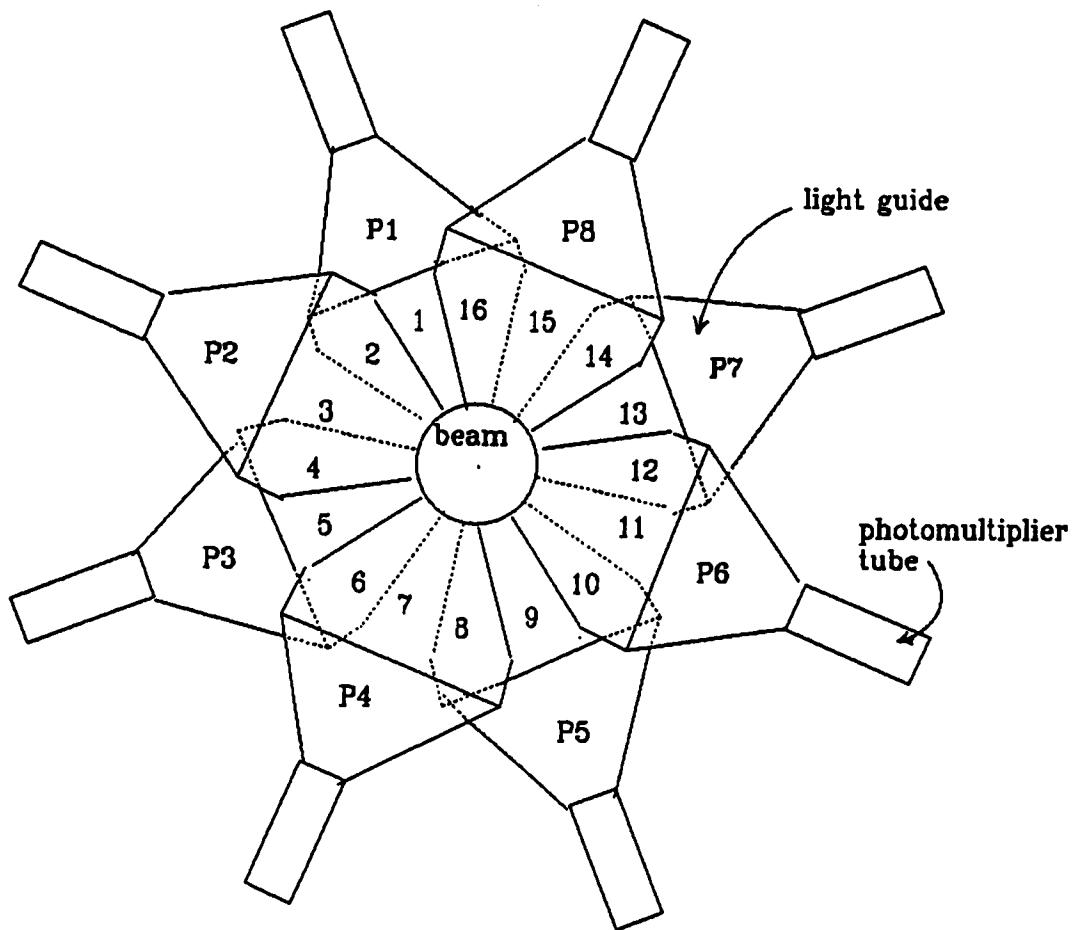


Figure 3-4: Schematic drawing of the phi paddles part of S2.

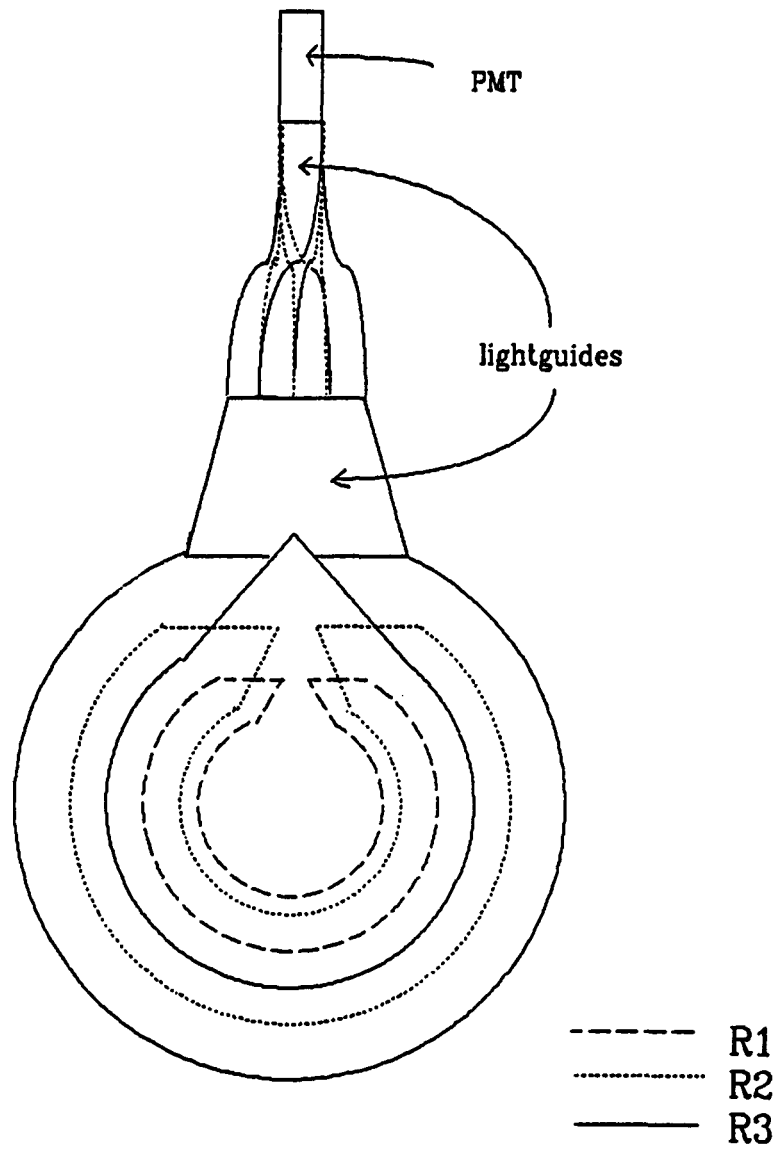


Figure 3-5: Schematic drawing of the ring detectors part of S2. The light guides and photomultiplier tube for R3 is shown, with R1 and R2 having similar arrangements.

it only passes through P1's light guide, and so will be included in  $\phi$  angle element 15, whereas this angle element should properly be 16. The combined area of these triangles represents only 5.08% of the total scintillating area for all the paddles. Since also the cross section for 15.11 MeV production falls off rapidly with scattering angle, and these triangles are located at the maximum polar angles, this effect is reduced to 2.3%.

### 3.1.2 $\gamma$ -ray Detection

The second arm of the experiment for the detection of the  $\gamma$ -ray from the de-excitation of the 15.11-MeV state consisted of four identical BGO detectors (bismuth germanate,  $\text{Bi}_4\text{Ge}_3\text{O}_{12}$ ). The BGO crystals were cylinders 3 in. in diameter by 3 in. deep. They were positioned in a horizontal plane around the target, with BGO's 1 and 2 on the right side looking downstream at angles of  $69^\circ$  and  $117^\circ$  respectively relative to the beam direction, and BGO's 3 and 4 on the left side at angles of  $89^\circ$  and  $131^\circ$  respectively. These angles are the ones for the fall of 1985. For both summer and fall of 1986 the angles changed to BGO 1:  $65^\circ$ , BGO 2:  $110^\circ$ , BGO 3:  $84^\circ$ , BGO 4:  $145^\circ$ . The distances between the front faces of the BGO's and the target center also were different for 1985 and 1986. These distances are given in table 3-1 along with the BGO angles.

Each BGO had a plastic scintillator in front of it to veto charged particles (anticoincidence scintillators or "Anti's").

### 3.1.3 Polarization and Beam Current

The  $\text{P}^-$  beam originates from a Lamb-shift ion source which uses cesium vapor to donate electrons selectively to hydrogen atoms in the 2S state, and then a "nuclear spin filter" to filter out one electronic spin state to which the spin of the proton is coupled. In this filter, electric and magnetic fields selectively cause the 2S atoms to decay to the ground state, or "quench," depending on the spin state of the nucleus and the electron. Finally, collisions with argon gas add electrons to produce  $\text{H}^-$  ions. The electrons are

removed in stripping foils and the spin is precessed before entry into the EPB area, as shown in Figure 3-1. The direction of polarization changed on a two minute cycle—*i.e.* there was approximately 1 minute 45 seconds of normal polarization followed by  $\sim$  15 seconds when the source was quenched, followed by 1 minute 45 seconds of reverse polarization, *etc.*

The direction of polarization, normal, sideways, and longitudinal, is controlled by the EPB spin precessor magnets. Information on the magnitude of the beam polarization was provided by the LAMPF beam-line polarimeters EP and LB, which employed plastic targets ( $\text{CH}_2$ ) and scintillators positioned at the correct angles for the  $(p, 2p)$  reaction in both vertical and horizontal directions. At the time the experiment was done the polarization was available as an averaged figure per hour, which included both normal and reverse time periods. It was estimated that the difference between normal and reverse polarization at any one time is less than 2 % [vD90].

The beam current was monitored by our scintillators and by the LAMPF ion chamber EPIR-01, situated about 3 feet downstream of S2. The calibration of the ion chamber was 1.4 picocoulombs/count. The choice of scintillators for additional monitoring of the beam current requires some care so that the specific monitors are polarization independent. Because of parity constraints, for normal polarization there is no N (normal or spin-up) *vs.* R (reverse or spin-down) asymmetry expected in the top or bottom direction of S2 (*i.e.* P1, P8, P4, P5) and so these scintillators may be used to monitor the ratio N/R of beam current that is needed in the analysis. For normal polarization it is expected that the ring detectors can also be used, since efficiency differences are expected only in the top *vs.* bottom of the rings because of their left-right geometric symmetry. For the same reasons the ring detectors cannot be used to monitor N/R for sideways and longitudinal polarization directions because for these directions asymmetries are expected in the top and bottom parts of the rings which combined with

differences in efficiencies for these parts of the rings would give erroneous N/R values for beam current. For sideways and longitudinal polarization, P2, P3, P6, and P7 may be used.

### 3.2 Data Acquisition

Data were taken using the "Q" data acquisition system at LAMPF and a VAX 750 computer using the VMS operating system. NIM electronics and CAMAC were used and an MBD ( Micro-programmable Branch Driver) interface between the CAMAC and the VAX. Besides a scaler event (event 11), three data events were taken in 1985 and two events in 1986. For both years an event 10 was a coincidence of a scattered proton ( $S1 \cdot S2$ ) and a  $\gamma$ -ray ( $G \cdot \bar{A}$ ), and event 8 was a prescaled proton single event ( $S1 \cdot S2$ ). In 1985 an event 6 was also taken that was a BGO single event ( $G \cdot \bar{A}$ ). CAMAC scalers were taken of all scintillators, the 4 BGO's, a clock, and the ion chamber, as well as the output from several discriminators in the electronics. A number of scalers were taken both with and without a "computer busy" inhibit, in order to monitor dead time. The Q system provided on-line analysis capability during the experimental runs and all the information was recorded on magnetic tape for further analysis off-line.

### 3.3 Electronics

Figure 3-6 shows the electronics for the S2 phi paddles. The monitor output of the CFD ( constant fraction discriminator) was used as the input for the two scintillator ADC's, PO and PE (the logical sums of the odd and even phi paddles respectively). Not shown in figure 3-6 was an output from each of the 8 paddle CFD's which were inputs to the Bit Register. ( Outputs of the CFD's which went to CAMAC scalers are also not shown.) The Q system analyzer used the bits set in the Bit Register on each event to determine which of the even-numbered paddle the PE ADC reading belonged to, and similarly for the PO ADC. The same strategy was used for the TDC PO and

PE stops.

Shown in figure 3-7 is the logical circuitry for the event triggers. As in the case of the phi CFD's, the Monitor output from the S1 CFD was used as the input to the S1 ADC. The start of all the TDC's was set by S1's firing (as validated by the other requirements for either a good event or an S1-S2 singles event).

Figures 3-8 and 3-9 show the BGO electronics for 1985 and 1986, respectively. The upper level discriminator ( UL) was set with a high threshold to veto large pulses from high energy neutral particles. The T (timing) CFD had a narrow width (20 ns) output so that BGO timing would be controlled by it. The E (energy) discriminator had its threshold set between 4.4 MeV and 15.1 MeV and was intended to suppress low energy pulses. This was taken out of coincidence in one beam macro-pulse out of 10 ( this was changed in the fall of 1986 to 2 out of 10) in order to accumulate a spectrum of the 4.4 MeV excited state of  $^{12}\text{C}$ , although pre-scaled since the 4.4 MeV state has a much higher production cross section.

The pile-up circuit set a bit in the Bit Register so that pileup could be handled in software. The signal for the pile-up circuit was put into coincidence with a delayed copy of itself, as shown in Figures 3-8 and 3-9.

In the fall of 1986 Anti's 2 and 3 were rewired so that instead of having a hardware veto into the coincidence unit, they set a bit and charged particles were vetoed in software. This was so that the BGO response to charged particles could be investigated in work not directly related to this experiment.

### 3.4 Calibration of the BGO Energy Spectra

Calibration of the ADC energy spectra was done with two sources, a Pu-Be source yielding a 4.4 MeV transition from carbon, and the other one yielding the 6.13 MeV transition from  $^{16}\text{O}$ . These calibration measurements were taken with the beam off at different times during each run, and with the sources located near the target position.

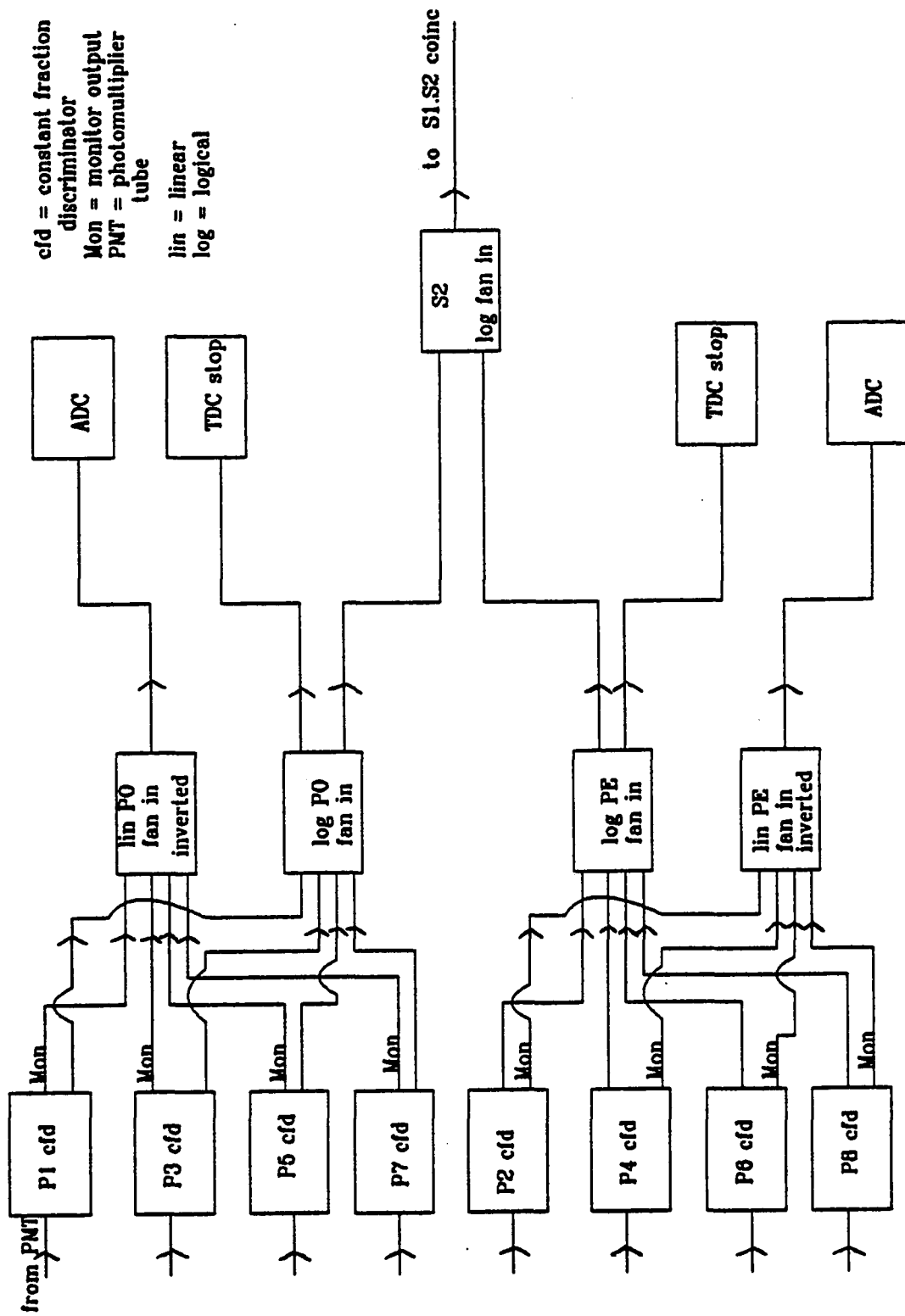


Figure 3-6: S2 electronics.

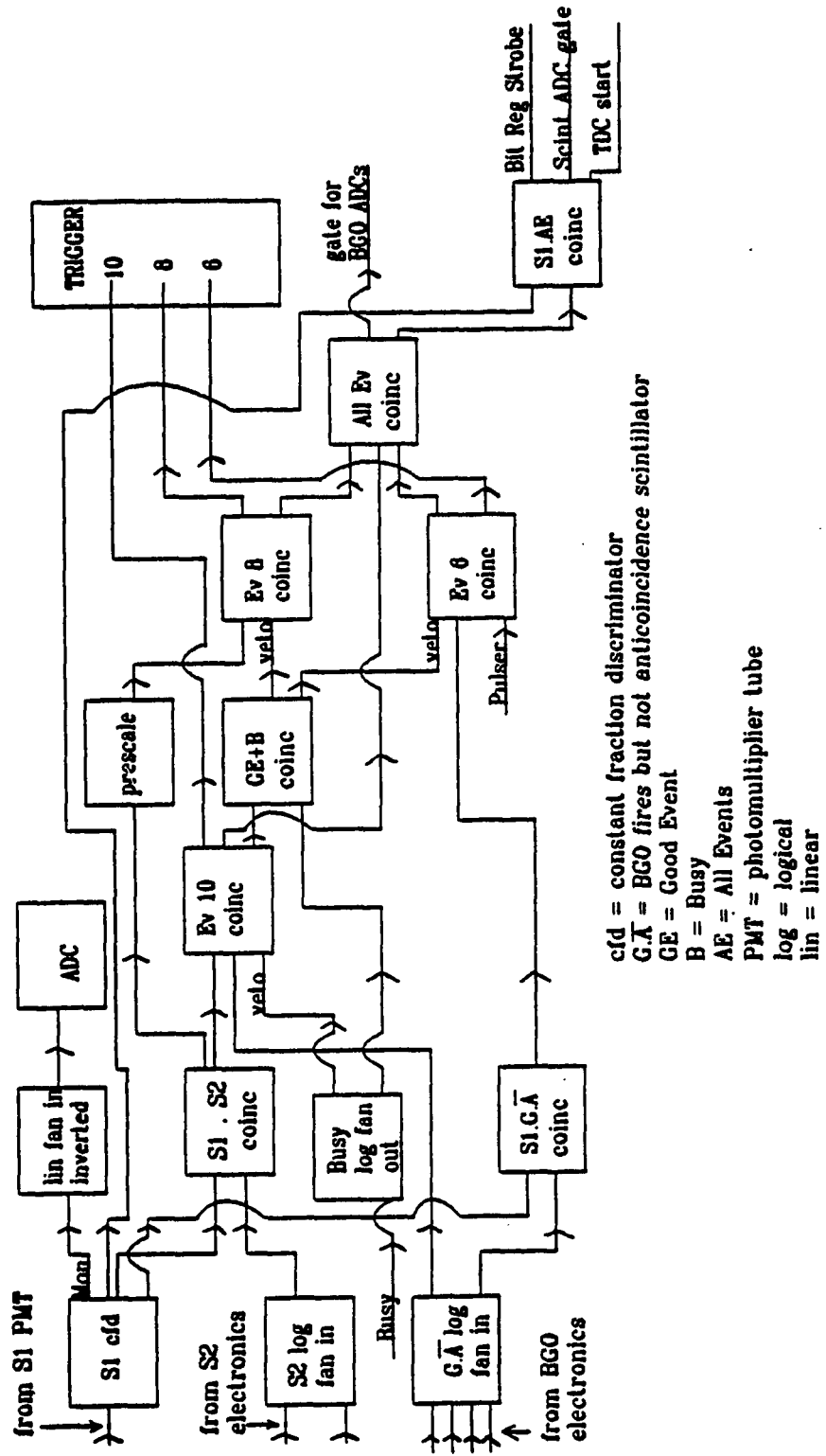


Figure 3-7: Schematic diagram of the events triggers.



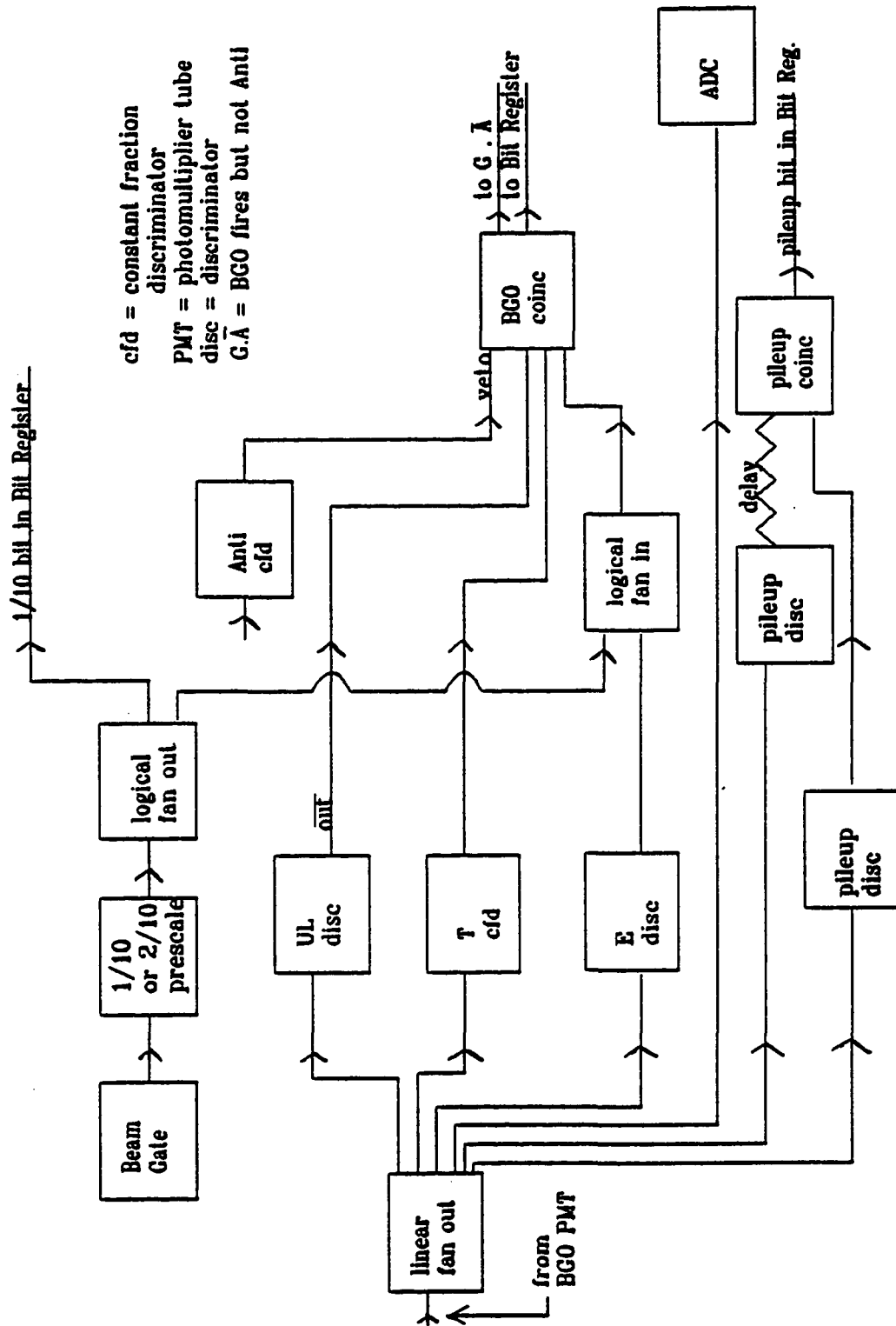


Figure 3-9: BGO electronics in 1986.

## Chapter 4

### Data Analysis

The data analysis for experiment 832 was complex, and was mainly directed toward measuring coincident analyzing powers or asymmetries of the reaction  $^{12}\text{C}(p, p'\gamma)^{12}\text{C}^*$  (15.11 MeV). A secondary goal was to determine the angular correlation function  $W(\theta_\gamma, \phi_\gamma)$  for this reaction. We also looked at the same quantities for protons scattered to the 4.44-MeV state of  $^{12}\text{C}$ . As we will see, problems prevented our achieving any but the primary goal. This chapter will describe the data analysis for these efforts.

#### 4.1 Data Analysis Hardware and Software

The bulk of the off-line analysis was done on a NAS 6660 and IBM 4381, using the IBM MVS operating system. Some calculations and graphics work were also done on the William & Mary Medium Energy Group Microvax II computer, and a few calculations were done on an IBM-compatible PC. To read the tapes written by the Q data acquisition system at LAMPF and to convert them to a form readable by the IBM system (which involved flipping the order of bytes in the data words) the program FLIPBYTE, written by Don Joyce, was used [Joy82], which was modified as needed by the author. Further analysis was performed by a FORTRAN77 program which incorporated some elements of the on-line analyzer program written by B.J. Lieb and J.R. Mackenzie [LM85], with the rest being written by the author. This program, called IBMQ, was able to emulate the Q on-line system in the sense that it could read Q system input files and gave output in the same format, *i.e.* the Q system test package output. Histogram plotting and fitting capability was handled by the CERN HBOOK and HPLOT packages on the IBM system [BIPL]. Some Monte Carlo simulations that were an integral part of the

data analysis were done on the Microvax using EGS4 [NHR85], a standard electron and  $\gamma$  simulation package. Some three-body calculations were done on a modified version of a program written by G.P. Pepin. Some Monte Carlo programs were written by the author, two of which will be described below and are included as Appendices B and C.

#### 4.2 Coincidence Analyzing Powers of $^{12}\text{C}(p, p' \gamma)^{12}\text{C}^*(15.11 \text{ MeV})$

The main quantities measured in this experiment were the  $\gamma$ -ray proton coincidence analyzing powers or asymmetries  $A_n^{coinc}$ ,  $A_s^{coinc}$ ,  $A_l^{coinc}$  corresponding to the three mutually perpendicular directions of incident beam polarization: normal (vertical), sideways (horizontal and perpendicular to the beam), and longitudinal (along the beam direction):

$$A_i^{coinc}(k_p, k_\gamma) = \frac{\left(\frac{d^2\sigma}{d\Omega_\gamma d\Omega_p}(k_p, k_\gamma)\right)_\uparrow - \left(\frac{d^2\sigma}{d\Omega_\gamma d\Omega_p}(k_p, k_\gamma)\right)_\downarrow}{p \left(\left(\frac{d^2\sigma}{d\Omega_\gamma d\Omega_p}(k_p, k_\gamma)\right)_\uparrow + \left(\frac{d^2\sigma}{d\Omega_\gamma d\Omega_p}(k_p, k_\gamma)\right)_\downarrow\right)}, \quad i = n, s, l \quad (4-1)$$

where  $p$  is the magnitude of the beam polarization. These are coincidence measurements involving double differential cross sections and so for each BGO there is one measurement for each direction of scattered proton (8 different directions as discussed below in section 4.2.3), and direction of incident beam polarization, for a possible total of 96 measurements ( $4 \times 8 \times 3$ ). The double differential cross sections in equation 4-1 involve a measurement of the size of the 15.11-MeV peak in the BGO spectrum for both  $\uparrow$  (normal) and  $\downarrow$  (reverse), S1 and S2 detector and electronics efficiencies, the efficiency of the BGO, beam current measurements for  $\uparrow$  and  $\downarrow$ , solid angles for S2 and BGO, the time over which the measurements were taken, and the number of nuclear scattering centers involved. However, many of these factors cancel since they are present homogeneously in the numerator and the denominator, and if we let  $N$  represent the size of the 15.11-MeV peak with  $\uparrow$  or normal polarization and  $R$  be the size of the peak with  $\downarrow$  or reverse polarization, and  $M_N$  and  $M_R$  be scaler monitors proportional to the beam

current for the two polarizations, then:

$$A_i^{coinc} = \frac{1}{p} \left( \frac{N - (M_N/M_R)R}{N + (M_N/M_R)R} \right) \quad i = n, s, l.$$

We will consider each element on the right hand side.

#### 4.2.1 Polarization

Beam polarizations were supplied by LAMPF using the LAMPf beam-line polarimeters on an hourly basis. These measurements were averages over the hour and were the same for both  $\uparrow$  and  $\downarrow$  to within 2% [vD90]. In computing the asymmetries for a particular polarization the average value of the polarization was used for the entire time that data was taken for that polarization, calculated from the hourly values supplied by LAMPF which were weighted by beam current as determined by scaler monitors. This is in contrast to determining the value of

$$A_j = \frac{1}{p_j} \left( \frac{N_j - (M_N/M_R)R_j}{N_j + (M_N/M_R)R_j} \right)$$

for each time interval  $j$  for which we have polarization values, and averaging these values to find

$$A = \frac{1}{N} \sum_j A_j \quad .$$

The validity of this approximation is discussed in appendix A. For normal polarization the scalers used were  $(P1 + P8)/2$ ,  $(P4 + P5)/2$ , R1, R2, and R3 , and for sideways and longitudinal polarization  $(P2 + P3)/2$  and  $(P6 + P7)/2$ . The reasons for the choice of these scalers was discussed in section 3.1.3 and will be further discussed in the next section.

#### 4.2.2 Beam Current Correction and Scalers

The scalers were used to monitor beam current and also as a general check on how the experiment was working. Scaler events (Event 11) were taken every 10 seconds for the 1985 and summer of 1986 data, and every second for the fall of 1986 data. The

double differential cross sections that determine the coincidence analyzing powers which we measured can be expressed as

$$\frac{d^2\sigma}{d\Omega_p d\Omega_\gamma} = \frac{kN_\gamma}{M}$$

where  $N_\gamma$  is the number of events in the 15.11-MeV peak for the cross-section measured,  $M$  is the scaler used as the beam current monitor, and  $k$  is a constant which contains detector efficiencies, the target thickness, the density of  $^{12}\text{C}$ , and other conversion factors. That is, if  $N_{inc}$  is the total number of incident protons in the beam,  $t$  is the time over which the data is taken,  $\rho$  is the density in  $\text{g/cm}^3$  of  $^{12}\text{C}$ ,  $d$  is the target thickness,  $N_A$  is Avogadro's number,  $\eta_\gamma$  and  $\eta_p$  the BGO and S1-S2 efficiencies,  $S$  is the beam spot area,  $A$  is the atomic weight of  $^{12}\text{C}$ , and  $M = hN_{inc}$  where  $h$  is a proportionality constant, then

$$\begin{aligned} \frac{d^2\sigma}{d\Omega_p d\Omega_\gamma} &= \frac{\text{number scattered/sec}}{\text{incident flux} \cdot \text{scattering centers}} \\ &= \frac{\text{number scattered}/t}{\left(\frac{N_{inc}}{tA} \frac{Sd\rho N_A}{A}\right)} \\ &= \frac{N_\gamma/\eta_\gamma\eta_p}{\frac{M}{h} \frac{d\rho N_A}{A}} = \left(\frac{hA}{d\rho N_A\eta_\gamma\eta_p}\right) \frac{N_\gamma}{M} = \frac{kN_\gamma}{M} \end{aligned}$$

If  $N$  and  $R$  are the numbers measured in the 15.11 MeV peak for normal and reverse (spin-up and spin-down) beam, and  $M_N$  and  $M_R$  are their corresponding beam monitors,

$$A^{coinc} = \frac{kN/M_N - kR/M_R}{p(kN/M_N + kR/M_R)} = \frac{N - QR}{p(N + QR)} \quad \text{where } Q = M_N/M_R. \quad (4-2)$$

This brings us to the question of which (spin-independent) scaler or combination of scalers to use for the ratio  $Q$ . If  $M_g$  refers to a beam monitor that is gated by "computer-not-busy," which we will refer to as a gated scaler, and  $M_u$  to one which is ungated, the choice for the  $M$  in the denominator of each cross section should be  $M_u$  since the cross section is computed using the total beam flux. However the  $N_\gamma$  in the numerator will need to be corrected for dead-time:

$$\frac{d^2\sigma}{d\Omega_p d\Omega_\gamma} = \frac{kN_\gamma(M_u/M_g)}{M_u} = \frac{kN_\gamma}{M_g}$$

Therefore the correct result will be obtained by using a gated monitor. The gated scalers that were recorded were scalers for all scintillators including the BGO's, a 1 MHz clock, the logical sum of the even-numbered paddle scintillators PE, the ion chamber BEAM (from EPIR-01), and scalers for the number of good coincidence events (EVENT10), S2 single events (EVENT8) and BGO single events (EVENT6). A subset of these scalers was also recorded without the computer-busy gating.

The scalers were examined in some depth and a few problems were discovered. During run suspensions the scalers would continue to count and so the first scaler event following a run suspension or after the start of a new run was dropped.

It was found that for about 26% of the sideways data, the computer-busy wire that comes from the trigger module was disconnected at the trigger module. The ratio of the normal versus reverse scalers for this period was  $<1$ , *e.g.* for PE (the logical sum of the even-numbered phi paddles) it was 0.947. For a sample of other tapes from the same period in the fall of 1985 that had an ungated PE normal-to-reverse ratio of 0.959, the gated ratio for PE was 0.975. This makes sense because in this case reverse beam is higher on the average and should therefore be more affected by dead-time. Thus if  $M_{Ng}$  and  $M_{Rg}$  are gated scalers,  $M_{Nu}$  and  $M_{Ru}$  their ungated counterparts, and  $L_N$  and  $L_R$  the corresponding live times (percent not busy):

$$\frac{M_{Ng}}{M_{Rg}} = \frac{L_N M_{Nu}}{L_R M_{Ru}} > \frac{M_{Nu}}{M_{Ru}}$$

since  $L_N > L_R$ . Thus we can expect that the normal-to-reverse ratio for the busy-disconnected data would likewise be about 1.5% higher. If the asymmetries of

$$\frac{1}{p} \left( \frac{N - QR}{N + QR} \right)$$

are regarded as a function of  $Q$ , a Taylor expansion can give us an idea of what effect this will have on our results:

$$f(Q) = f(\Delta Q = 0) + \frac{1}{p} \left( \frac{-(N + QR)R - (N - QR)R}{(N + QR)^2} \right) 0.015 + O(\Delta Q^2)$$

$$\cong f(\Delta Q = 0) - \frac{2NR}{p(N + QR)^2} \times 0.015$$

As a rough approximation let  $N=R=QR$ ,  $p=0.8$ . Then

$$f(Q) = f(\Delta Q = 0) - \frac{0.015}{0.8 \times 2} = f(\Delta Q = 0) - 0.009$$

This shows that the effect on our asymmetries is expected to be less than 1%. Since only 25% of the sideways data is so affected, and this would further decrease the effect on the results, it was decided not to exclude that data.

One positive result of having the busy disconnected during the sideways data was that it allowed us to compare the various scalers used as dead-time monitors and assess their reliability. With the busy disconnected, a plot of percent-live-time (*i.e.* percent of the time the computer is not busy, as measured by the ratio of a gated divided by an ungated scaler) vs. time should have resulted in 1 for all times, yet percent-live-time plots for several scalers did not show this. Figure 4-1 shows percent-live-time plots versus time for the end of the period when the busy was disconnected (it was reconnected at approximately minute number 5030). For S1, A2, and A3, where the percent-live-times were not equal to 1, the gated and ungated inputs to their scalers came from different discriminators or linear fan-outs. Either a difference of efficiency between these modules or of the scalers themselves may explain why percent-live-time is not recorded as 1 with busy disconnected. PE, the clock, and BEAM all had a reading of 1. The busy wire was also disconnected for a short time in some data that was not used in the fall of 1986 and showed the same pattern for the various scalers as the fall of 1985 data. Although when busy was disconnected the clock showed a percent-live-time of 1, it consistently showed higher percent-live-time when the busy was connected. This was probably due to the fact that there was a gate on the clock which was of somewhat longer duration than the beam was on, and accordingly the clock was counting part of the time when the beam was off and during that time the percent-live-time would be considerably higher.

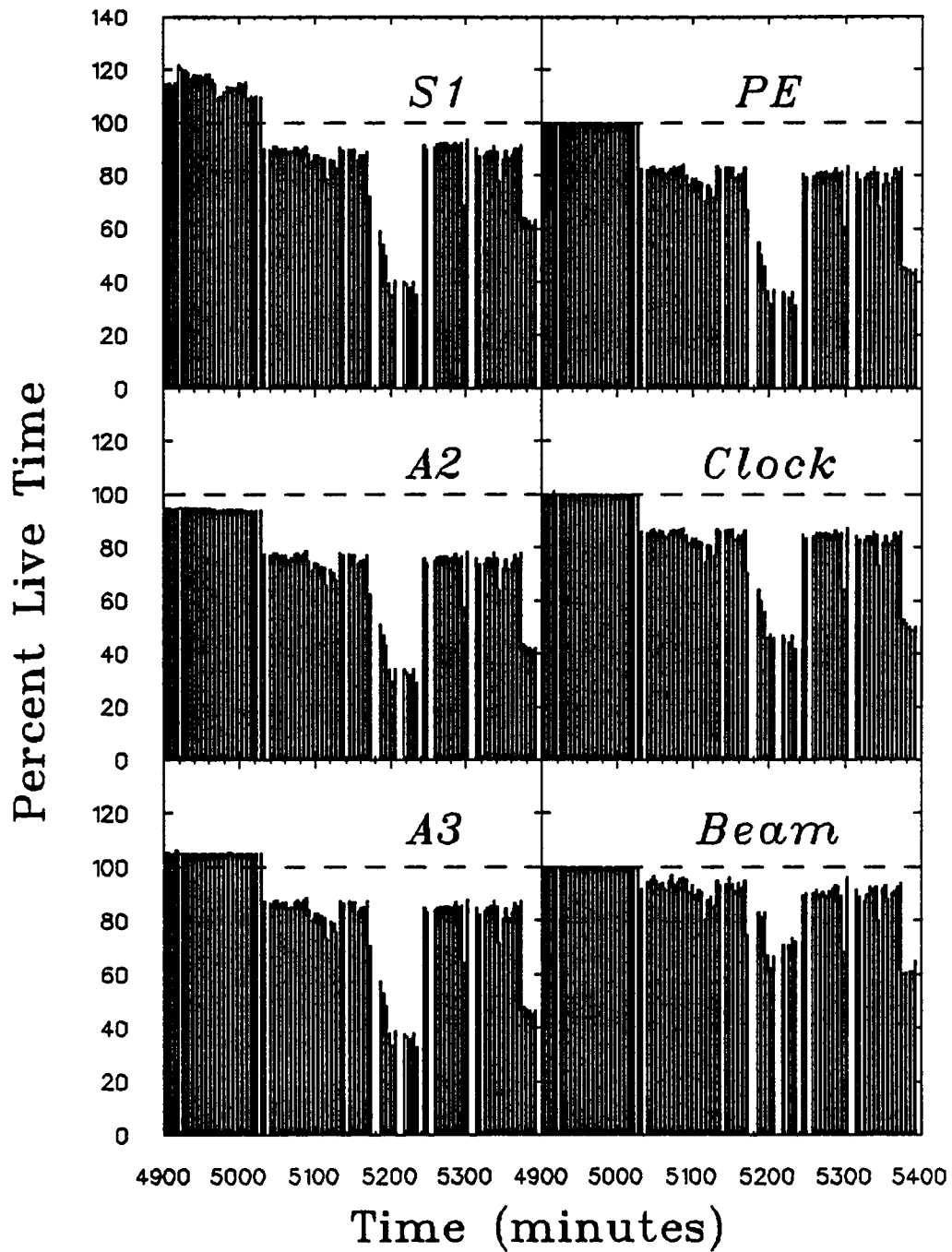


Figure 4-1: Percent-live-times of various scalers. The busy wire is disconnected for the times on the left-hand side of these plots, until minute number 5030. During this time the scalers should read one, but scalers *S1*, *A2*, and *A3* do not.

When the scaler totals during two-minute polarization cycles (of spin-up or spin-down) were plotted versus the ion chamber readings for the same cycles, a saturation of scaler S1 was revealed when S1 had more than  $6.5 \times 10^6$  counts per two-minute period (see Figure 4-2 a); *i.e.* for periods of higher beam the response did not show the expected linearity. Other scalers such as S1-S2, EVENT10, and EVENT8, which depend on S1, show the same effect. This leveling off takes place at about 6.5 pA of beam current. From Figure 4-2 we can estimate the frequency of S1:

$$\frac{6.5 \times 10^6 \text{ counts in S1 per 2 minute period}}{3.0 \times 10^6 \text{ counts in clock per 2 minute period} \times \frac{1}{10^8} \text{ sec per clock count}} = 2.2 \text{ MHz}$$

Taking the inverse of this to find the discriminator input pulse length for the maximum counting rate, we find a pulse length of 440 nsec, which is considerably longer than the 70 ns maximum length of the S1 phototube output pulse, and therefore saturation of S1 from pile-up is not the problem. An alternate explanation of the leveling out of S1 is a "sagging" of the photomultiplier tube, where an excess of current in the phototube dynodes lowers the DC voltage, resulting in output pulses of too small an amplitude to trigger S1's discriminator.

The beam current was monitored throughout all the runs and the only times when beam current was consistently high relative to the 6.5 pA level mentioned above was during the early part of fall 1986. This data has not been used for our results. Since at other times the beam generally stayed well below the 6.5 pA level, the data was not endangered from too high a beam current.

Another effect was noticed that explained some of the dependence of  $Q = M_N/M_R$  upon type of scaler used. Some of the scalers had a component of random coincidences, *e.g.* EVENT10 (good events) contain some random coincidences between BGO's and S1-S2 events. Since the singles rates for each of these is proportional to beam current, a part of EVENT10 is proportional to beam current squared. If  $M_N/M_R$  is greater than (less than) one for a scaler that contains no random coincidences, the same ratio for the

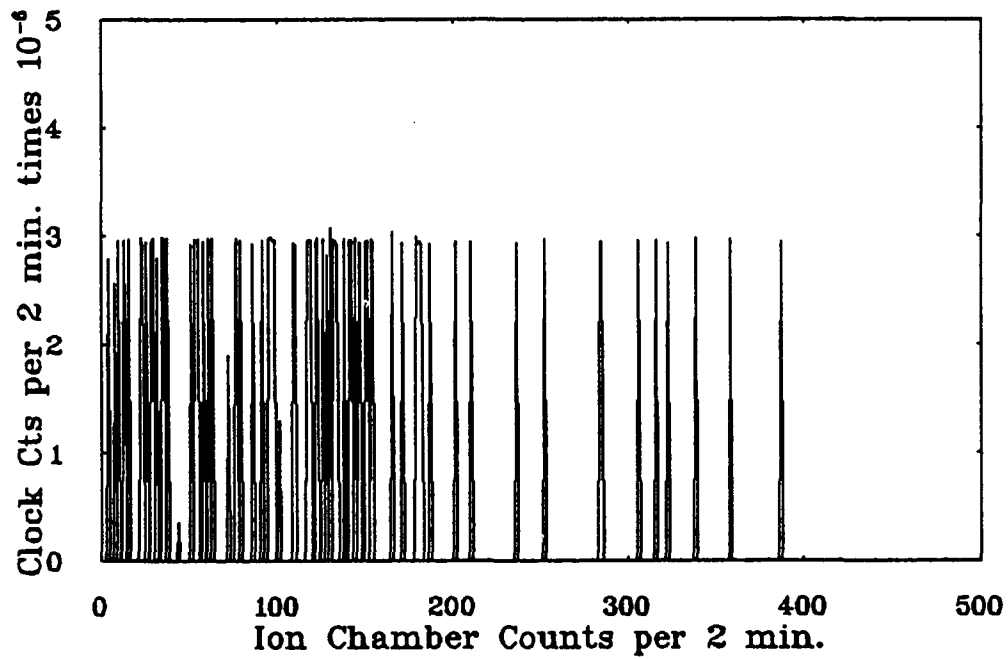
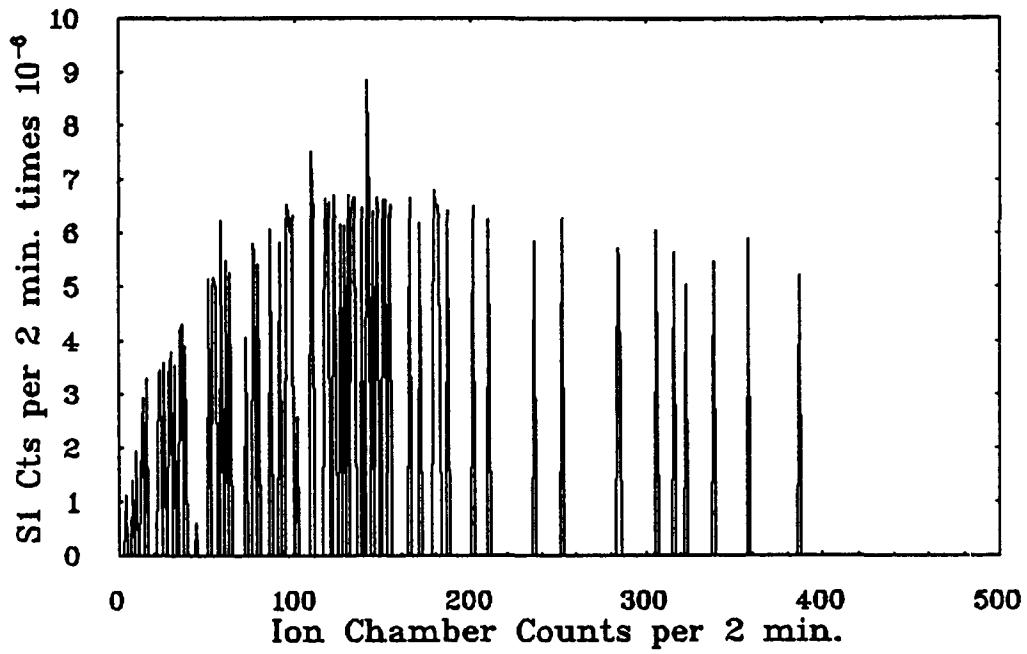


Figure 4-2: Average counts in two scalers vs. ion chamber counts for the same time.

randoms part of EVENT10 will be  $(M_N/M_R)^2$  which will be greater than (less than)  $M_N/M_R$ . The same effect was noticed for the ratio of the area of the background under the 15.11-MeV peak in the raw energy spectrum, which is mostly randoms.

The conclusion of these considerations, and of the need to choose polarization-independent beam monitors as discussed in Section 3.1.3, is that the scintillator paddles and rings were selected to use as beam current monitors. These do not contain random coincidences, are not affected by S1 saturation or sagging, and are not among the scalers shown to be suspect when busy was disconnected. An average of  $(P1 + P8)/2$ ,  $(P4 + P5)/2$ , R1, R2, and R3 was used for the normal polarization data, and for sideways and longitudinal an average of  $(P2 + P3)/2$  and  $(P6 + P7)/2$ . That is, the ratio of  $M_N/M_R$  was taken for each of these quantities and the results were averaged for the  $Q = M_N/M_R$  value for the asymmetries.

#### 4.2.3 Measurement of the 15.11-MeV Peaks

The BGO ADC spectra were analyzed and fitted to obtain the amplitudes N and R that were used to compute the asymmetries. In a few cases a BGO did not produce a useable spectrum: this was the case for BGO 1 in the summer of 1986 (longitudinally-polarized data) and for BGO's 1 and 3 in the fall of 1986 (normal polarization). The spectra in these cases were too broad to fit well. The cause of these failures was never determined.<sup>1</sup>

The scintillator arrangement of the S2 hodoscope, which included phi paddles and ring scintillators, enabled a determination of the polar angle of the scattered proton, to within 5 polar angle elements. Since the phi paddles determined the azimuthal angle of the scattered proton to within 16 angle elements, there were  $5 \times 16 = 80$  solid angle elements that were capable of being discriminated by S2. The software program was also

---

<sup>1</sup>The BGO's were not the same from run to run. For the fall of 1985 4 BGO's borrowed from Dr. Steve Wender of LANL were used. In summer of 1986 BGO's 1,2, and 4 were from Dr. Wender (which may not have been the same or may have been altered) and BGO 3 was a new Harshaw BGO belonging to Dr. Carey Stronach. In fall of 1986 4 Harshaw BGO's belonging to Dr. Stronach were used.

capable of producing a spectrum for any combination of these 80 solid angle elements. It was found, however, that there were not enough events in these individual elements to provide a good fit of the 15.11-MeV peak and so data from the different  $\theta$  elements were lumped together. This choice also allowed more data to be used since the ring detectors were not efficient. Samples of data from the different runs showed that for the fall of 1985 about 27% of the events that were good with respect to the phi paddles (*i.e.* either one paddle or 2 adjacent paddles firing) were not good with respect to the rings firing (had no ring firing or 2 non- adjacent rings firing). The corresponding figure for summer of 1986 was 14% and 27% for fall of 1986. Part of this can be accounted for by the v-shaped cuts in the top of the rings.

A further improvement in statistics was made by combining data from 3 adjacent phi elements, so that data were grouped in sets where  $\theta$  ranged from  $3^\circ$  to  $11.7^\circ$  and phi over a  $67.5^\circ$  range. The different directions of phi presented in the results were  $45^\circ$  apart so that neighboring points on our asymmetry plots share data from one of the sixteen  $22.5^\circ$  phi elements. The somewhat arbitrary choice was made to analyze data in the 4 directions that make right angles with directions for normal and sideways beam polarization, *i.e.* the top of S2 (elements 1,15,16 in Figure 3-4), bottom (elements 7-9), right (elements 11-13), and left (elements 3-5). The  $45^\circ$  directions midway between these were also chosen: elements 1-3, 5-7, 9- 11, and 13-15 in Figure 3-4.

#### 4.2.3.1 Doppler Correction

$E_\gamma$  was Doppler corrected for the motion of the recoiling nucleus. Since for each good event we knew the angle of the scattered proton from knowing which phi paddles and rings fired, the angle and momentum of the recoiling carbon nucleus could be determined. If the angle between the direction of recoil of the  $^{12}\text{C}$  nucleus and the BGO which detected the 15.11 Mev  $\gamma$  is  $\theta$ , then the frequency of the  $\gamma$  will be changed from

the frequency  $f_0$  of a  $\gamma$  emitted from a stationary  $^{12}\text{C}$  by

$$f = \frac{\sqrt{1 - \beta^2}}{1 - \beta \cos \theta} f_0$$

Since energy is directly proportional to frequency, a correction of

$$\frac{1 - \beta \cos \theta}{\sqrt{1 - \beta^2}}$$

was applied to the ADC pulse-height values. This correction amounted to less than 1.5%, and was expected to be useful mainly in giving a slight improvement to quantities derived from combined spectra of all directions of scattered photon direction, such as the width and centroid position of the 15.11-MeV peak, rather than for spectra for any given direction of the scattered proton, since the data for these latter would all be corrected by Doppler correction factors with values quite close together.

#### 4.2.3.2 Temperature Corrections

BGO crystal response shows a substantial temperature dependence, which has been measured to be  $-1.55\%/^{\circ}\text{C}$  [BBB\*89]. Our data showed peak centroid variation that exhibited a diurnal pattern. The centroid variation in the fall of 1985 at times conflicted with what one would naively expect the temperature to be —*i.e.* the centroids had their lowest values at what one would expect the coolest part of the day would be in early December— in the morning between 4 and 8 a.m. However we did not take measurements of temperature during this run and that effect is probably due to artificial heating of the experimental areas. In the summer of 1986 we recorded the resistance values for a thermocouple located in the neighborhood of the target and BGO's, and the variations in BGO centroid positions for that run corresponded quite well with variations in temperature registered by our thermocouple. We conclude therefore that temperature was primarily responsible for the shifts in centroid that we saw.

We corrected the data for these temperature shifts by the following procedure. The BGO ADC spectra from the different time intervals, typically about four hours long,

were analyzed together, and a fit was made of the 15.11-MeV peak with an asymmetric gaussian (one with a different width on each side of the centroid) on top of a quadratic polynomial background. Data from these different time intervals were then summed after each spectrum was shifted so that the 15.11-MeV centroids lined up with one another (to within 4 channels— the binwidth of the ADC histograms). This shifting was most beneficial with the summer 1986 data where it resulted in a 38% decrease in the width of the BGO 2 peak, a 14% decrease in the width of the BGO3 peak, and a 20% decrease in the width of the BGO 4 peak.

#### 4.2.3.3 S2 Timing Cuts

Two TDC's recorded timing information relative to S1 for the S2 phi paddles, one for even-numbered paddles PE and one for odd-numbered paddles PO. The bit register was used to tell which paddle the TDC quantity belonged to. A correction for light-travel time inside the paddle scintillators was applied to the timing information by using the  $\theta$  information from the rings. The timing for each proton was normalized to be the same as though it had gone through the part of S2 nearest its center, *i.e.*  $\theta = 1$  (where  $\theta$  runs between 1 and 5 and represents the polar angle elements that can be distinguished by S2 – see Figure 3-5), by adding 5.89 channels times  $\theta - 1$  to the TDC readings. This number was arrived at by using an index of refraction for the scintillators of 1.58.

A typical timing spectrum for a paddle is shown in Figure 4-3, with the cuts indicated on the plot. A study was made of the BGO energy spectrum for eight subdivisions of this timing interval. It was found that the 15.11 MeV peak was evident through most of the large timing peak and was not noticeable in the last cut on the right-hand edge of the main peak. The cuts are shown in Figure 4-4 and some of the BGO ADC spectra generated for these cuts are shown in Figure 4-5. The 15.11-MeV peak is visible for some of the cuts at about channel 600. The spectra were fit with an asymmetric gaussian and a quadratic polynomial background, and the relative peak areas found are plotted

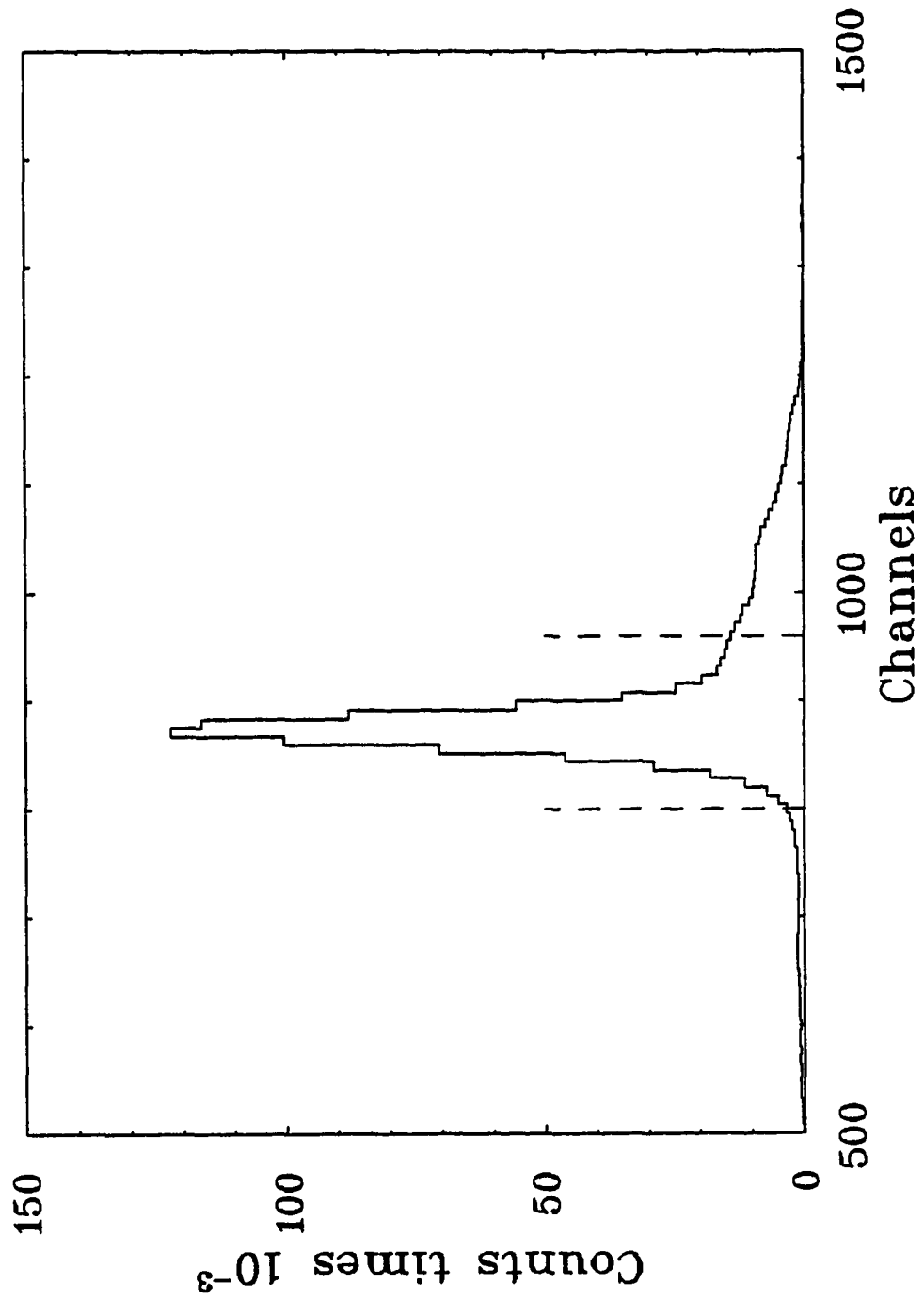


Figure 4-3: S1-S2 timing spectrum for P1 sideways polarization data.

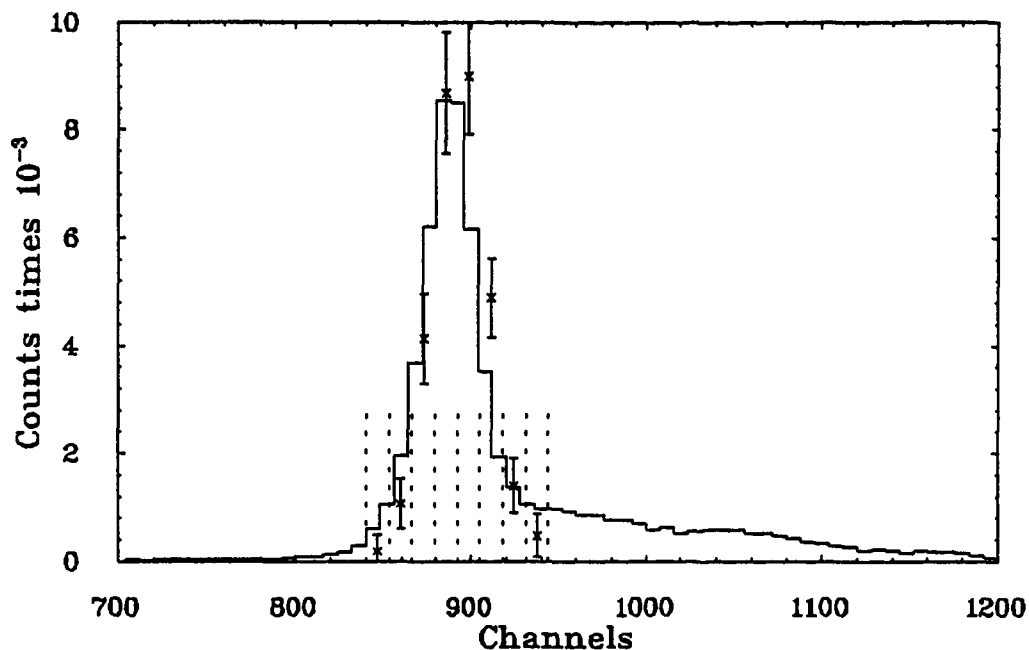


Figure 4-4: S1-S2 timing spectrum for data where the BGO ADC spectra (see Figure 4-5) were generated for each of the 8 small cuts indicated by the dotted lines. The crosses are the relative areas of the peak sizes found by a fitting procedure. See the text.

(with arbitrary normalization) as crosses in Figure 4-4.

A 3-body kinematical study of the reaction  $p + {}^{12}\text{C} \rightarrow {}^{11}\text{B} + p + p$  was done to see if the long tail on the right side of the main S1-S2 timing peak could be knocked-out or scattered protons. It was found that protons arriving in S2 by an amount of time corresponding to from 50 to 250 channels on the timing spectrum (1 channel represents 50 psec), or approximately in the region of the tail, are not kinematically allowed for Fermi momenta of the struck proton less than about 200 MeV/c, and that for struck proton Fermi momenta greater than this there is a minimum in this region of the proton energy spectrum compared with more energetic protons. Thus kinematic reasons make it unlikely that the tail is composed of protons. A second study was done with the same

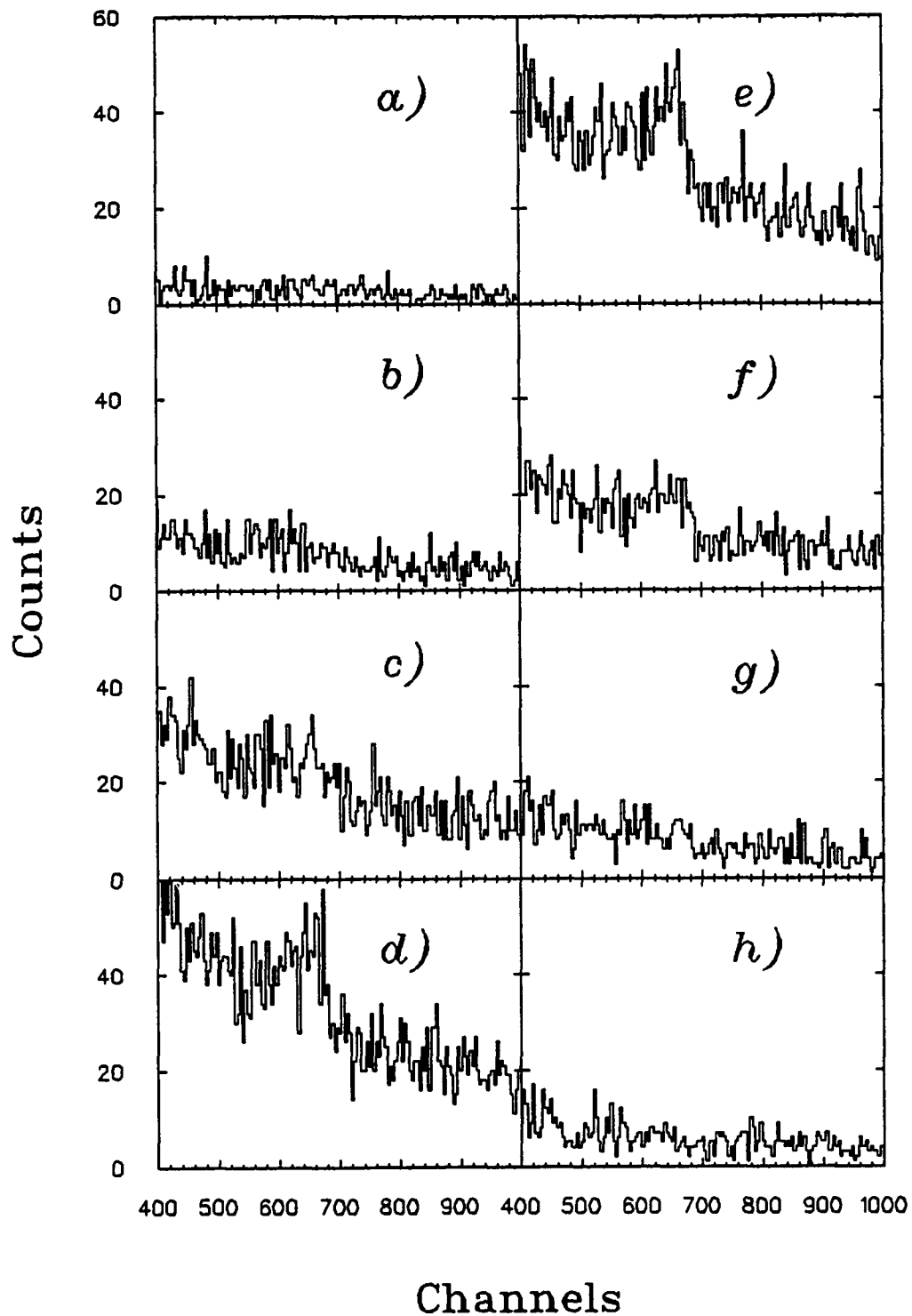


Figure 4-5: The BGO ADC spectra for the narrow timing cuts shown in Figure 4-4. The horizontal axis is in channels and the vertical axis is in counts. Part a) corresponds to the leftmost or first timing cut, b) is the second, etc. The 15.11-MeV peak (near channel 660) has been fitted as described in the text and the peak areas plotted in Figure 4-4.

program of the reaction  $p+^{12}\text{C} \rightarrow ^{10}\text{B}+d+p$  and it showed that knocked-out deuterons have a maximum for this range of times. It then appears that the tail is probably made up of knocked-out deuterons and  $\alpha$ 's or events with more than one particle knocked out.

We realized that a way to measure the timing resolution of our apparatus for S2 timing was to take a sample of events going through two overlapping paddles, put a narrow cut on the timing in one paddle (*e.g.* P1) and see how wide the distribution of times was for the other paddle (*e.g.* P2). When this was done with a 4-channel cut on P1 timing, the full width at half-maximum ( FWHM) of the roughly gaussian-shaped timing distribution in P2 ranged from 1.4 nsec for  $\theta = 1$  to 2.15 nsec for  $\theta = 3$  and 5. This 2 nsec resolution is equivalent to 40 channels and accounts for about 94% of the width of the main timing peak. Without the spread introduced by lack of exact timing resolution, the total spread of proton times for elastic protons ( 318 MeV) to those with least energy from exciting the 15.11 MeV state ( scattered into the maximum angle of S2 at  $11.2^\circ$ ) would be only 0.14 nsec or less than 3 channels. Therefore it is not possible to cut within the main peak to try to differentiate between elastics and excited bound states of  $^{12}\text{C}$ ; the broadness of the timing peak is also explained.

#### 4.2.3.4 Plastic Scintillator Pulse-height Information

The pulse height information of the S2 paddle scintillators was recorded in two ADC's, one for the odd-numbered paddles (PO)and one for the even-numbered ones (PE), and the bit register was used to determine which paddle the information belonged to. S1 had its own ADC to monitor pulse-height.

In Figure 4-6 are shown typical pulse-height spectra for a phi paddle and for S1. In Figure 4-7 is shown a scatter plot with P1 dE/dx plotted on the  $x$  axis and timing for P1 relative to S1 on the  $y$  axis. The timing cuts on P1 are indicated by solid lines on the plot. As was discussed above, the events for longer P1 times above the timing cuts are thought to be mostly deuterons or multiple knock-out events. The question of

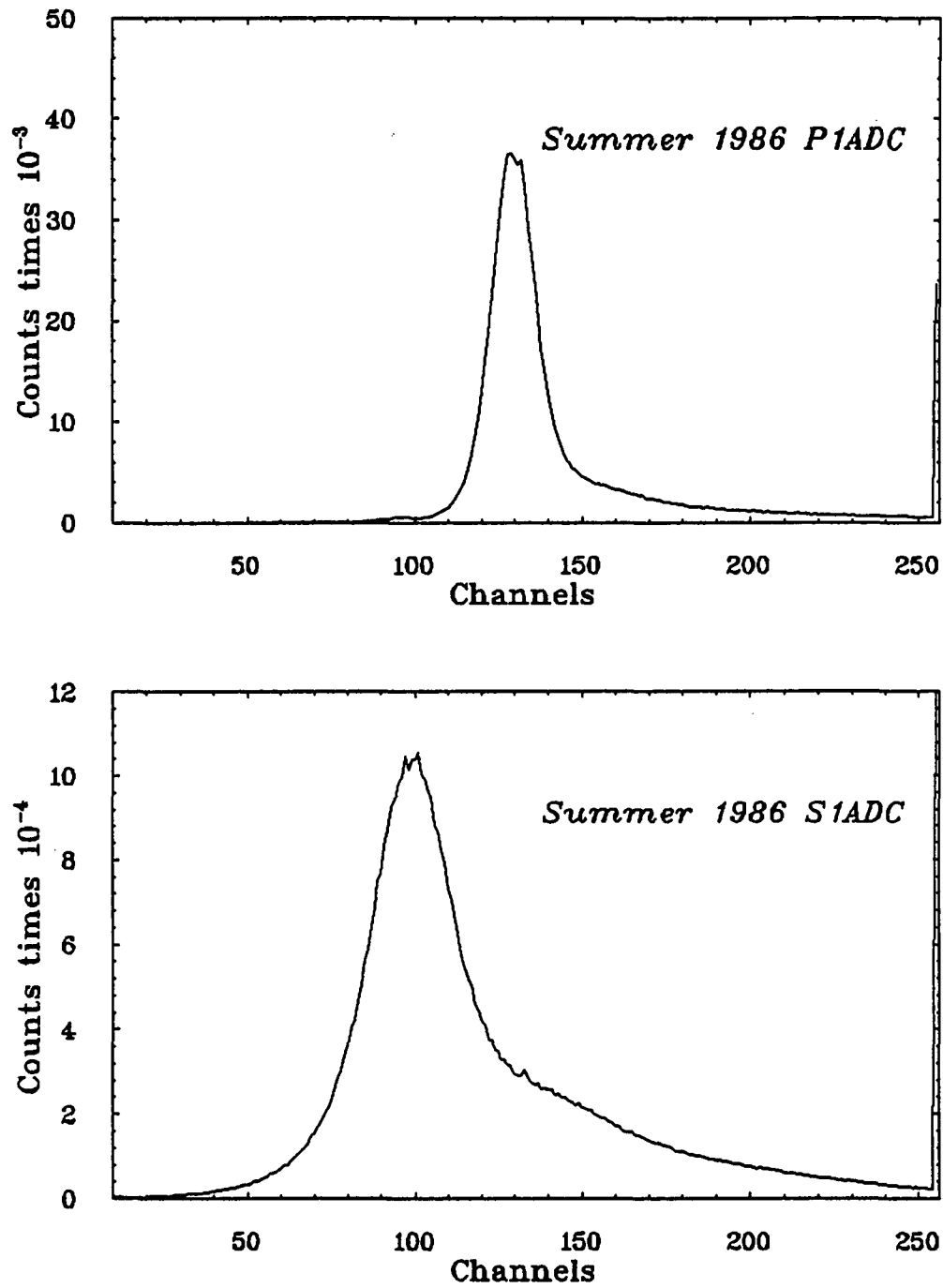


Figure 4-6: Pulse-height spectra for a paddle and for S1.

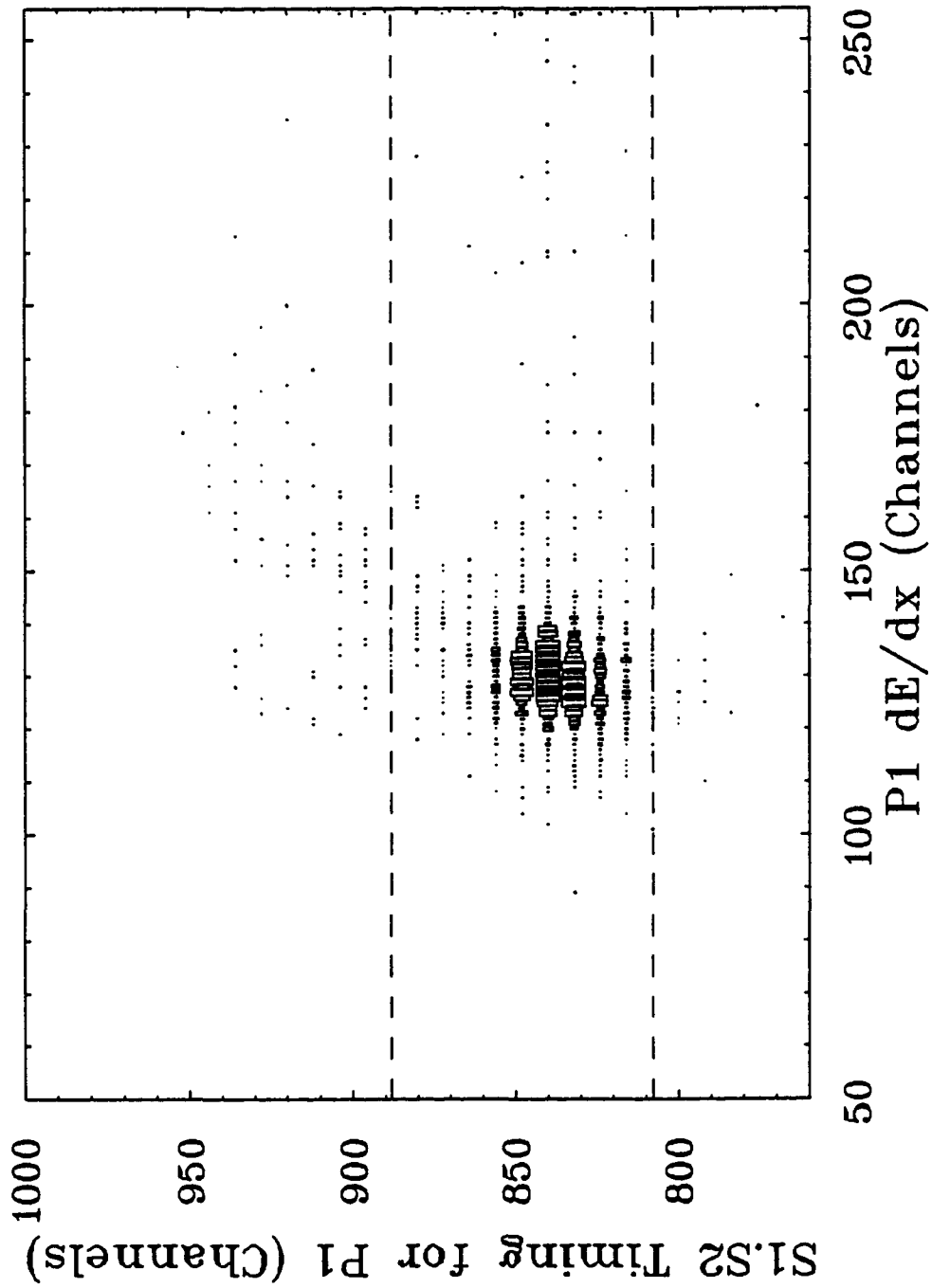


Figure 4-7: Scatter plot of pulse-height ( $dE/dx$ ) in one paddle vs . S1-S2 timing for that paddle.

the benefit of ADC cuts thus draws our attention to the events within the timing cuts and to the right of the large spot that includes the main concentration of events. It is believed that these events with a higher  $dE/dx$  are the result of nuclear reactions in the scintillators. Using the total reaction cross section of 0.34 barns for carbon it was estimated that around 2% of the events might be expected to react in the scintillators. This figure compared reasonably well with the figure for the proportion that the events to the right of the main concentration and within the timing cuts were of the total events within the timing cuts, which was 3.3% on the average. Since for our purposes events where the scattered proton underwent nuclear reactions in the scintillators were still good events, it was decided not to employ a  $dE/dx$  cut on the data.

#### 4.2.3.5 BGO Timing

A typical BGO timing curve relative to S1 is shown in Figure 4-8, with the cuts used indicated (both on-time and off-time cuts are shown). The flat background under the central peak represents random coincidences between S1 firing and the BGO firing, and the central peak represents correlated events. The background level of randoms became worse for higher beam current and so beam current was kept low, below about 6 pA. As in the case of S2 timing a study was made of the BGO energy spectrum for different subdivisions of the central timing peak and the 15.11-MeV energy spectrum peak was evident throughout the timing peak. The beam microstructure was a 0.25 nsec burst every 5 nsec, which translates to every 100 TDC channels. In some BGO timing plots the microstructure of the beam was evident, as in Figure 4-9 where it is seen in the smaller peaks to the right and left of the central peak. There is evidence of non-linearity of the TDC also, in that the microstructure peaks are somewhat closer together on the right-hand side than on the left-hand side, and correspondingly the background shows a general slope upward to the right for the same reason. Figure 4-10 shows a scatter plot with BGO 1 timing plotted on the  $x$  axis versus P1 timing on the  $y$  axis for some

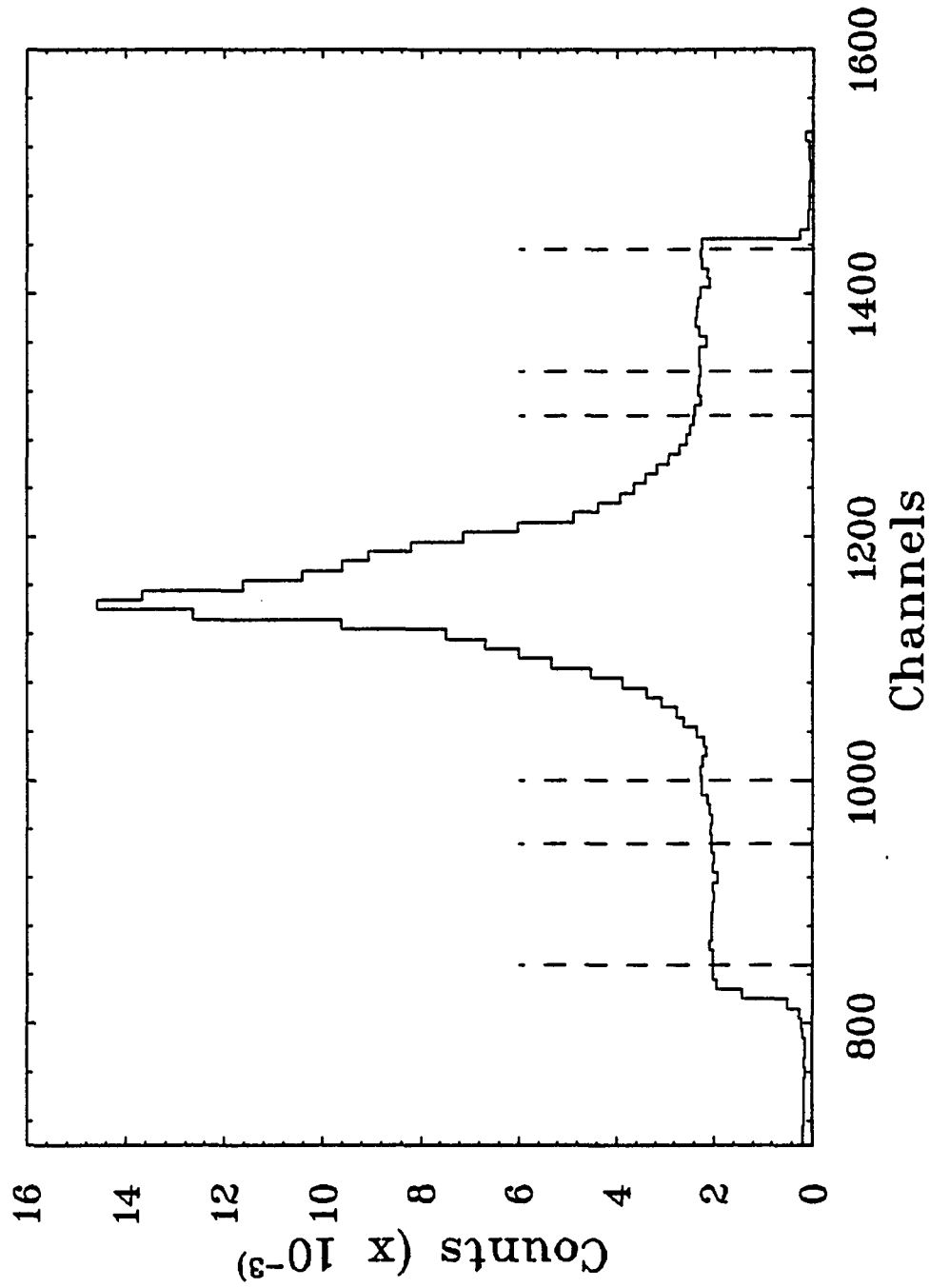


Figure 4-8: Sample BGO timing spectrum. Both on-time and off-time cuts are shown.

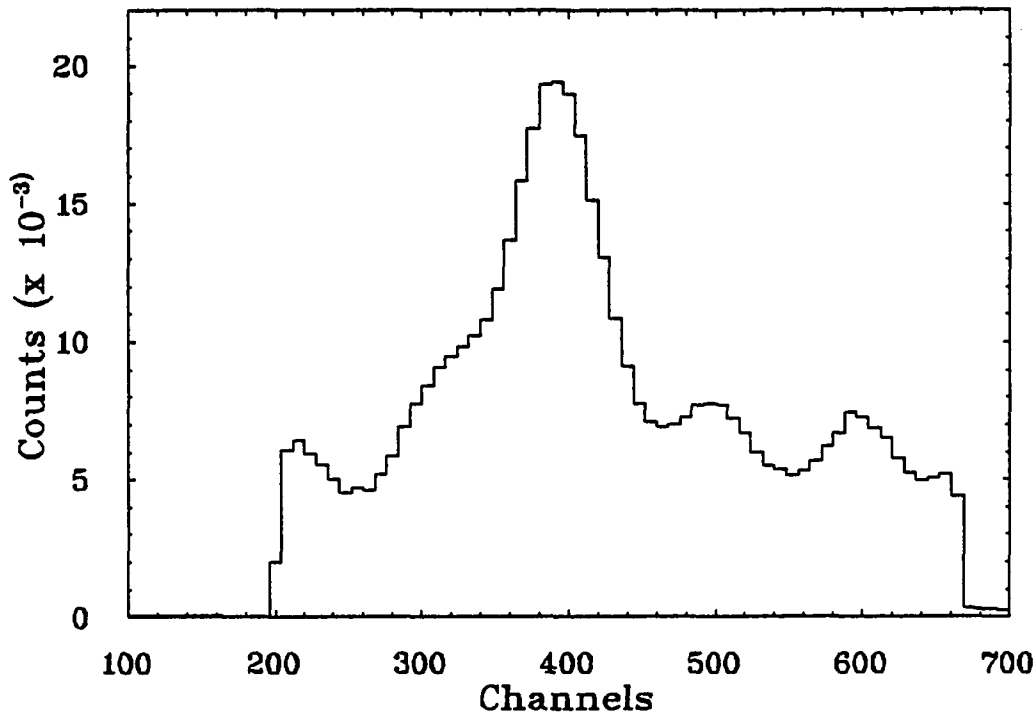


Figure 4-9: BGO timing spectrum where microstructure of the beam is evident.

fall 1985 data. The microstructure can be seen in the main horizontal band as a series of darkened areas slanting upward and to the right. Solid lines have been drawn on the plot with slope equal to one. The effect of these areas of more events can be explained merely as due to the distribution in time within the micropulse hitting the target, with the later protons causing later events in both BGO 1 and P1. (This correlation holds directly for real coincidences and on the average for random coincidences—*i.e.* although later protons in S2 from a random coincidence will not necessarily be associated with later signals in the BGO, they will have a distribution of times that is centered later than for protons from earlier parts of the micropulse.) The tail of real events that rises from the middle of the central horizontal band upward and to the left is probably knocked-out deuterons and  $\alpha$ 's, or protons, deuterons, and  $\alpha$ 's associated with neutrons

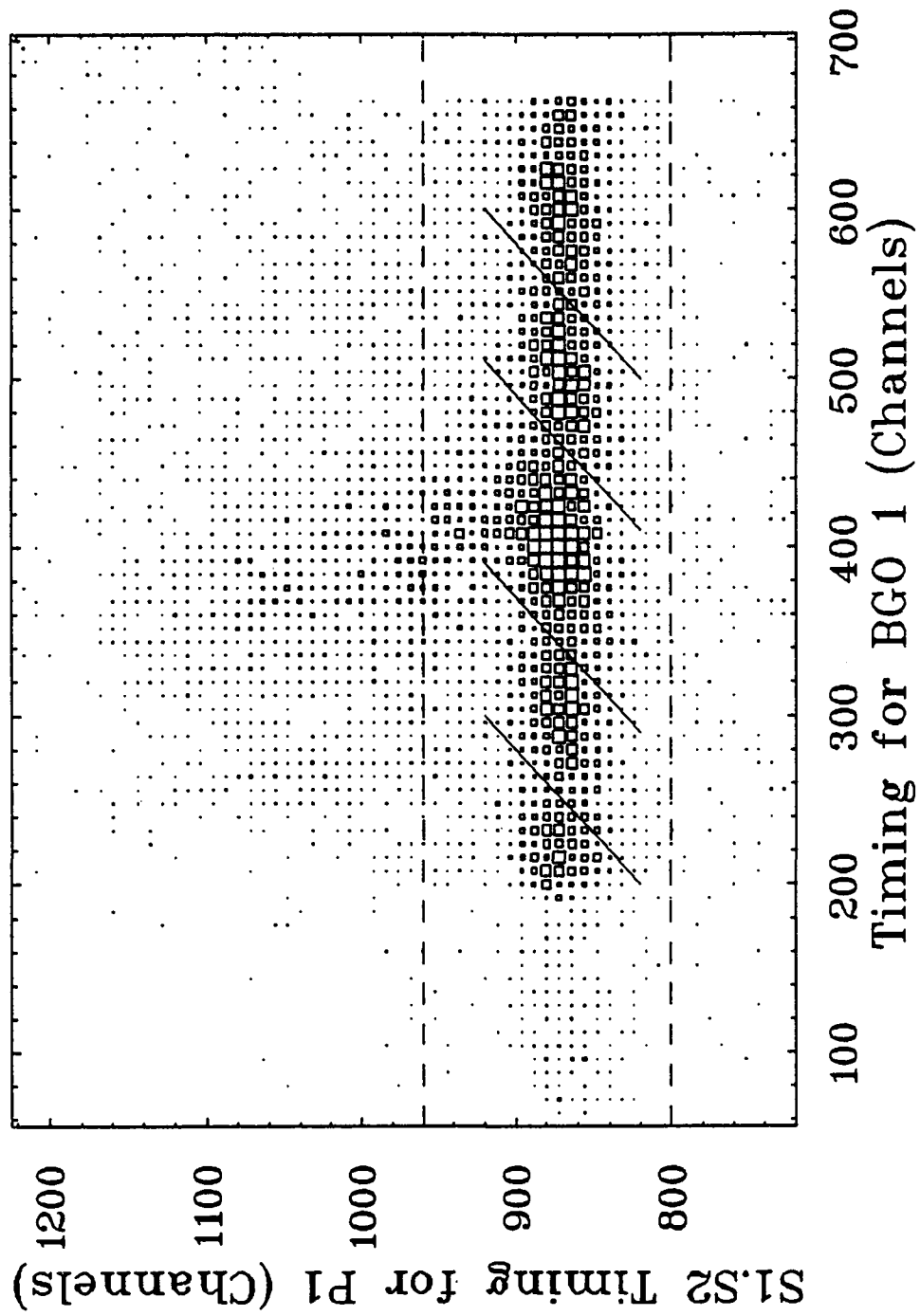


Figure 4-10: Scatter plot of S1-S2 timing on the  $y$  axis vs. BGO timing. The beam microstructure can be seen in the horizontal band.

knocked into BGO 1. This would explain the correlation of slower events (longer time relative to S1) in S2 with faster events in the BGO (shorter time relative to S1), since the available energy is shared among the particles.

BGO 3 had an anomalous hump on the left side of the main timing peak in the summer of 1986. However, this hump did not appear in the timing curve that contained only events with energy in the neighborhood of the 15.11-MeV peak, and so it was not considered a serious problem although the cause was not determined. (See Figure 4-11.) A similar hump appeared for BGO 3 in the fall of 1986, and BGO 1 had a double timing peak for that run, but these BGO's did not produce useable energy spectra for the fall of 1986 and so were not used.

#### 4.2.3.6 Pile-up

A pile-up cut was written into the software using the pile-up circuit discussed in section 3.3. However during replay it was discovered that the cut drastically cut down (by more than two thirds) the 4.44-MeV peak for BGO 3 in the fall of 1986 data. Since it was not known what the problem was, and this indicated the pile-up electronics was not working properly, at least for BGO 3, it was decided not to use the pile-up cut for the main analysis. An analysis of the amount of pile-up events was done for the normal and sideways polarization data for 1985 and this determined that within the part of the BGO energy spectrum around the 15.11-MeV peak that was eventually used to find the peak area (including the 15.11-MeV peak and some parts on the shoulders of the peak), there were 1% or less pile-up events for BGO's 2, 3 and 4, and between 1 and 2% for BGO 1. Figure 4-12 shows the energy spectrum of the pile-up events for the normal data for 1985. BGO 1, which was located in the forward direction, shows a different pattern, with more events at higher energies presumably from knocked-out neutrons.

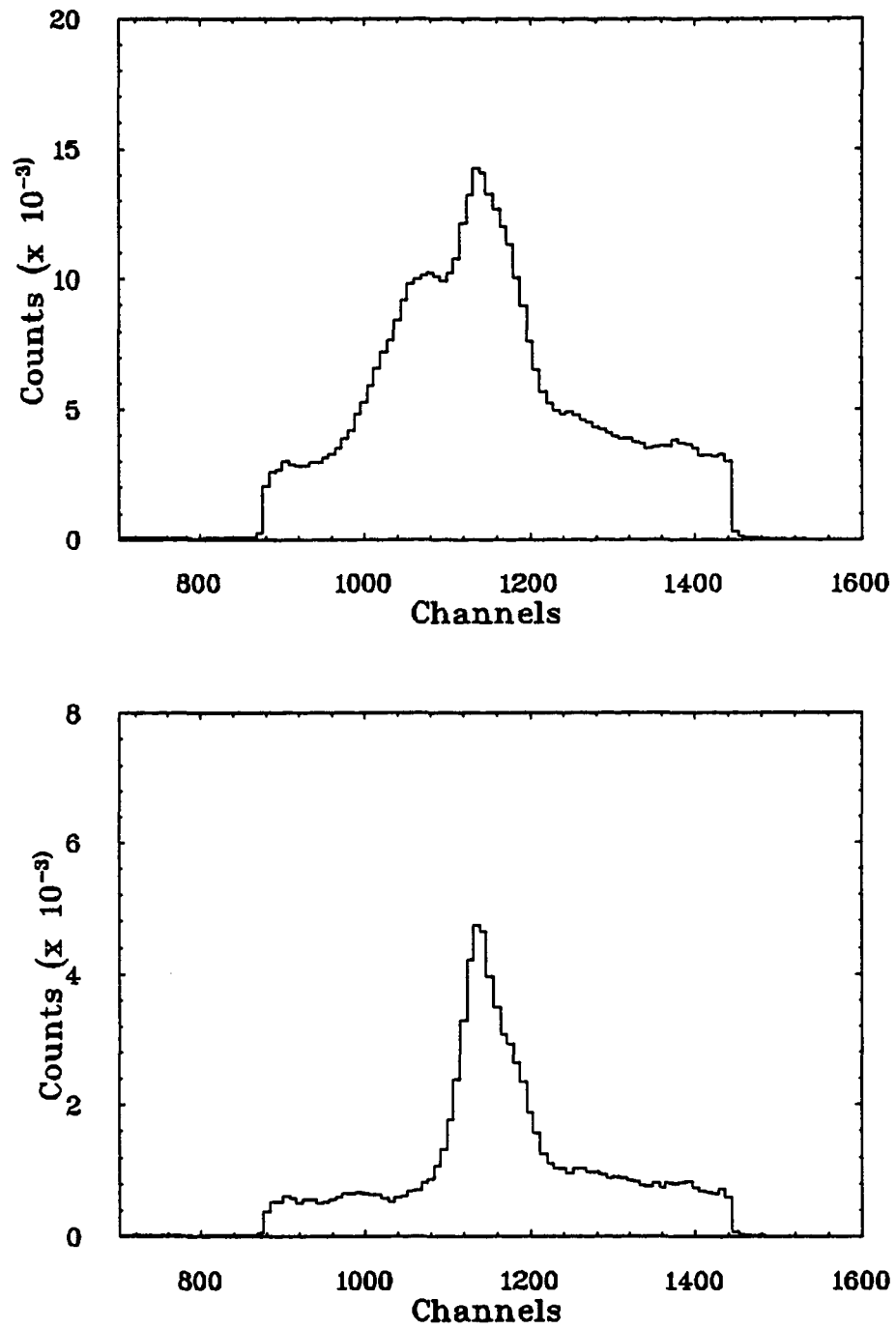


Figure 4-11: The top spectrum is the uncut BGO 3 timing in summer 1986. The bottom spectrum has had cuts made on the BGO pulse-height spectrum in the neighborhood of the 15.11-MeV peak.

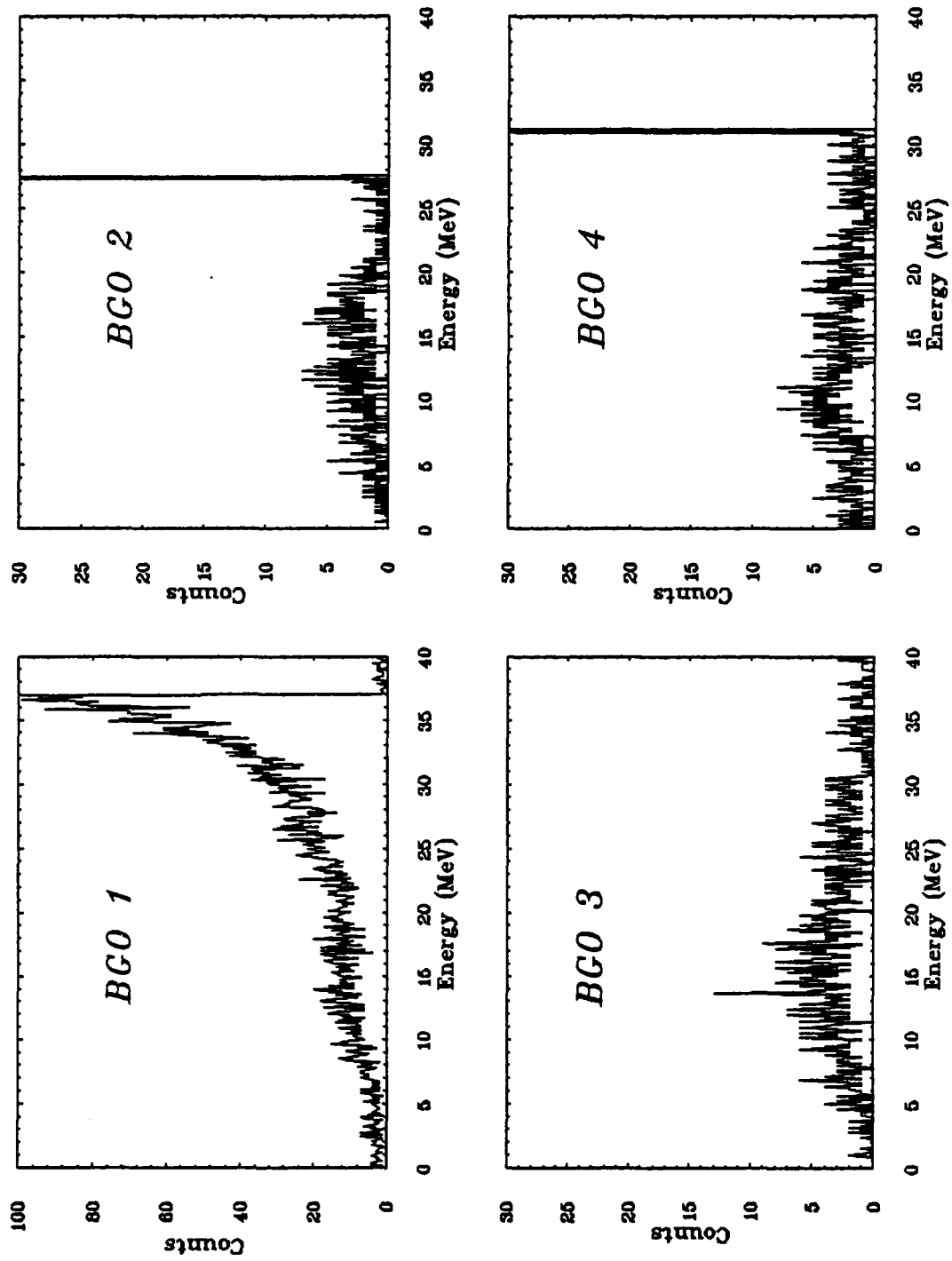


Figure 4-12: The energy spectrum of pile-up counts for the 1985 normal polarization data.

#### 4.2.3.7 Random Background Subtraction

Two kinds of background were subtracted in determining the size of the 15.11-MeV peak: correlated coincidences and non-correlated, random coincidences. The random background was subtracted by accumulating an energy spectrum with timing cuts on the flat shoulders of the BGO timing spectrum, and subtracting this energy spectrum from the energy spectrum accumulated with timing cuts on the central peak of the BGO timing spectrum (see Figure 4-13). Since off-time cuts on the BGO timing peak had different widths than the on-time cuts, the subtracted spectrum was multiplied by a normalizing constant before subtraction. In determining the widths of both the off-time and on-time timing cuts, consideration was given to the microstructure of the beam. This microstructure has a nominal period of 5 nsec, and can sometimes be seen as bumps on the top of the shoulders of the timing curve (see Figure 4-9). Since the randoms make-up of different parts of a period of the beam microstructure might well be different, it was desirable to make both the on-time and off-time cuts in widths that represented an integral number of microstructure periods. The width of the on-time cut was made to be for the duration of three micropulses. With the fall 1985 data, off-time cuts of the length of one beam micropulse were taken on one side of the timing peak only, as the widths of the flat portions on the sides of the on-time peak, controlled by the widths and delays of the outputs of the main BGO coincidence units, were only sufficient for cuts on one side. The off-time cuts for BGO 1 and 2 were made on the high or right-hand side of the central peak, and those for BGO's 3 and 4 were made on the lower or left-hand side. The widths of the cuts for the 1985 data were determined after an analysis of the positions of the microstructure peaks gave an approximate linear relationship for variation of the calibration constant of the TDC (channels/nanosecond) with channel number.

For both the summer and fall of 1986 the same procedure was not followed. The

main peaks in the timing curves were more centered and this allowed the off-time cuts to be made on each side of the main peak, one micropulse width on each side, with the result that the 1986 data had better determination of the random background than the 1985 data. The on-time cut was again 3 micropulses wide. The spacing of the micropulse peaks could not be determined as well for the 1986 data since in general only one small peak from the micropulses appeared on each side of the main on-time peak, in contrast to the situation for the 1985 data where two appeared on one side or other of the peak. Accordingly the nominal timing calibration was used throughout the timing spectrum in assigning a width of 100 channels to each micropulse in choosing the cuts.

A sample on-time BGO energy spectrum for BGO 2 from summer 1986 is shown in Figure 4-13a, with the off-time spectrum in Figure 4-13b, using the timing cuts shown in Figure 4-8. Each of these spectra is actually a composite spectrum, because of the 1/10 circuit discussed in section 3.3, so that the lower end of the spectrum has been prescaled by 0.1. The point where the transition is made can be seen at approximately 6 MeV. The subtracted spectrum which is the on-time spectrum minus 1.5 times the off-time spectrum (because of the 3:2 ratio of on-time to off-time cut widths) is shown in Figure 4-13c. For the fall of 1985, on-time, off-time, timing and resultant spectra (on-time minus three times the off-time, corresponding to the 3:1 ratio in cut widths) are shown for BGO 3 in Figure 4-14.<sup>2</sup>

#### 4.2.3.8 Background Identification

In order to handle the on-time correlated background in the best manner, substantial effort was made to identify the make-up of this background. The possibility that we could be seeing decays of other excited levels of  $^{12}\text{C}$  was investigated. Inelastic proton

---

<sup>2</sup>The off-time spectrum generally appeared smooth and showed no evidence of a 15.11-MeV peak for nearly all the data. In one exception in the fall of 1986, BGO 2 showed a large peak near 15.11 MeV for some early tapes that were not included in the final results. We were not able to determine the cause of this difference from the rest of the data.

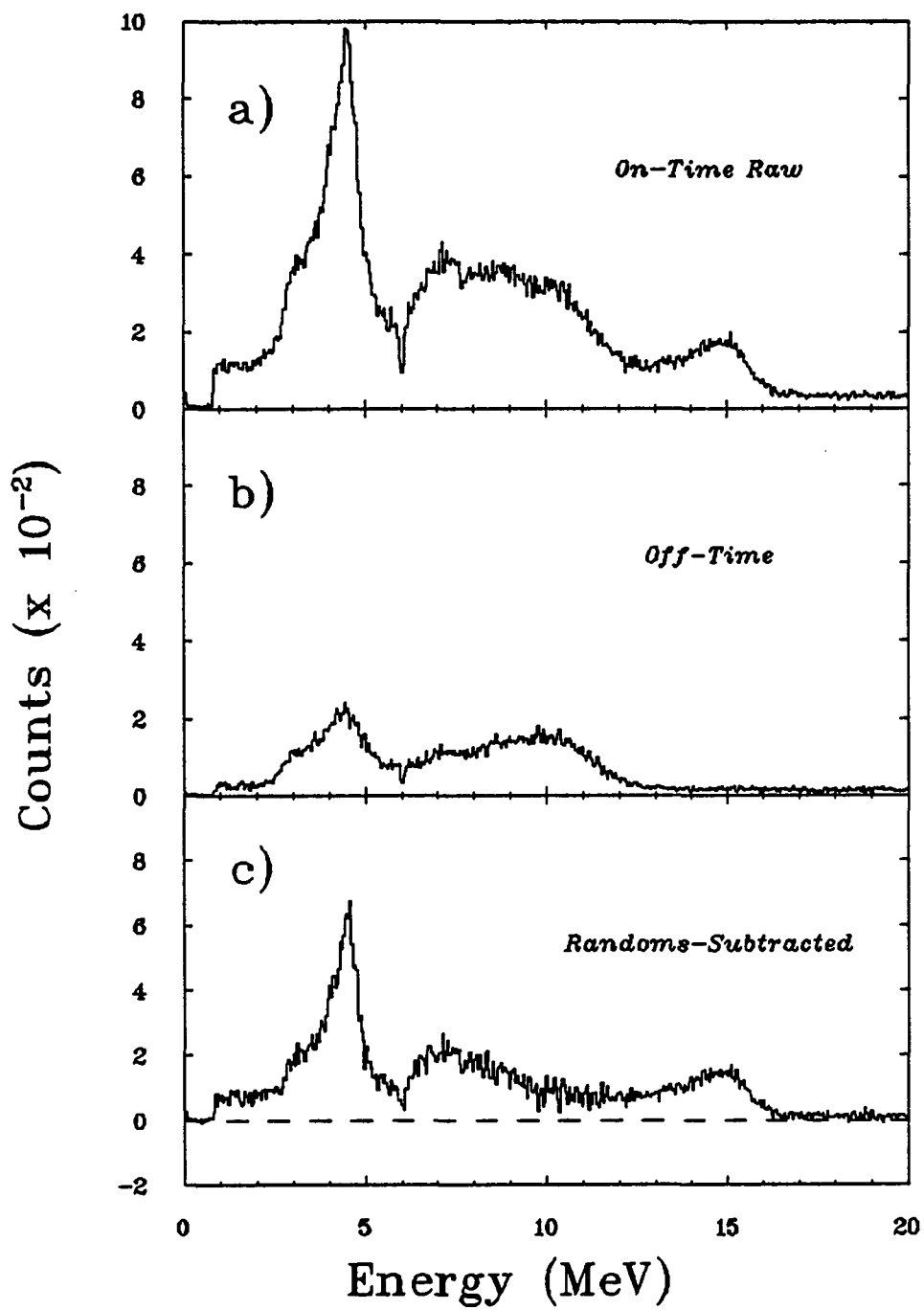


Figure 4-13: Longitudinal polarization on-time raw, off-time and randoms-subtracted spectra for BGO 2.

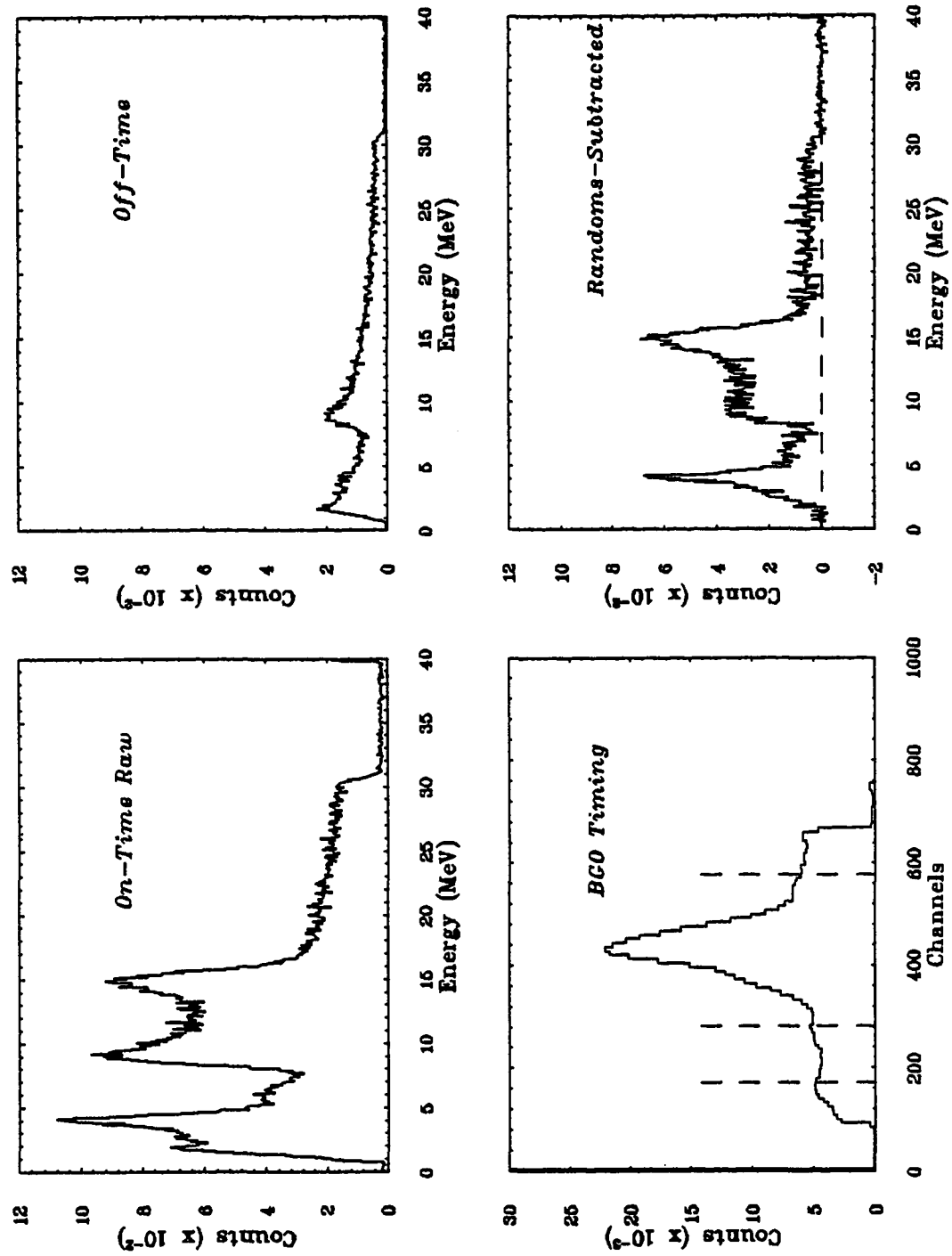


Figure 4-14: Same as Figures 4-13 and 4-8 for BGO 3 sideways polarization.

scattering data for 200 MeV [CMF\*82] shows that there are levels excited at 12.71 MeV, 16.58 MeV, 18.4 MeV, 19.2 MeV and 19.7 MeV with cross sections comparable in magnitude to the 15.11-MeV state. The 12.71 MeV state has a  $\gamma$  branching ratio of about 2% to the ground state. The other states all have radiative branching ratios of much less than 1%, decaying mainly by  $\alpha$  or proton emission [Ajz85]. (The 15.11-MeV state doesn't  $\alpha$ -decay because it is  $T = 1$  and it cannot couple to the two daughter states of  ${}^8\text{Be}$  and  ${}^4\text{He}$  whose isospin are both  $T = 0$ .) Thus as far as we can ascertain, contamination of the 15.11-MeV transition from the decay of other excited states of  ${}^{12}\text{C}$  is not a problem.

The incident proton energy in our experiment is slightly above the pion production threshold (280 MeV), and consequently there is the possibility of  $\gamma$ 's from the decay of  $\pi_0$ 's contributing to the background. Based on an estimate derived from the free nucleon-nucleon production cross section, the total  $\pi_0$  production cross section for  ${}^{12}\text{C}$  at our energy (318 MeV) is approximately  $80 \mu\text{b}$ , which is two orders of magnitude less than the 15.11-MeV  $\gamma$  cross section.<sup>3</sup> (Fermi motion in the  ${}^{12}\text{C}$  nucleus may result in a  $\pi_0$  production cross section significantly higher than  $80 \mu\text{b}$ — for 200 MeV/c Fermi momentum in a direction antiparallel to the beam direction the cross section is roughly a hundred times the cross section for no Fermi motion. However Fermi motion in other directions will lower this factor.) A Monte Carlo simulation was done using EGS4 [NHR85] of the response of a BGO detector of our dimensions to monoenergetic  $\gamma$ 's of energy equal to half the mass of a  $\pi_0$ , and this is shown in Figure 4-15. In the region around 15–20 MeV the spectrum is fairly flat and therefore might account for the flat background that is seen to the right of the 15.11-MeV peak. A more refined simulation was done, using a 3-body kinematics program written by the author, of the reaction

<sup>3</sup>Originally an upper limit for the  $\pi_0$  cross section was used that was 100 times too large, and led to a more involved effort at investigating the possibility of  $\pi_0$ 's being responsible for the background than was actually warranted, since with the erroneous cross section the estimates of the expected background levels were comparable to the 15.11-MeV peak levels.

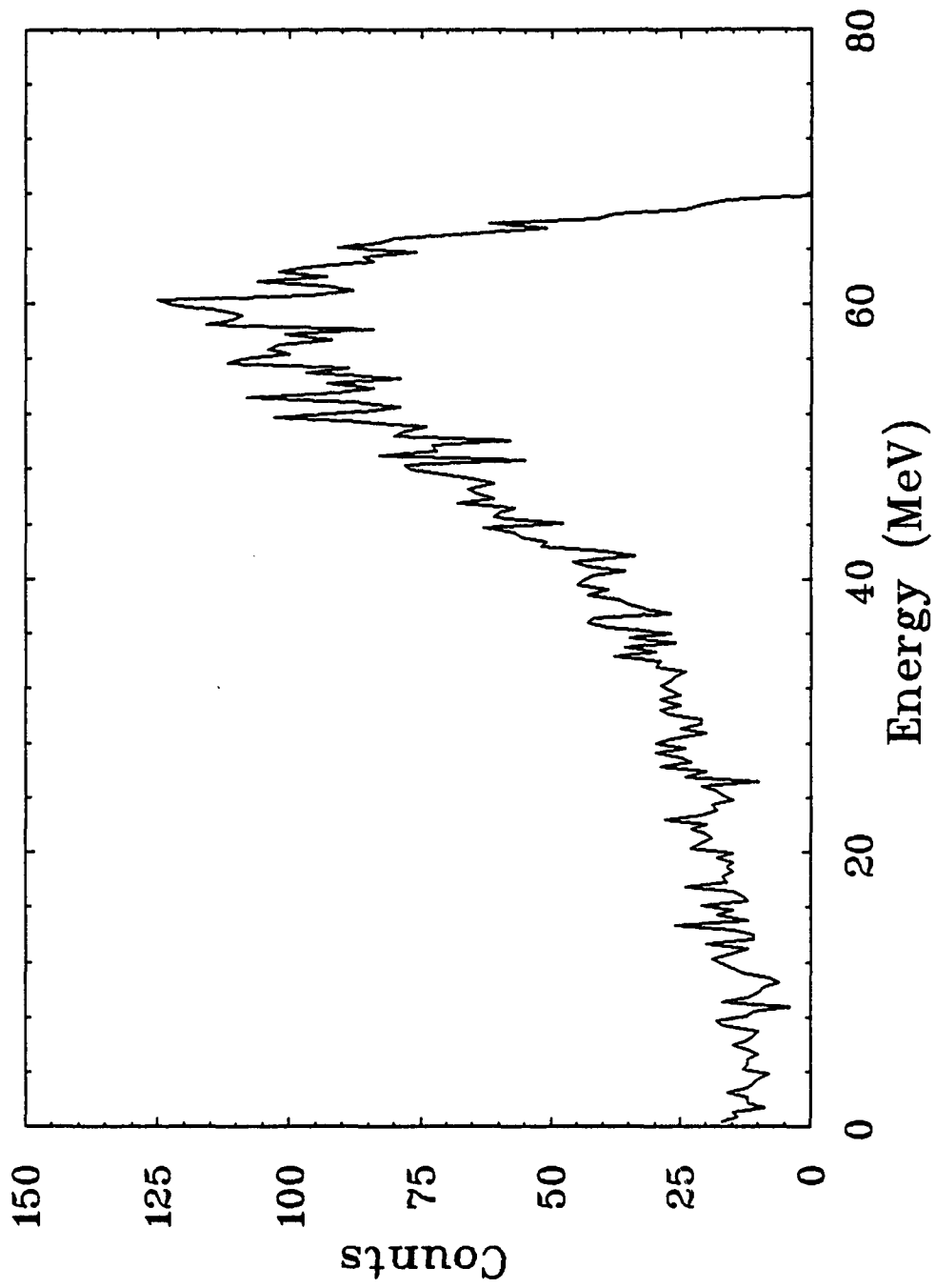


Figure 4-15: EGS4 spectrum of 68.74 MeV  $\gamma$ 's in BGO (one-half the  $\pi_0$  mass).

$p + p \rightarrow p + p + \pi_0$  as follows: the recoil angle and energy of the proton was fixed to be within the range of S2 angles and timing cuts, the CM energy of the  $\pi_0$  was picked uniformly within the kinematically allowed limits, and the  $\pi_0$  was allowed to decay into  $\gamma$ 's back-to-back isotropically in the  $\pi_0$  rest frame. Then it was determined whether and with what energy the  $\gamma$ 's went into the BGO detectors. Since the  $\pi_0$  is spin 0 and is produced near threshold (S wave) we expect the pion to be produced isotropically; it should appear with equal probability in the allowed phase space, as reflected in the calculation. The results for the most forward and most backward BGO's, 1 and 4, are shown in Figure 4-16. The spectrum begins to rise quite near the 15.11-MeV region. Sample spectra for real data for BGO's 1 and 4 are also shown in Figure 4-16, and it can be seen clearly that the background does not resemble the  $\pi_0$  spectrum. The Monte Carlo program is included as Appendix B.

In addition to  $\gamma$  rays, knocked-out particles must be considered as candidates for the background. Since protons, deuterons, and  $\alpha$ 's are charged particles and would be vetoed by the anticoincidence scintillators with an expected efficiency of 98–99%, the main candidate for this type of background is knocked-out neutrons. An estimate for the neutron knock-out cross section using 6 times the (n,p) cross section for S2 angles gives a cross section of 36 mb/sr, which is 36 times the 15.11-MeV cross section for those angles. In the approximation that the neutron is at rest, equal in mass to the proton, and unaffected by the rest of the carbon nucleus ( $^{11}\text{C}$ ), the neutron will come off from the proton at an angle of  $90^\circ$ , and so for example neutrons ending up in BGO 1 at  $\theta_\gamma = 69^\circ \pm 10.6^\circ$  will be associated with protons scattered to the left between the angles of  $\theta_p = 10.4^\circ$  and  $31.6^\circ$ , and so higher background levels should be seen for BGO 1 spectra for protons scattered to the left than for protons scattered to the right. For BGO 3 in the same approximation, neutrons entering it at  $\theta_\gamma = 89^\circ \pm 10.6^\circ$  to the left will be associated with protons scattered between  $0^\circ$  and  $11.6^\circ$  to the right. In the

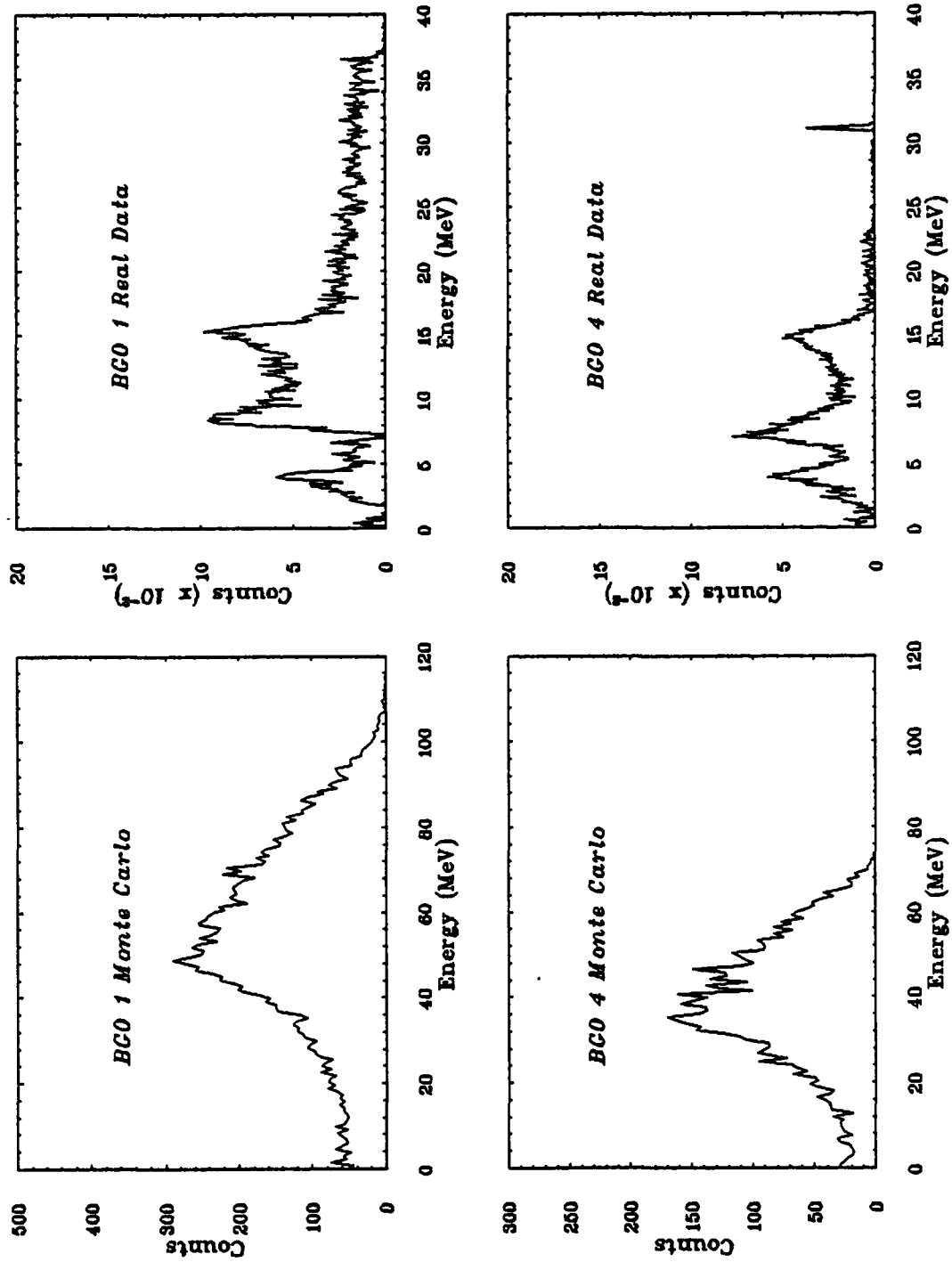


Figure 4-16: Comparison of expected background from  $\pi_0$  decay and real data for the most forward BGO (BGO 1) and the most backward one (BGO 4).

same approximation there will be no neutron background in BGO's 2 and 4 because backscattering is not kinematically allowed. Figure 4-17a shows two overlaid spectra for BGO 1 from fall of 1985 sideways polarization, one associated with protons detected in S2 to the left (S2 elements 3-5, see Figure 3-4) and the other with protons scattered to the right (elements 11-13 in Figure 3-4). The spectrum for scattering to the left shows more counts than the one for scattering to the right, particularly in the area around 12 MeV. Figure 4-17c shows the same two types of spectra for BGO 3 (fall 1985, sideways polarization) and now the situation is reversed and the spectrum for scattering to the right is higher than the spectrum for scattering to the left. Figures 4-17b and 4-17d show BGO's 2 and 4 with right and left overlaid and there is no noticeable effect. This is just what one would expect for knocked-out neutrons as outlined above.

To have a better idea of what might be expected to occur when we depart from the simplifications mentioned above, a Monte Carlo calculation was done for the reaction  $p + {}^{12}\text{C} \rightarrow {}^{11}\text{C} + p + n$  which included assigning a Fermi momentum to the struck neutron in the  ${}^{12}\text{C}$  using a Fermi gas model [FH74]. This Fermi momentum was assigned to the  ${}^{11}\text{C}$  nucleus (treated as a spectator) and the rest of the available energy in the center of mass frame was shared between the  $p$  and the  $n$ , assigning the neutron energy with a uniform distribution between the kinematically allowed limits [Per82b]. A weighting was then given to the events using the free  $(p, n)$  cross section [LM70] and it was then determined which events had neutrons entering the BGO for which the calculation was run, and also protons entering S2. (The Monte Carlo did not make any allowance for the analyzing power of neutron knock-out reactions.) Scatter plots of the results of this calculation for the different BGO's showing proton  $\phi$  angle *vs.* neutron momentum and proton  $\theta$  angle *vs.* neutron momentum are given in Figures 4-18 and 4-19. The S2 acceptance angles are indicated by dashed lines in Figure 4-19. As can be seen, the Fermi momentum enables some neutrons to be scattered into every part of S2, and therefore

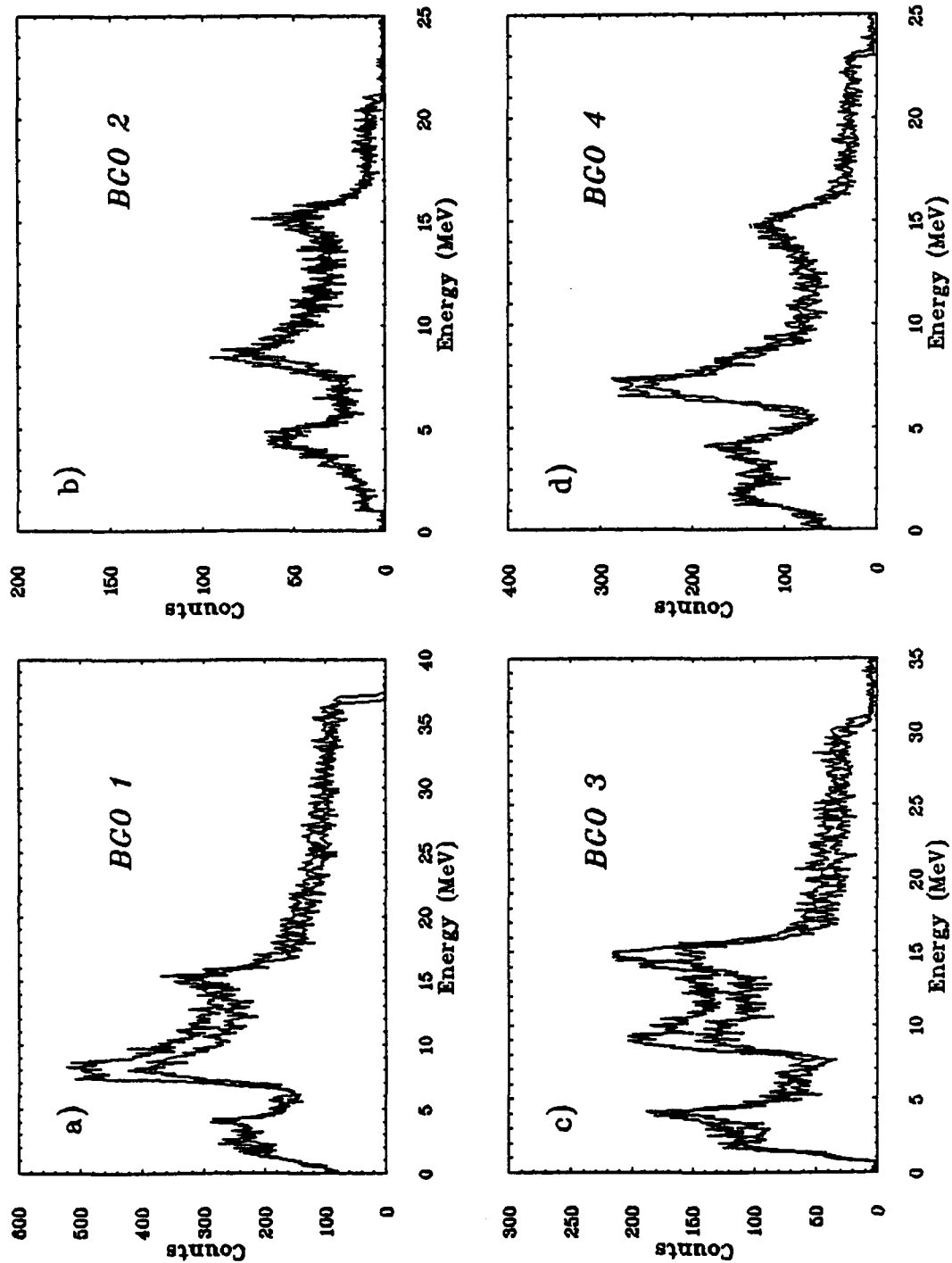


Figure 4-17: Comparisons of BGO spectra for protons scattered to the left and protons scattered to the right for the four BGO's. See the text. These are spectra before the randoms are subtracted.

the results of the calculation are consistent with the experimental data.

A study of the BGO response to neutrons by Häusser *et al.* [HLAK83] shows that with incident neutrons of from six to ten MeV there is a detection efficiency of about 30%. They also gave response spectra for four different energies of incident neutron, 4, 6, 8, and 10 MeV (see Figure 4-20). Since in our experiment we expect neutrons with a continuous range of energies between 0 and  $E_{max}$  which ranges from about 25 MeV for BGO 4 to about 85 MeV for BGO 1, we cannot predict on the basis of the available information what the neutron background should look like. However a background that decreases gradually with increasing energy, such as we observe in BGO's 1 and 3 is consistent with the available information and along with the high cross section for neutrons indicates that most of the on-time, correlated background is of this type.

#### 4.2.3.9 Use of EGS4 to Find the 15.11-MeV Peak Amplitudes

Since the background varied with the  $\phi$  direction of the scattered proton, we decided to fit the randoms-subtracted spectrum with an EGS4-determined 15.11-MeV peak shape (BGO response function). EGS4 [NHR85] is a standard simulation package for electron and  $\gamma$  showers which can be adapted to the geometry of the experiment. We fit the spectrum with an EGS4 15.11-MeV peak shape with a variable amplitude. A simple functional form— either a quadratic polynomial ( $ax^2 + bx + c$ ) or an exponential ( $ae^{-bx} + c$ ) approximated the background. The EGS4 simulation was run for the actual size of the BGO of, and with 15.11 MeV  $\gamma$ 's emanating from a point 8 inches from the center of the front face of the detector, located on the detector symmetry axis. The resulting spectrum is shown in Figure 4-21. To account for the resolution of the BGO and photomultiplier tube, mostly from statistics in photons reaching the phototube and photoelectrons in the phototube, a gaussian (whose width was determined by a fit as will be discussed below) was convoluted with the basic spectrum in Figure 4-21 with the result shown in Figure 4-22, which we will call the convoluted EGS4 form. As a check on

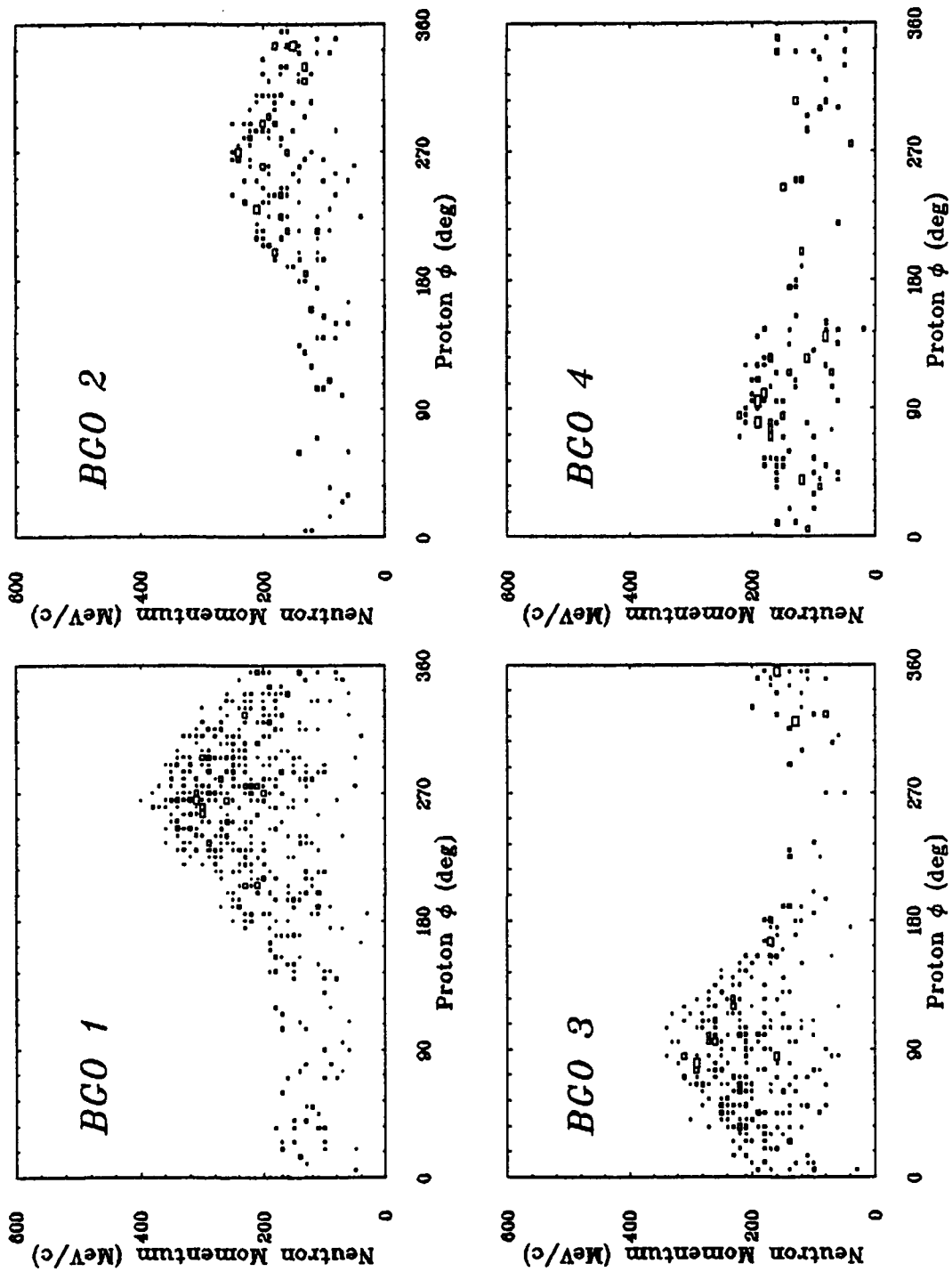


Figure 4-18: Results of a Monte Carlo calculation for neutron knockout on  $^{12}\text{C}$  (including Fermi momentum) showing neutron momentum *vs.* outgoing proton  $\phi$  angle. See text.

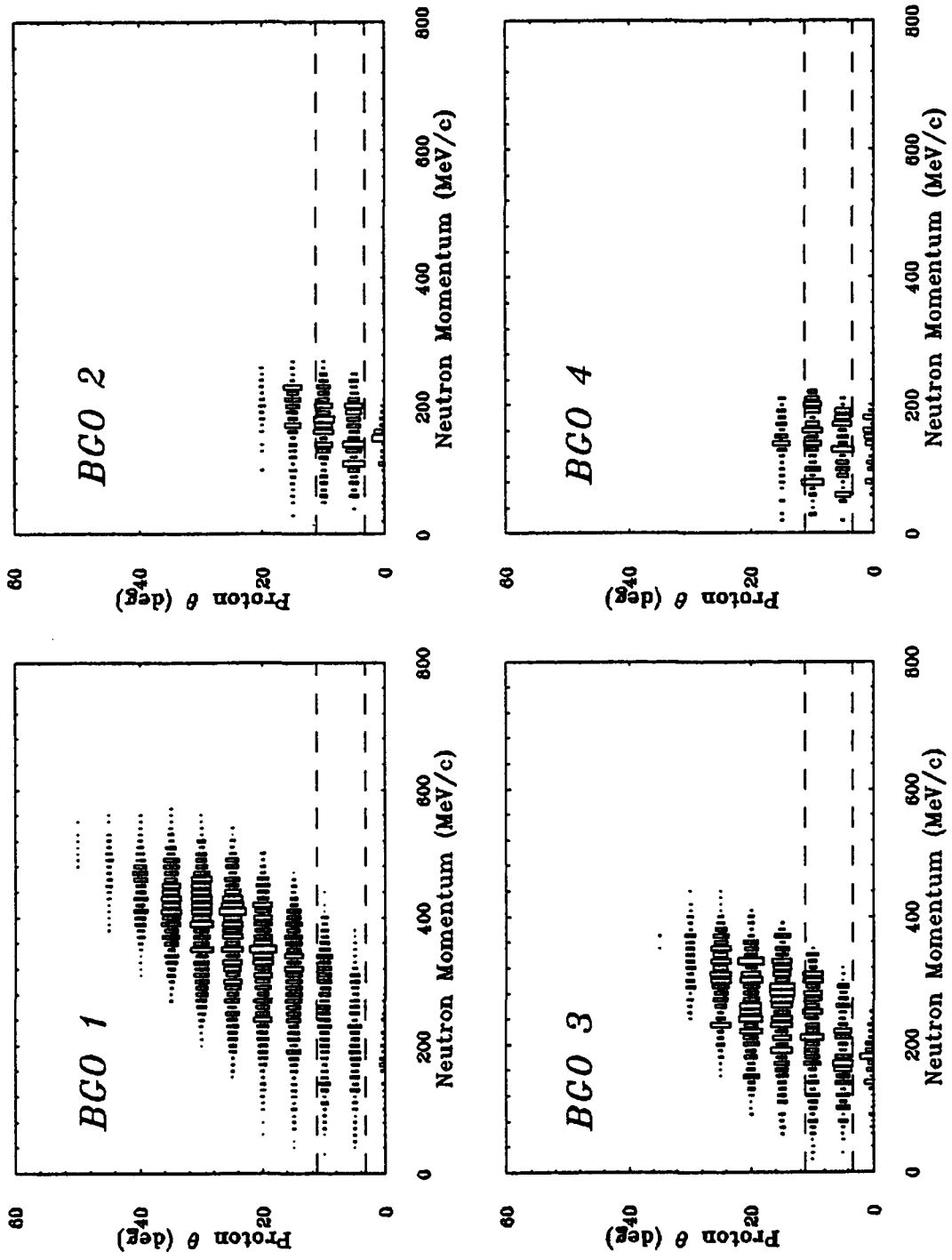


Figure 4-19: Same as Figure 4-18 but now vs. outgoing proton  $\theta$  angle. S2 acceptance angles are indicated by dashed lines. See text.

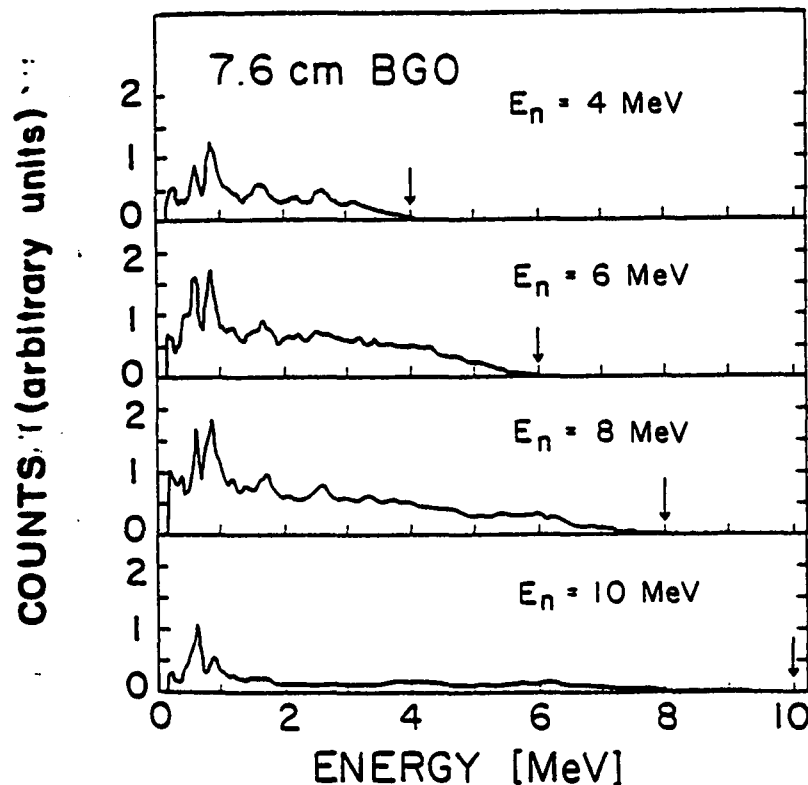


Figure 4-20: BGO response to neutrons of the energies indicated from Ref. [HLAK83].

the method, an EGS4-generated spectrum of 4.44 MeV  $\gamma$ 's in BGO, convoluted with a gaussian whose width was allowed to vary, on top of an exponential background function ( $ae^{-bx} + c$ ) was fit to a sample of calibration data. (Fitting with the convoluted EGS4 form involved using a table look-up and interpolation procedure.) In addition to the width, an overall amplitude and the exponential background parameters were allowed to vary. The resulting very good fit to the calibration data is shown in Figure 4-23. The smaller peak to the left of the main photopeak is the first escape peak (where one 0.511-MeV  $\gamma$  from the annihilation of a positron from pair production escapes detection). The second escape peak (where both  $\gamma$ 's escape), 0.511 MeV to the left of the first escape peak is also visible in the calibration data, although not in the EGS4 curve. From the width of the convolution gaussian the resolution of the BGO and phototube ( $\Delta E/E$

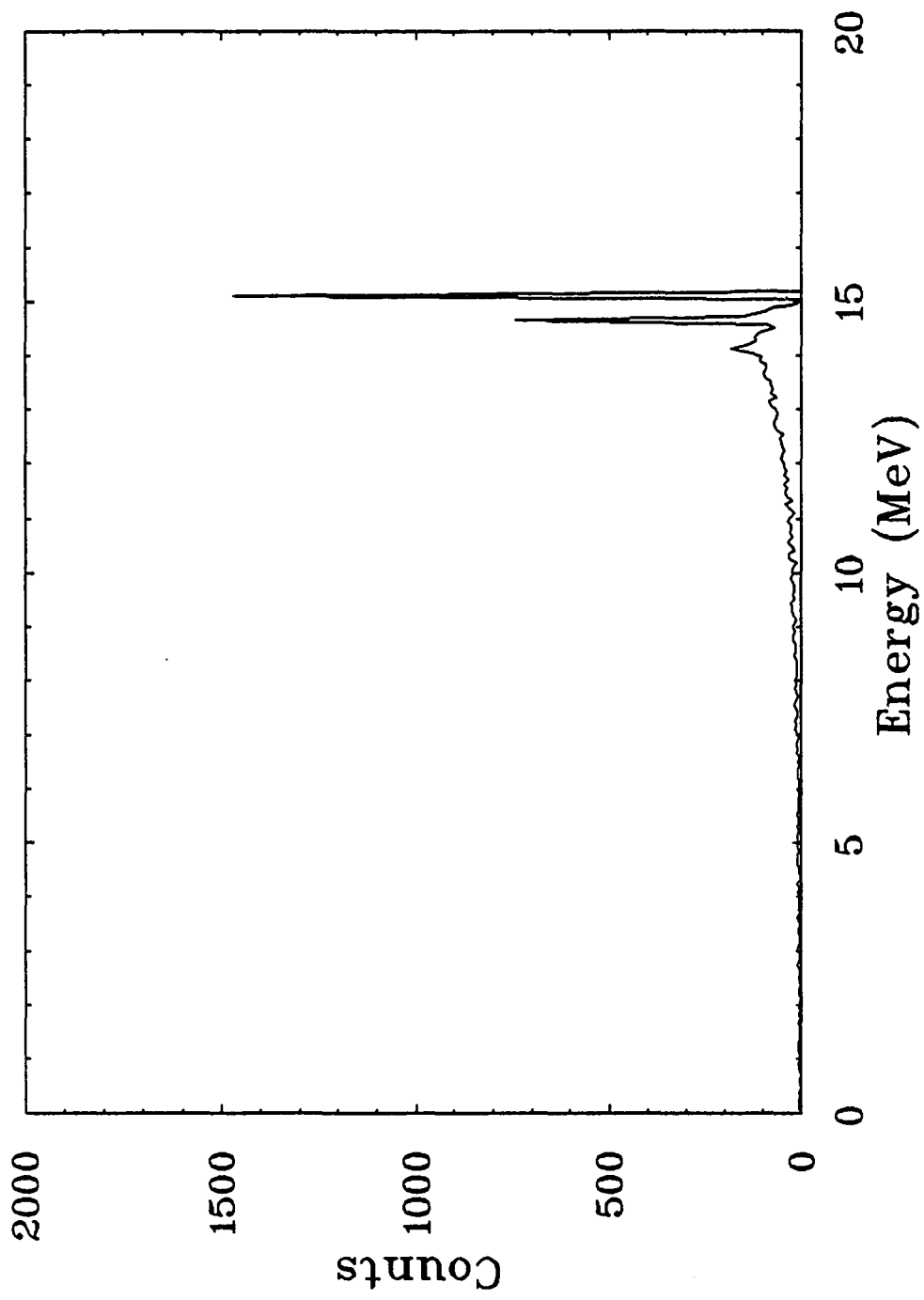


Figure 4-21: Basic 15.11-MeV spectrum in BGO from EGS4.

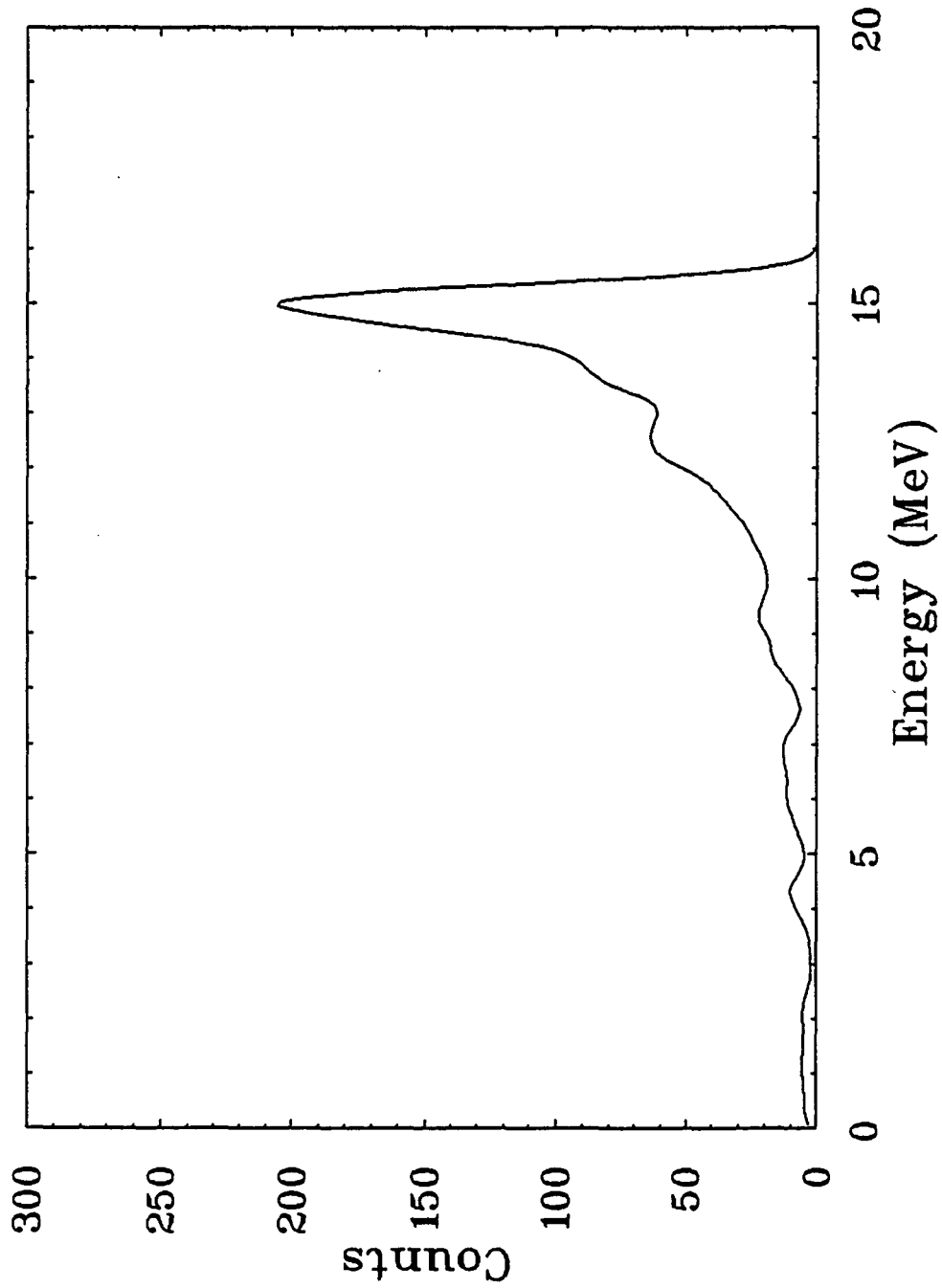


Figure 4-22: Example of result of convoluting the basic EGS4 15.11MeV spectrum with a gaussian to represent resolution.

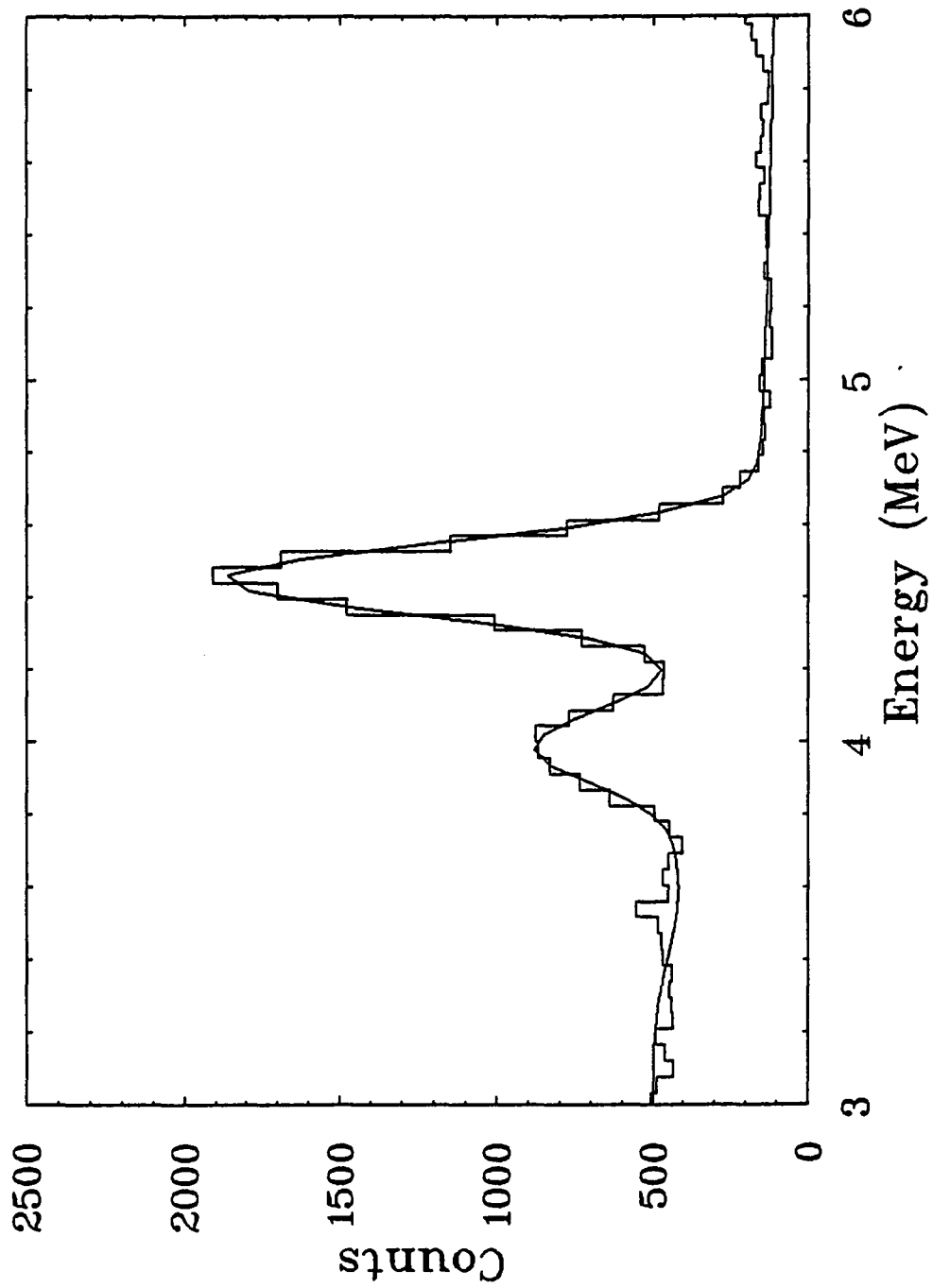


Figure 4-23: Fit of the basic 4.44-MeV EGS4 spectrum convoluted with a gaussian to some 4.44-MeV source calibration data.

where  $\Delta E$  is the FWHM) is 5.46% which when adjusted to the standard 0.662 MeV Cs transition ( $\times\sqrt{4.44/0.662}$ ) yields 14.15% resolution, which is considered very good.

To determine which type of functional form (quadratic or exponential) should be used for the background, the convoluted EGS4 form was subtracted from different samples of data with the width and amplitude adjusted to produce the smoothest resulting spectrum by eye, and then this spectrum was fit with either a quadratic polynomial or exponential form. The exponential form generally produced a smaller  $\chi^2$  than the polynomial and so it was chosen to represent the on-time correlated background. In theory we should have been able to use the calibration data to find the correct width for the convoluting gaussian by scaling up by a factor of  $\sqrt{15.11/4.44}$  from the calibration widths. However, since the (residual uncorrected) temperature shifting had introduced an additional spread in the data, the width for the gaussian and the peak centroid position were determined by a fit to each run of data. For a better fit in determining these two characteristics, data from both normal and reverse polarization and for all directions of the scattered proton were combined. Thus for each run, a 6-parameter fit was done on the combined data: 3 parameters for the background exponential, a width for the convoluting gaussian, a centroid position, and an overall amplitude. This determined the width and centroid for the convoluted EGS4 form. Once the centroid position and width were determined, a 4-parameter fit was done on data for each  $\phi_p$  direction with the combined normal and reverse polarization data: 3 exponential background parameters and an amplitude. Finally a 2-parameter fit was made on data from each direction of polarization (normal and reverse) with one peak amplitude and one background amplitude. The amplitudes from these final fits were used to compute the asymmetries. A sample of data and a 6-parameter fit of BGO 2 from fall 1986 is shown in Figure 4-24a, and a 4-parameter fit for normal polarization scattering to the right is shown in Figure 4-24b. Figure 4-25 shows the final 2-parameter fit corresponding to

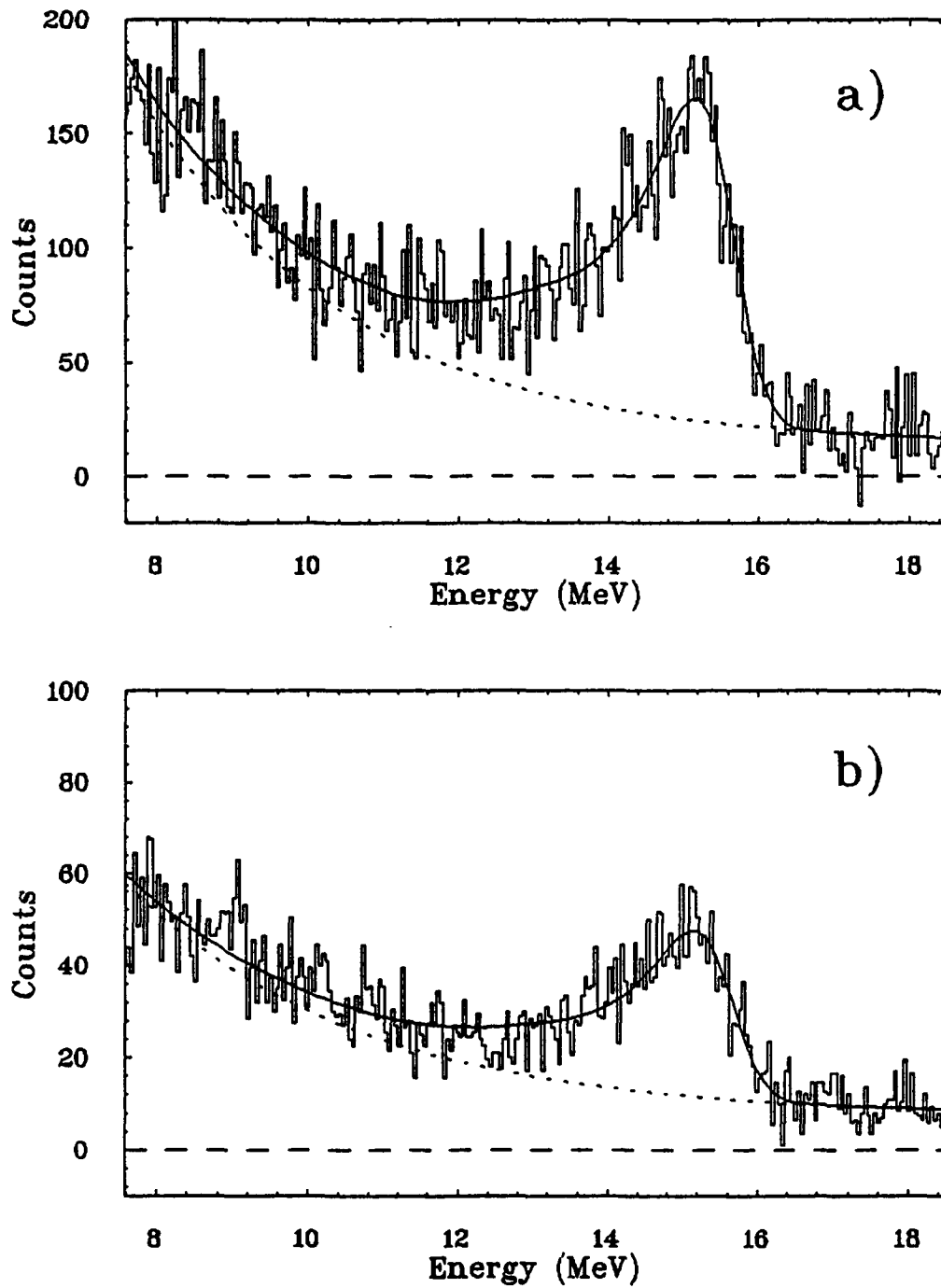


Figure 4-24: The top spectrum and fit is for 1986 BGO 2 of all azimuthal proton directions and both polarizations to get the gaussian width and centroid position, and the lower spectrum is a for a single azimuthal direction and polarization. The on-time background is shown as a dotted line. See the text.

Figure 4-24.

#### 4.2.4 Uncertainty Analysis

The statistical uncertainty in each channel of the raw spectrum is equal to the square root of the channel contents, since this quantity follows the Poisson distribution. Our randoms-subtracted spectra, however, have larger uncertainties because they are the result of combining two spectra: the on-time and off-time spectra, and the correctly propagated statistical error for each channel is  $\sigma = \sqrt{\sigma_{\text{On}}^2 + w^2\sigma_{\text{Off}}^2}$ , where  $w$  is a weighting factor and equal to the ratio of the on-time to off-time timing window widths. The randoms-subtracted spectrum with these adjusted errors was fit with the convoluted EGS4 form by the CERN fitting program HFIT, which inverts the 2nd derivative or Hessian matrix to find the uncertainties in each fitting parameter (a good discussion of this method may be found in Ref. [PFTV86]). The standard deviations of the amplitudes given by the CERN routine were propagated with the error in the ratio of normal to reverse beam current to arrive at the statistical errors in the asymmetries. The uncertainty in the average incident beam polarization (of the hourly measurements provided by LAMPF) was determined to be negligible compared to the other uncertainties and so was not used in the error analysis. The uncertainties in the ratio of normal to reverse beam current were found by merely calculating the root mean square deviation from the mean of the ratios of the different scalers. The uncertainties in the beam current monitor ratios were always less than 1.8%.

Most systematic errors in determining the amplitudes will cancel since they affect both the numerator and denominator of the asymmetries. Possible sources of error in these amplitudes involve the use of a smooth background function of simple form, and the possibility that EGS4 might not accurately determine the peak shape. Also some residual broadening of the 15.11-MeV peak due to temperature effects may not be well represented by a gaussian in the various cases (since not all of this was corrected). Errors

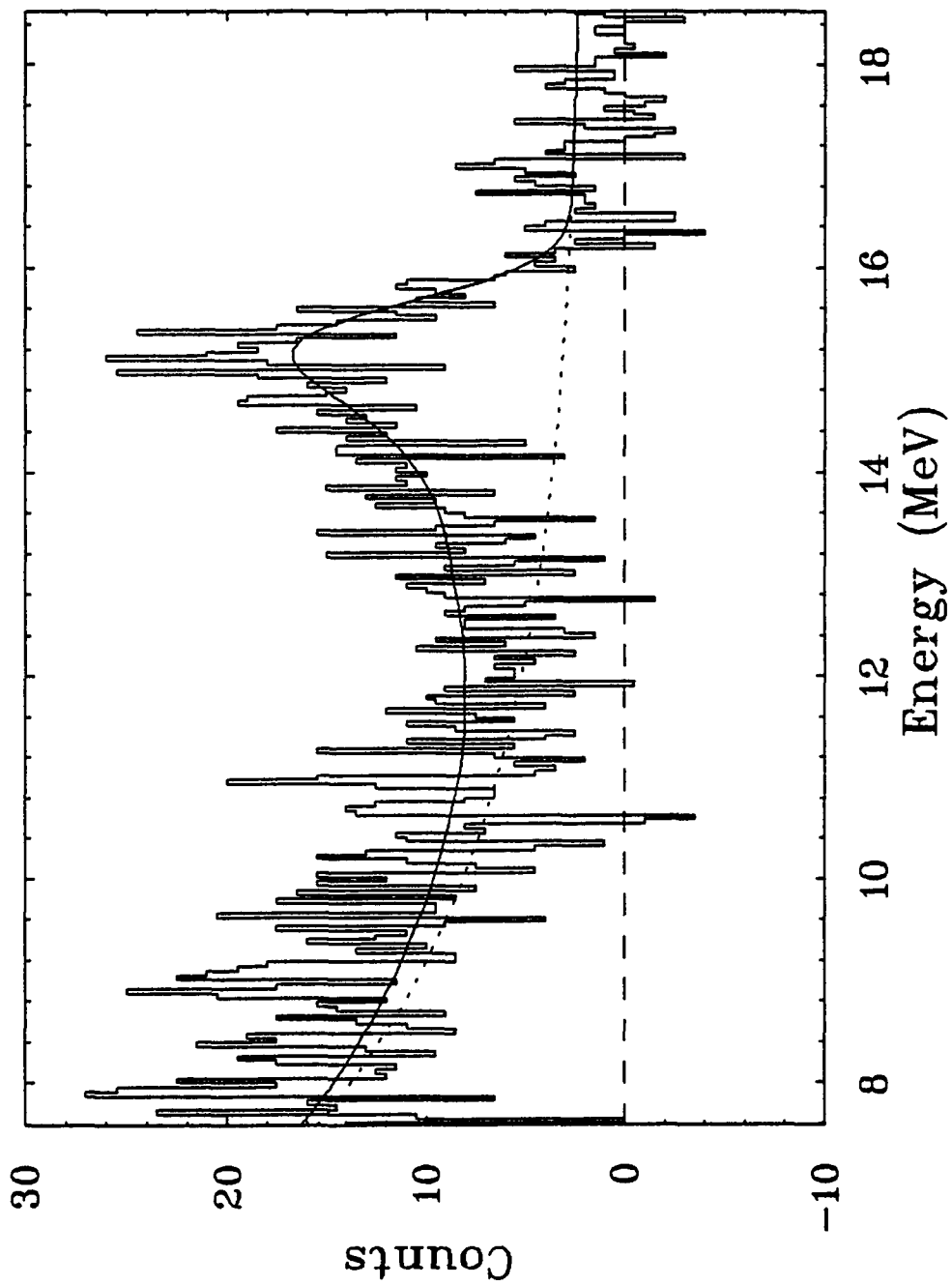


Figure 4-25: Two-parameter fit corresponding to Figure 4-24. The on-time background is shown as a dotted line.

in selecting the right width of timing cuts could also have an effect by subtracting too much or too little random background. The possibility of error from using the average polarization from each run is discussed in Appendix A. Any error introduced in this way will not cancel since it only appears once in the expression for the asymmetries. It is very difficult to determine a quantitative limit for the systematic error. Systematic error will be further discussed in the next chapter.

#### 4.2.5 The Angular Correlation Function $W(\theta)$ and the 4.44-MeV State

Besides the coincidence analyzing powers for the different polarizations, a knowledge of the 15.11-MeV peak amplitudes should in principle yield the correlation function  $W(\theta_\gamma, \phi_\gamma)$ . We examined data for right and left directions of scattered proton. For this case  $\theta_\gamma$  is the angle of the  $\gamma$  in the horizontal plane and now runs from  $0^\circ$  to  $360^\circ$  starting from some direction in the scattering plane— say the beam direction.  $W(\theta_\gamma)$  is computed for a particular angle of scattered proton,  $\theta_p$ , which in our case is the average value for the protons scattered into S2,  $7.7^\circ$ . Choosing the protons scattered to the right as our standard, those scattered to the left can be included if  $\theta \rightarrow 360^\circ - \theta$ , i.e. the system is rotated by  $180^\circ$  around the beam axis. For  $\gamma$ 's in the scattering plane and a particular value of  $\theta_p$ , the definition of  $W$  is:

$$W(\theta_\gamma; \theta_p) = \frac{\frac{d^2\sigma}{d\Omega_\gamma d\Omega_p}}{\int \frac{d^2\sigma}{d\Omega_\gamma d\Omega_p} d\Omega_\gamma} = \frac{\frac{d^2\sigma}{d\Omega_\gamma d\Omega_p}}{\frac{d\sigma}{d\Omega_p}}, \quad (4-3)$$

where now the cross sections are for unpolarized incident protons. Apart from overall normalization constants (including the  $d\sigma/d\Omega_p$  in the denominator of equation 4-3),  $W(\theta_\gamma)$  for a particular BGO  $i$  at  $\theta_\gamma$  is

$$W_i = \eta_{S2} \eta_i (N + QR)$$

where  $N$ ,  $Q$ , and  $R$  are as in equation 4-2. The efficiency  $\eta_{S2}$  is the relative efficiency for either S2 elements 11-13 or elements 3-5 in Figure 3-4, and must be included when comparing scattering to both right and left. The efficiency  $\eta_i$  is the efficiency for the

particular BGO, or if they are all normalized to one of them, BGO  $k$ , it is the relative efficiency  $\eta_i/\eta_k$ .

The relative BGO efficiencies were measured by using the source calibrations with the two radioactive sources (see section 3.4). However, sufficient care was not given to the placement of the source, to make sure that it was exactly at the target center position each time the source calibrations were done. Since the front face of the BGO's were only about 8 inches from the target center position, a 1 inch uncertainty in the placement of the source could yield a 25% difference in measurement for the efficiency of the BGO. Because of this problem it is felt that the data we have on  $W$  is unreliable and is therefore not presented. In the case of the data for the fall of 1986, when four new commercially-manufactured BGO's were used, and it might be expected that they had similar efficiencies, BGO's 1 and 3 did not produce useable spectra and so there were insufficient points to show the behaviour of  $W$ .

Problems also prevented our being able to present analyzing-power measurements or correlation function for the 4.44-MeV state of  $^{12}\text{C}$ . The main difficulty was that although the random background could be subtracted in the same way that was done for the 15.11-MeV state, the nearness to the 4.44-MeV peak of the discriminator electronic cut-off on the left-hand side of the peak prevented our being able to gauge the level of on-time, correlated background properly. An example of a typical 4.44-MeV spectrum is given in Figure 4-26. Judging also from the level of flat background to the right of the peak, the correlated background was not negligible, and often appeared to be 50% or more of the counts in the region of the 4.44-MeV peak. In addition, it could not be known for certain if the background rose, fell or stayed the same as one moved from the right-hand shoulder into the peak and toward the electronic cut-off.

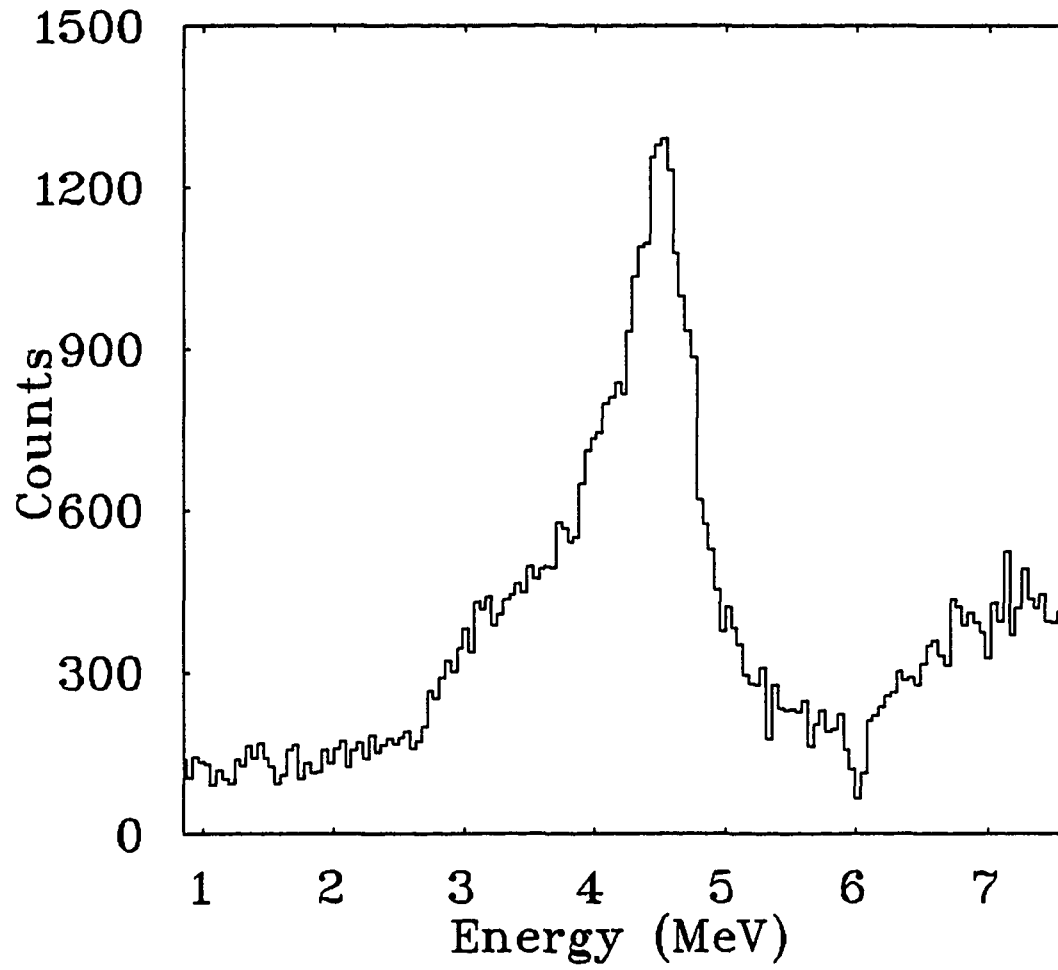


Figure 4-26: A typical 4.44-MeV peak. This is BGO 2 from summer 1986 longitudinal data.

## Chapter 5

### Results and Conclusions

#### 5.1 Presentation of the Results

We present the results graphically in Figures 5-1, 5-2, 5-3 and 5-4, and list the asymmetries in Table D-1, Appendix D. Figure 5-1 shows the normal polarization 1985 data and Figure 5-4 shows normal polarization data from 1986, at somewhat different BGO angles. The nonrelativistic distorted-wave calculation results from DW81 [RS77] (dashed line) and the relativistic distorted-wave treatment with explicit exchange from program DREX [Ros] (solid line) are also presented in the plots. The  $(p, p')$  amplitudes and the program to calculate the  $\gamma$ -ray coincidence analyzing powers from them were provided by Jorge Piekarewicz. Quantities calculated in the programs DW81 and DREX, which use the same reference frame as in Chapter 2, with axes  $\hat{x} = \hat{n} = \hat{p} \times \hat{p}' / |\hat{p} \times \hat{p}'|$ ,  $\hat{y} = \hat{k} = (\hat{p} + \hat{p}') / |\hat{p} + \hat{p}'|$  and  $\hat{z} = \hat{q} = \hat{n} \times \hat{k}$  ( $\hat{p}$  and  $\hat{p}'$  are unit vectors in the direction of the incident and final center-of-mass proton momenta), have been transformed here into a frame fixed in the laboratory. In our frame  $\phi_p$  angles are measured azimuthally around the beam direction or  $z$  axis, and the  $x$  axis or zero azimuth angle is horizontally toward the left looking downstream. The errors shown are the statistical only. As discussed in section 4.2.3, it was found necessary to combine three adjacent  $22.5^\circ$  scattered-proton azimuthal elements (see Figure 3-4) for better statistics. The theoretical calculations are thus correspondingly averaged over a range of azimuthal values. Note that since points in Figures 4 and 5 are separated by  $45^\circ$ , there is some overlap of data between adjacent points. In averaging the theoretical predictions the weighting was done with the theoretically predicted unpolarized cross section. (This does not seem to be a problem since both DW81 and DREX reproduce the unpolarized

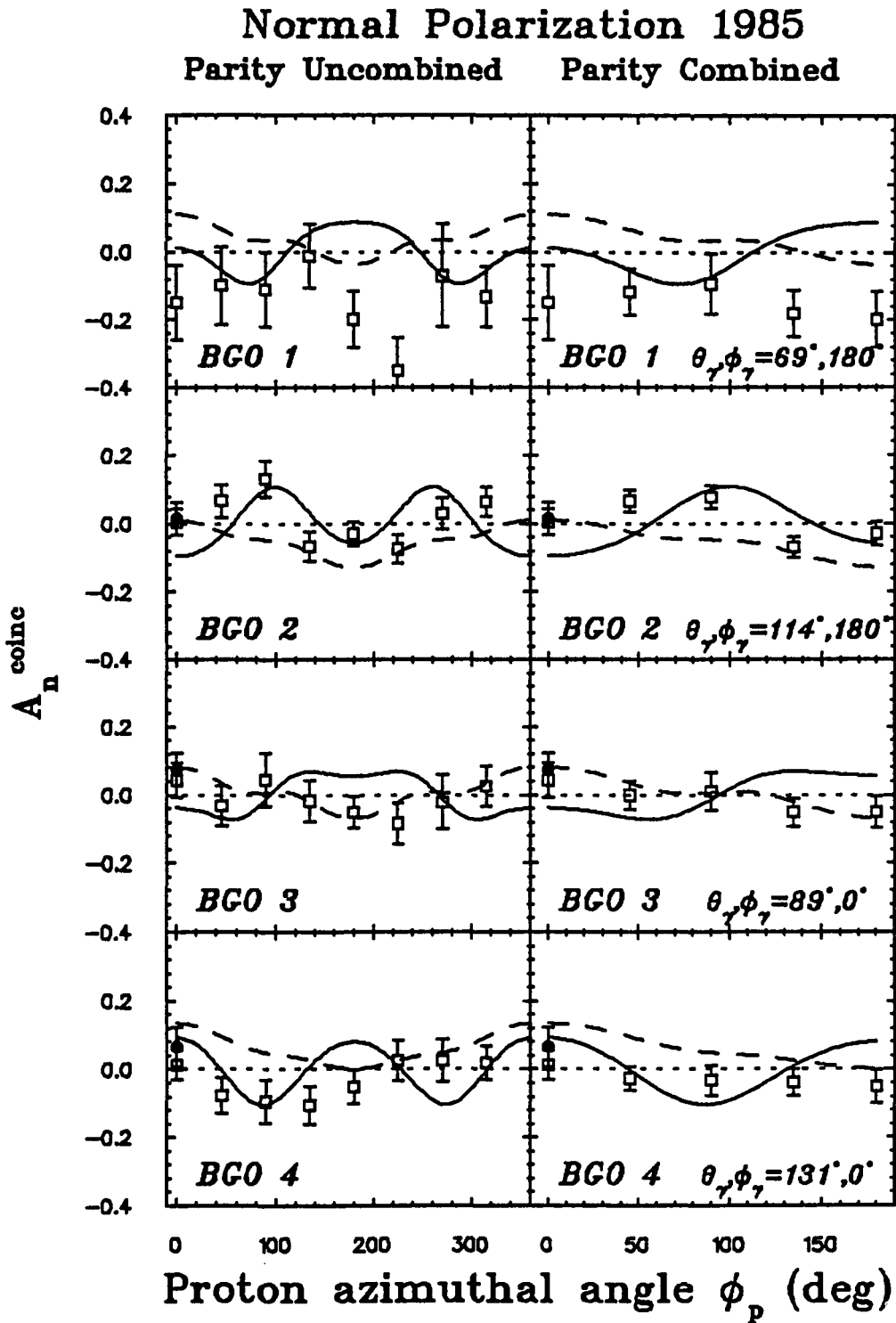


Figure 5-1:  $A_n^{\text{coinc}}$  for 1985 normal polarization data. The solid lines are DREX and the dashed lines are DW81. The solid points are data from Hicks *et al.* [Hic88].

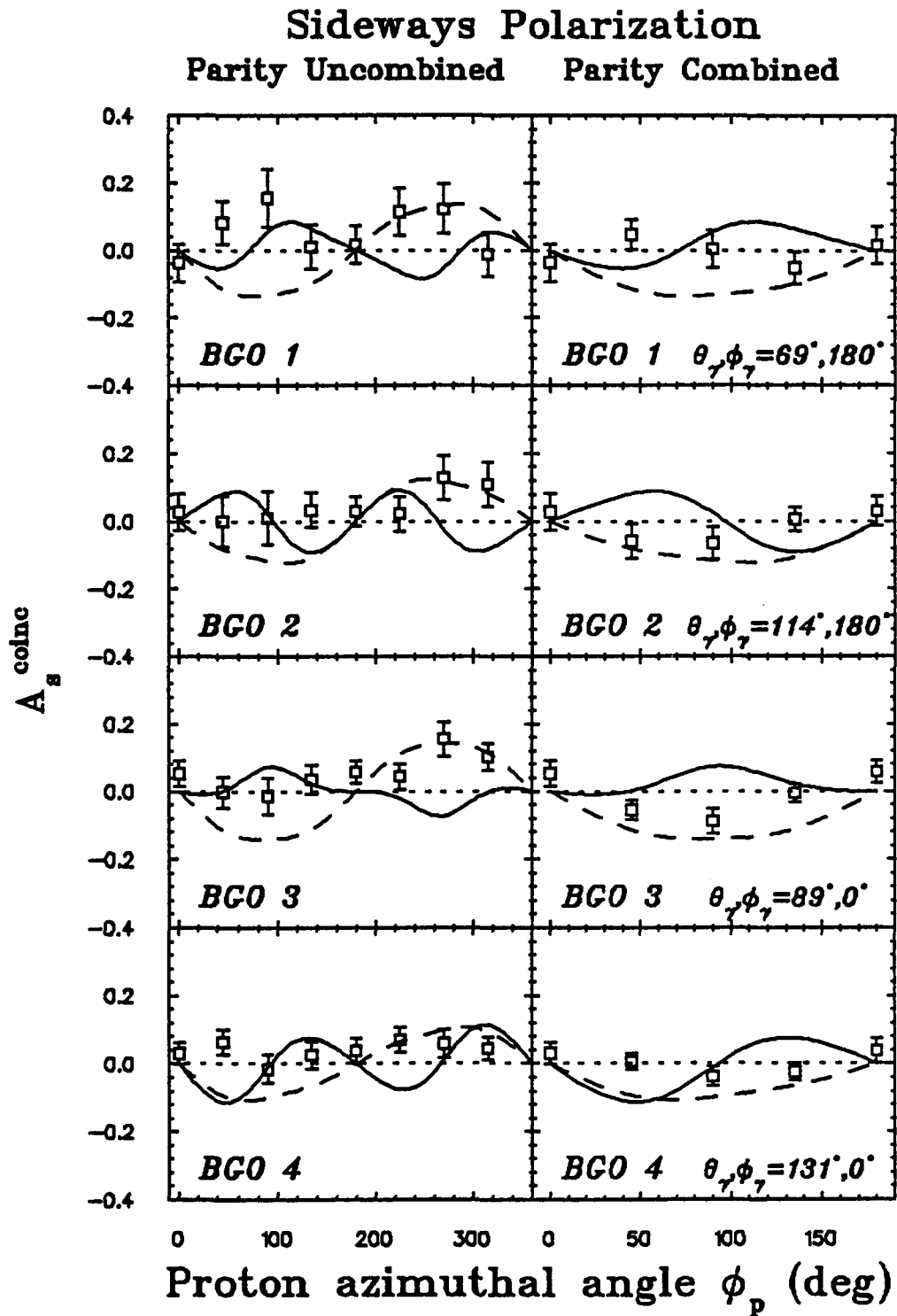


Figure 5-2:  $A_B^{coinc}$  for 1985 sideways polarization data. The solid lines are DREX and the dashed lines are DW81.

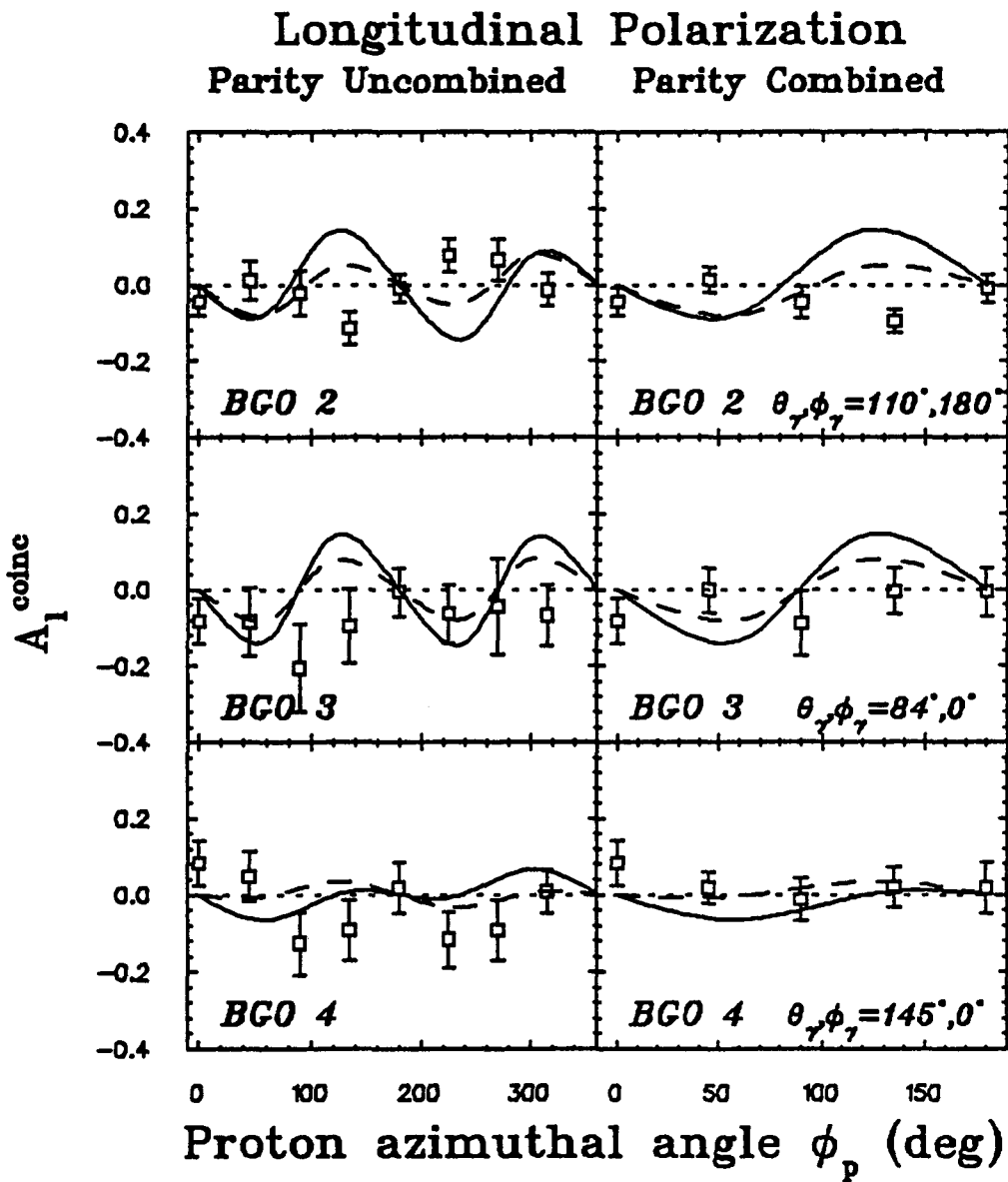


Figure 5-3:  $A_1^{\text{coinc}}$  for 1986 longitudinal polarization data. The solid lines are DREX and the dashed lines are DW81.

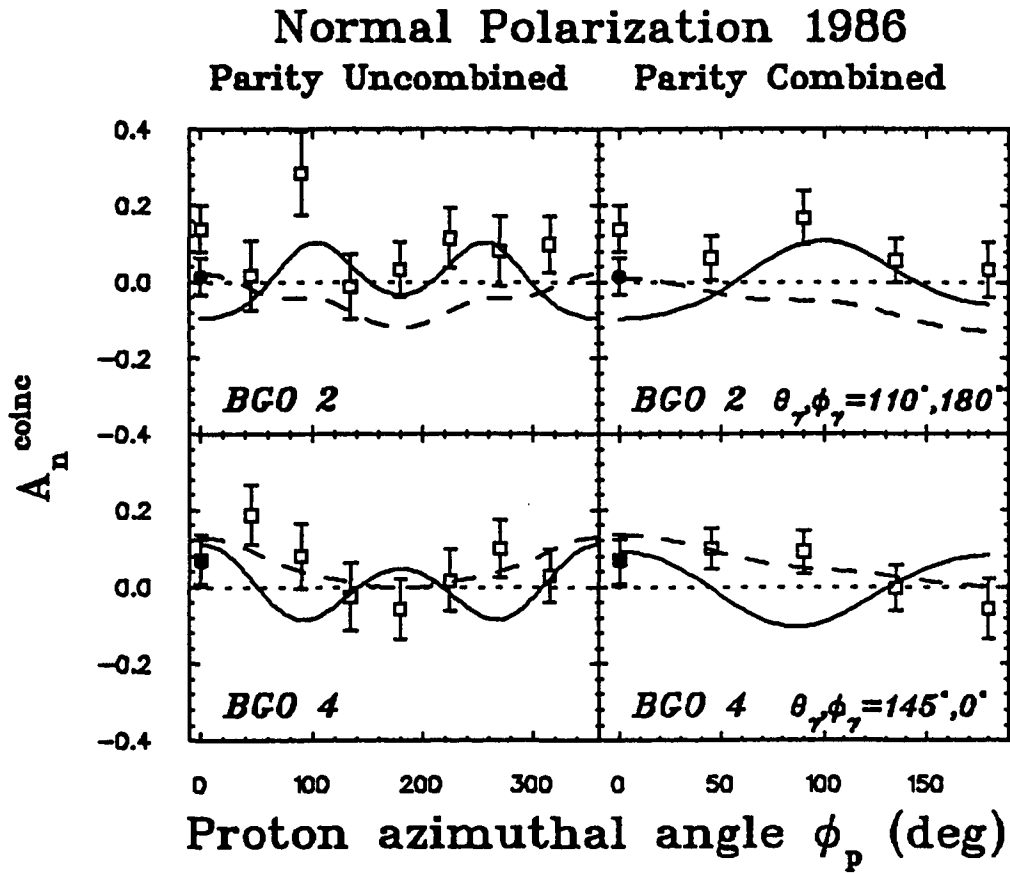


Figure 5-4:  $A_n^{\text{coinc}}$  for 1986 normal polarization data. The solid lines are DREX and the dashed lines are DW81. The solid points are data from Hicks *et al.* [Hic88].

cross section well for the angular range of S2 for 200 MeV data [CMF\*82, RS87].) The solid dots are data from Hicks *et al.* that correspond to our kinematics [Hic88]. Hicks *et al.* present data for normally polarized 400 MeV protons scattered to the left ( $\phi_p = 0^\circ$ ) at center of mass polar angles of  $\theta_p = 6.7^\circ, 8.9^\circ, 11.1^\circ$  and  $13.3^\circ$ , and  $\gamma$  rays emitted at 8 different angles greater than  $90^\circ$ . We have chosen  $6.7^\circ$  as the closest corresponding polar angle since using a 15.11-MeV state inclusive cross section weighting we get an average  $\theta_{cm}$  for S2 of  $7.3^\circ$ . The agreement is good between our data and theirs.

## 5.2 Parity Constraints

Parity and rotational invariance hold for the strong interactions, and place definite constraints on the observables that we measure. We will discuss these constraints and then discuss how they may be used to combine data and also give information on systematic error in the experiment. It is an easy matter to see what parity and rotational invariance require for our coincidence analyzing powers with the aid of some simple diagrams. Let us take as an example a proton scattered into either the top or bottom parts of S2 for sideways polarization. Figure 5-5a shows plan and elevation views of a proton scattered into the top of S2 with initial spin state spin-up, with the regular picture on the left and the parity-inverted view on the right, in which the momentum directions are inverted but the polarization direction does not change. (In the elevation views  $\otimes$  signifies a polarization direction into the page, and the BGO's are not shown for clarity.) Figure 5-5a is called measurement  $m_1$ . Figure 5-5b gives a similar schematic for the same situation except the opposite spin state ( $\odot$  signifies an arrow coming out of the page in the elevation view), and is measurement  $m_2$ . Figure 5-5c now gives a schematic for a spin-up proton scattered into the bottom of S2, and Figure 5-5d for the same process except the opposite spin state. Since the parity-inverted picture of Figure 5-5c can be made by a rotation to coincide with the regular picture for Figure 5-5b, Figure 5-5c is also measurement  $m_2$ . (The regular picture for Figure 5-5c also coincides with

the parity picture for Figure 5-5b.) Similarly Figure 5-5d is measurement  $m_1$  because it coincides with the opposite parity picture of Figure 5-5a.

Since the asymmetry for top is

$$\frac{m_1 - m_2}{m_1 + m_2}$$

and for bottom is

$$\frac{m_2 - m_1}{m_1 + m_2} ,$$

parity and rotational invariance require that  $A_S^{coinc}(top) = -A_S^{coinc}(bottom)$ , where the  $S$  refers to sideways polarization. Similar methods show that  $A_S^{coinc}(right) = A_S^{coinc}(left) = 0$  and that the asymmetry for each scattered proton angle and a given BGO direction is the negative of the asymmetry for the same direction of BGO and a scattered proton direction that is reflected in the horizontal plane ( $360^\circ - \phi_p$ ). The same relationships hold for longitudinal polarization. (Note also that longitudinal polarization can have no *inclusive*, or singles, analyzing power, *i.e.* without a  $\gamma$  detected, since rotational invariance makes all directions of scattered proton equal.)

For normal polarization the same process of drawing schematic diagrams reveals a different relationship. In this case  $A_N^{coinc}(top) = A_N^{coinc}(bottom)$  and  $A_N^{coinc}(\phi_p) = A_N^{coinc}(360^\circ - \phi_p)$ , *i.e.* the asymmetries for proton scattering angles reflected through the horizontal plane are equal. In this case there is no constraint for protons scattered to the right or left as in the longitudinal and sideways cases, where the asymmetries were required to be zero.

### 5.3 Discussion of the Results

We first discuss the left-hand sides of Figures 5-1, 5-2, 5-3, and 5-4, where the data from 8 different directions of proton azimuthal angle are presented. The parity constraints discussed in the last section require that in the case of the normal polarization data, Figures 5-1 and 5-4, the points should show symmetry about a vertical line through

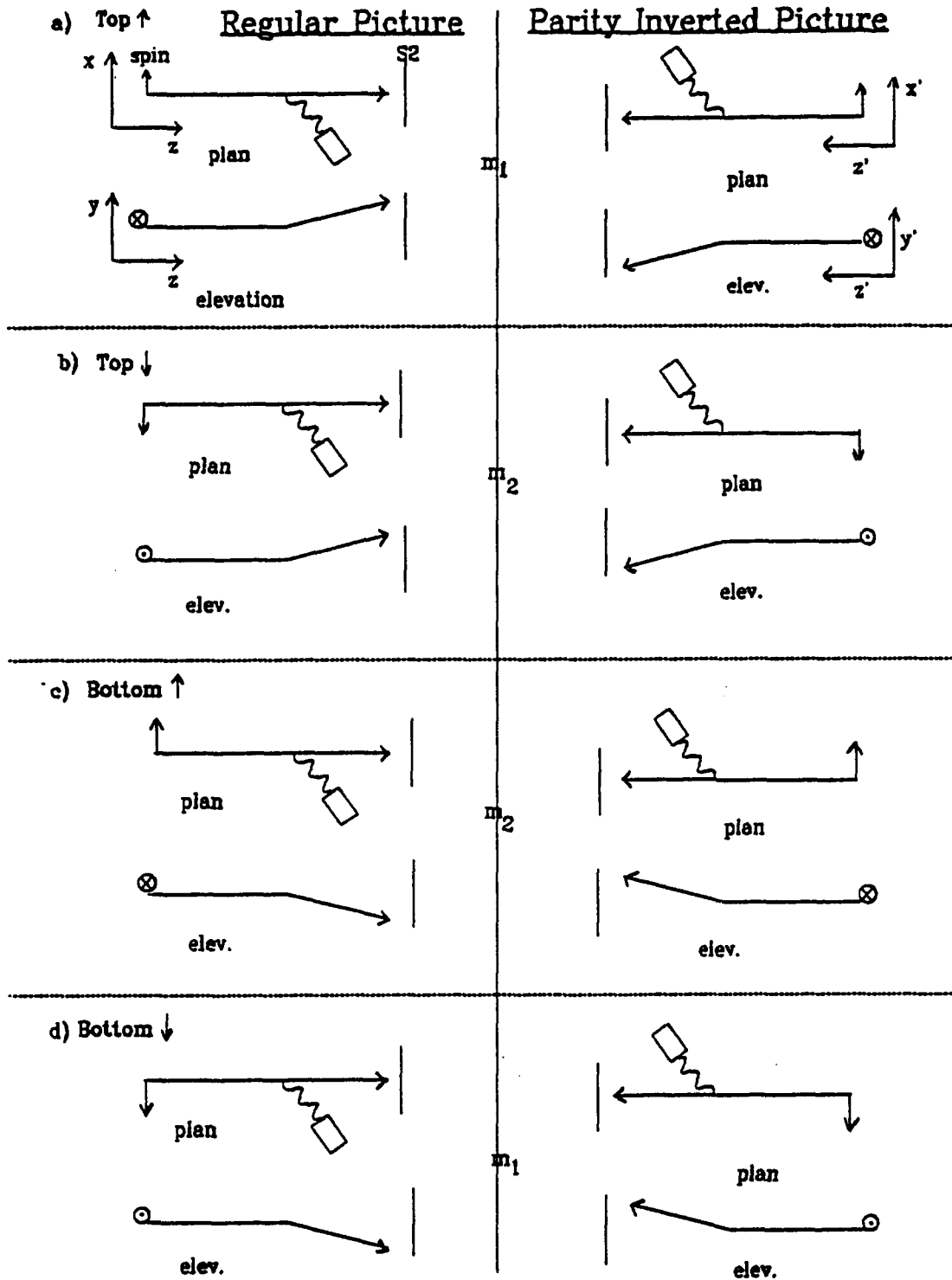


Figure 5-5: Regular and parity inverted schematic views of scattering to top and bottom parts of S2 with sideways polarization. (In the elevation views  $\otimes$  and  $\odot$  signify polarization direction into and out of the page respectively, and the BGO's are not shown for clarity.)

the middle of the plot at  $\phi_p = 180^\circ$ , and for sideways and longitudinal polarization data, there should be antisymmetry about the same vertical line. The positions of the data points do not clearly follow these constraints, but perhaps this is explained by the fact that the error bars are large.

To evaluate the extent of non-agreement with the parity constraints, we examine the distribution of observables that should equal zero because of parity invariance. For sideways and longitudinal polarization, we add  $a_{45} + a_{315}$ ,  $a_{90} + a_{270}$ , and  $a_{135} + a_{225}$ , where  $a_n$  represents the asymmetries at  $\phi_p = n$  degrees, and see if the sums are close to zero (when compared to their propagated uncertainties). We can also include  $a_0$  and  $a_{180}$  by themselves for comparison, since they should separately equal zero. For normal polarization we use instead  $a_{45} - a_{315}$ ,  $a_{90} - a_{270}$ , and  $a_{135} - a_{225}$ , and now  $a_0$  and  $a_{180}$  may not be considered, since parity invariance makes no prediction about their value. These results in units of  $\sigma$  (*i.e.* the propagated standard deviation or uncertainty) are presented in Table 5-1, and their distribution in Figure 5-6. The standard deviation of this distribution, *i.e.* the square root of the average square deviation from zero, is  $1.22 \pm 0.14$ , which is slightly more than the expected value of 1.0, and indicates the possibility of some systematic error. Out of a total of 53 measurements, 52.8% are 1  $\sigma$  or more away from zero, which is more than can be expected from statistics alone if the deviations are normally distributed (in which case we would expect only 32% to be more than 1  $\sigma$  from zero).

In looking at the sideways data, it is apparent that there is a preponderance of positive points, when parity invariance predicts an equal number of positive and negative points. This immediately raises several questions. First, perhaps the value of the ratio of normal to reverse beam current monitors,  $Q$ , has a value which is too low. A problem with having the computer-busy wire unhooked while the sideways polarization data was being collected was discussed in section 4.2.2, and indeed the effect is in the right

Normal 1985		Sideways 1985		Longitudinal 1986		Normal 1986
0.23	-1.34	-0.65	1.40	-1.15	1.44	-0.69
-0.22	-1.34	0.75	1.63	-0.02	0.63	1.42
2.48		2.45	1.89	0.55	-1.93	-1.10
0.05		1.30	1.40	-0.61	-1.97	1.52
1.43		0.29	1.69	-0.26	0.26	-0.17
0.13		0.49	0.95	-1.37		-0.36
-0.68		1.09	2.21	-1.26		
0.60		1.36	0.75	-1.46		
0.79		0.76	1.80	-1.29		
-1.35		0.69	1.07	-0.10		

Table 5-1: Combinations of the asymmetries that should equal zero by parity invariance, divided by their standard deviations. See text.

direction, but as was shown in that section it is not enough of an effect to account for what is seen. A good indication that  $Q$  is not significantly in error is the asymmetry in the off-time ADC spectrum for sideways and normal polarization data, shown in Figures 5-7 and 5-8. Since off-time means there is no correlation between the  $\gamma$  and the proton, with the  $\gamma$  merely acting as a random strobe, the asymmetry measured is of the proton singles, which are mostly elastics. For the normal and sideways polarization data, the fact that the clear patterns in Figures 5-7 and 5-8 are centered vertically on the zero line indicates  $Q$  is not significantly in error. For the longitudinal data, for which the asymmetry is expected to be zero for all values of  $\phi_p$  because of parity and rotational invariance, the off-time spectra indicate that  $Q$  may be underestimated by about 7%.

The same evidence argues against the source of the problem (for normal and sideways polarization data) being a difference in the amount of polarization between periods of normal and reverse polarization. LAMPF at the time the experiment was performed only reported the value of the average polarization (including both directions of polarization) per hour (it has since changed to giving a separate average value for each of the two directions), and the polarization value was nominally the same for both normal and reverse [vD90]. If the difference was appreciable, the plots in Figures 5-7 and 5-8 would

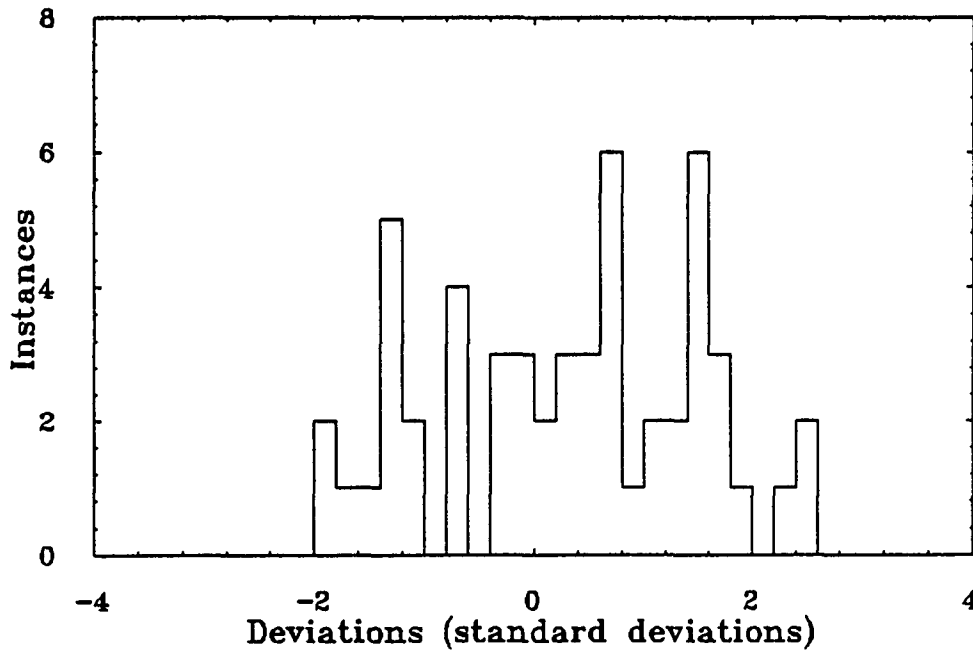


Figure 5-6: Distribution of the values in Table 5-1. These are combinations of the asymmetries for all directions of polarization, divided by their standard deviations. See text.

also no longer be centered vertically. Again, for the longitudinal data the fact that these plots are not centered vertically may indicate a difference in polarization value between normal and reverse polarization times.

The question of background contamination causing the deviations from parity invariance also arises. However, since any process that contaminates our measurement of the 15.11 MeV state should also obey the parity constraints, this is not a possible source of the problem. For example, if the contaminating background had an asymmetry it should also show an antisymmetric pattern around  $\phi_p = 180^\circ$  for sideways and longitudinal data, and the combined asymmetry should still be antisymmetric about  $\phi_p = 180^\circ$ . (If the background does not have an asymmetry it should merely dampen the magnitude of our measured 15.11-MeV asymmetry without causing it to lose its antisymmetric characteristic, or symmetric for normal polarization.)

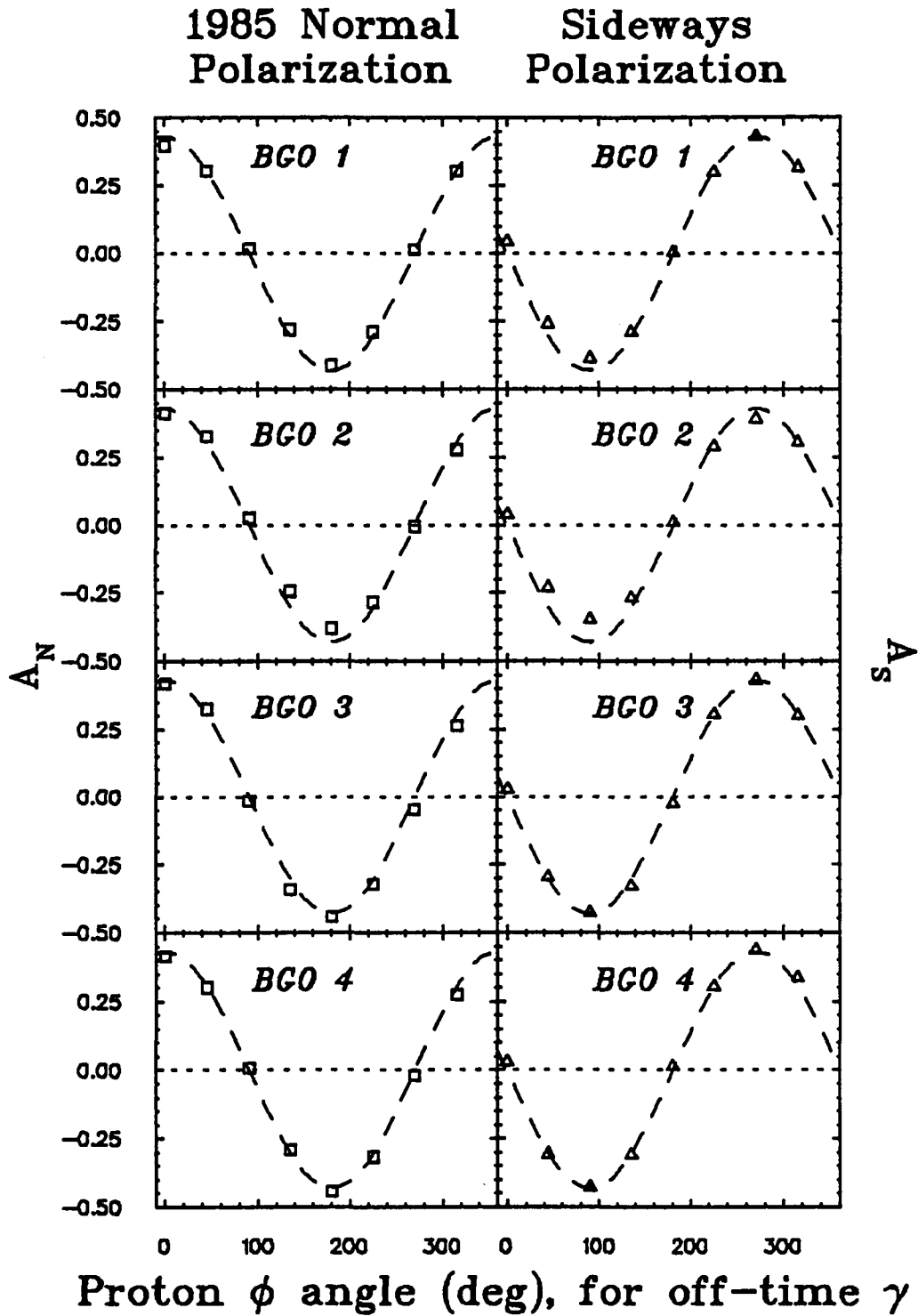


Figure 5-7: The off-time asymmetries (whole spectrum) for normal and sideways polarizations, 1985. The dashed lines are  $0.43 \cos$  and  $-0.43 \sin$ .

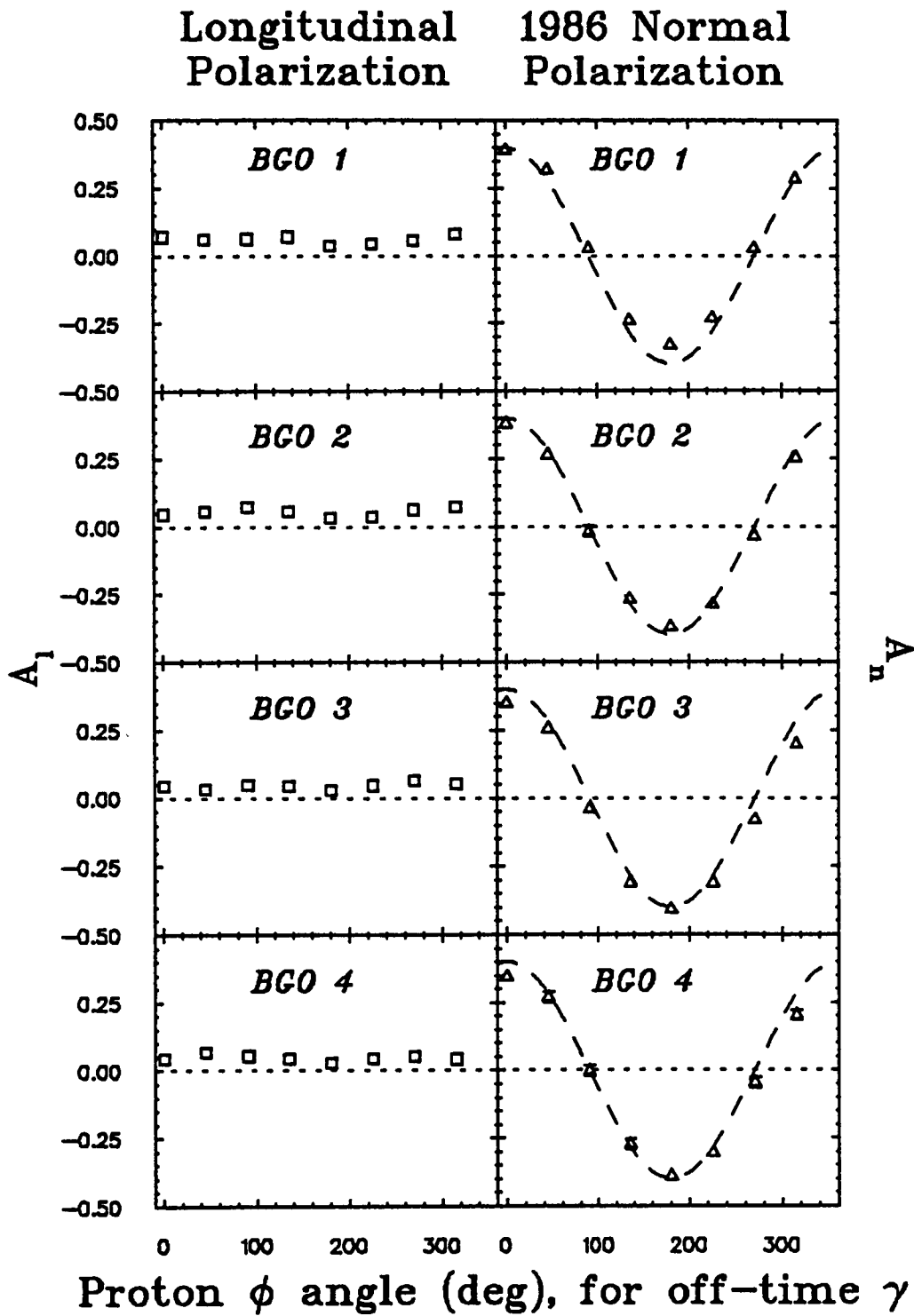


Figure 5-8: The off-time asymmetries (whole spectrum) for longitudinal and normal polarizations, 1986. The dashed line is  $0.4 \cos$ .

The possibility remains that our error bars are too small and therefore the calculations of the deviations in Table 5-1 are exaggerated. In the fitting of the ADC spectra we have assumed that we know more than we actually do. For instance we assume that we know the centroid position and width of the convoluting gaussian perfectly in that these items (from 6-parameter fits of data from both directions of polarization and all azimuthal angles of scattered proton  $\phi_p$ ) are fixed in the final fit (2-parameter of data from only one direction of polarization and  $\phi_p$ ) that determines the 15.11-MeV peak amplitude. However, a study was done of BGO 2 for the sideways data in which the peak width and centroid position was varied by one standard deviation from the value given by the (6-parameter) fit of the combined data, and this change resulted in less than a 1% effect on the 15.11-MeV peak amplitudes. A more probable source of error is that the shape of the background is assumed to be a particular form and any error inherent in this assumption is not manifested in the error bars in Figures 5-1, 5-2, 5-3, and 5-4. A study was done of the BGO 2 sideways polarization data to see what effect using a different functional form for the on-time background would have on the asymmetries. A quadratic polynomial ( $ax^2 + bx + c$ ) was used for the background in all the fits for this study, and the magnitude of the change in each of the eight asymmetries (when compared to the asymmetries derived with the exponential background form) was at most 0.022, with the average magnitude of the change being 0.012. (Seven of the eight changes were in the positive direction.) We conclude that the error bars in the plots are probably too small, and that uncertainty in the background shape is a likely source of additional (systematic) error.

#### 5.4 Use of Symmetries to Combine Data

With this *caveat* in mind (that the deviations from parity predictions are more than what is expected from statistical uncertainty alone), we turn to the right-hand side of Figures 5-1, 5-2, 5-3, and 5-4 where the parity invariance requirements have

been used to combine data points, and we consequently show  $\phi_p$  only between  $0^\circ$  and  $180^\circ$ . In the case of sideways and longitudinal polarization, the 3 pairs of points  $\phi_p = (45^\circ, 315^\circ), (90^\circ, 270^\circ)$  and  $(135^\circ, 225^\circ)$  have been combined as

$$A = \frac{N_1 + QR_2 - QR_1 - N_2}{N_1 + QR_2 + QR_1 + N_2}$$

and for normal polarization the same pairs have been combined as

$$A = \frac{N_1 + N_2 - QR_1 - QR_2}{N_1 + N_2 + QR_1 + QR_2}$$

The error bars are smaller and as discussed above probably underestimated, and yet the procedure should be valid if the main source of the error is statistical.

A second attempt at using symmetries to combine data points is seen in the top part of Figure 5-9, where BGO1 and 2 have been combined into BGO A for further improvement in statistics ( BGO's 3 and 4 are the same as in Figures 5-1 and 5-2, and are included in Figure 5-9 for comparison as discussed below.) Rotational invariance requires that data from BGO 1 at  $\phi_p = a$  will have an asymmetry with the same magnitude but opposite sign from an asymmetry at a point  $\phi_p = a + 180^\circ$  for a BGO position at the same  $\theta_\gamma$  value ( $69^\circ$ ) but reflected through the  $x-y$  plane ( $\phi_\gamma = 0^\circ$  instead of  $180^\circ$ ). A second symmetry requires that the measured asymmetry be the same for detectors at diametrically opposed  $\gamma$ -ray detector center-of-mass angles (see equation 2-9), and so the position of BGO 1 that has been reflected from its original position at  $\theta_\gamma, \phi_\gamma = 69^\circ, 180^\circ$  through the  $x-y$  plane to  $\theta_\gamma, \phi_\gamma = 69^\circ, 0^\circ$  is then reflected through the origin to  $\theta_\gamma, \phi_\gamma = 111^\circ, 180^\circ$ . This is only  $6^\circ$  from BGO 2 at  $\theta_\gamma, \phi_\gamma = 117^\circ, 180^\circ$ , which is small compared to the  $20^\circ$  acceptance of each BGO, and so the corresponding points have been combined into BGO A at the mean  $\theta_\gamma$  value of  $114^\circ$ . (See Appendix D for the values of the asymmetries and errors.)

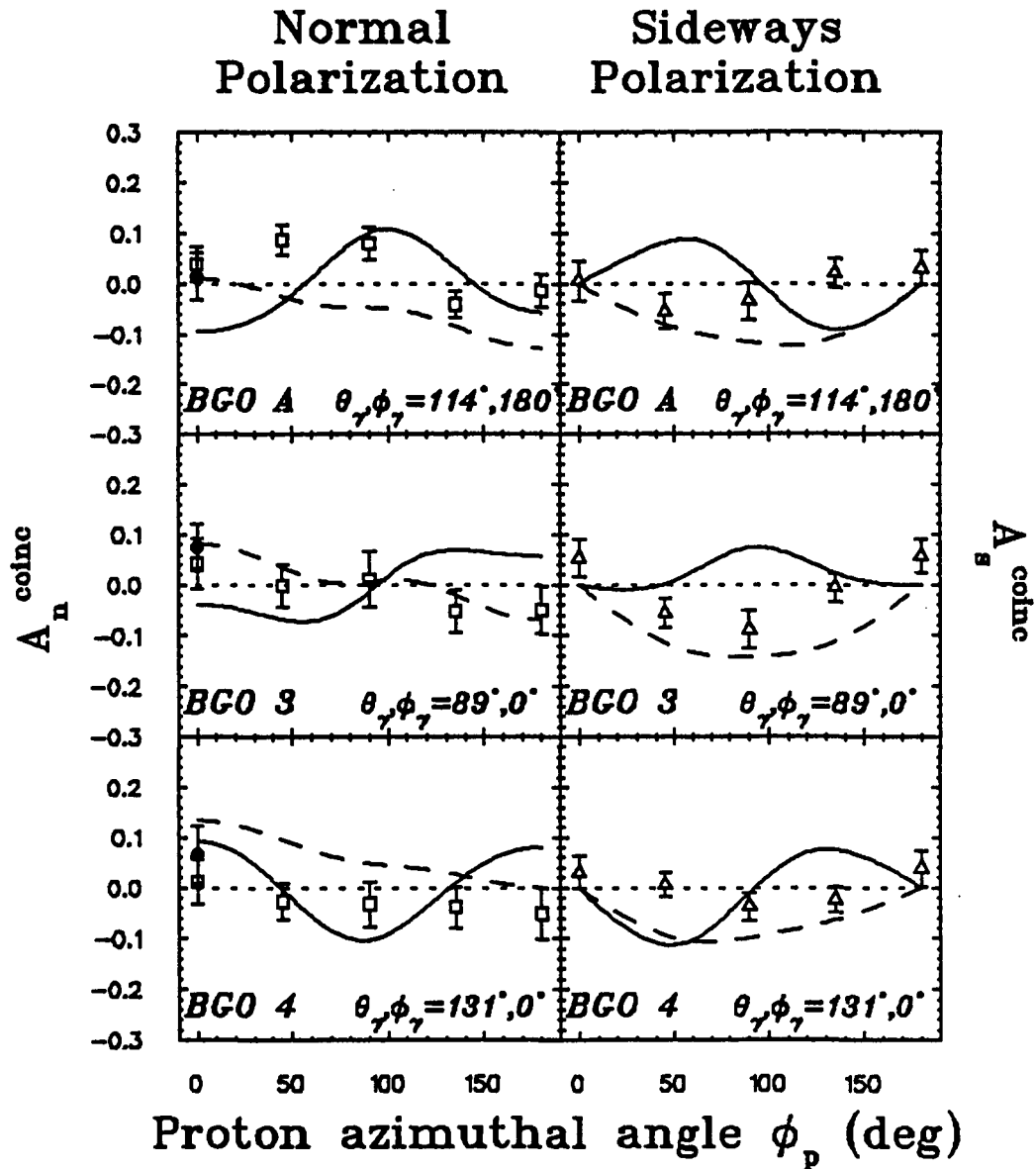


Figure 5-9: BGO's 1 and 2 have been combined into BGO A as described in the text. BGO's 3 and 4 are the same as in Figures 5-1 and 5-2, reproduced here to aid in seeing any trends. See the text.

## 5.5 Conclusion

In general the magnitude of the asymmetries in Figure 5-9 and the right-hand sides of Figures 5-3 and 5-4 found is slightly less than the size predicted by both relativistic and non-relativistic models, and also consistent with zero. Using the parity-combined asymmetries and the combination of BGO's 1 and 2 as BGO A, the overall (all three types of polarization) root-mean-square asymmetry for our data was  $.060 \pm .007$ ; for DREX predictions at the same points it is .063, and for DW81 at those points it is .065.

The normal polarization data for BGO's 2 and 4 in 1985 shows some limited agreement (with exceptions) with the 1986 normal polarization data. However, neither model follows our data well. The sideways data also does not clearly favor either model. The data for BGO 3 shows some tendency toward the DW81 prediction. In the case of the longitudinal polarization data there seems to be a difference of sign with both of the predictions. From the form of the strongest component of the longitudinal analyzing power,  $D_{0k}$ , in equation 2-1, and from an examination of the relative magnitudes of the theoretically predicted amplitudes, this could be caused by a wrong sign in  $A_{nn}$  (see equation 2-2).

The plots in Figures 5-3 and 5-9 are arranged so that they are in vertically descending  $\theta_\gamma$  order, in order to show trends in both the data and the predictions as  $\theta_\gamma$  changes. (BGO A of normal and sideways polarizations at  $\theta_\gamma, \phi_\gamma = 114^\circ, 180^\circ$  is equivalent to one at  $\theta_\gamma, \phi_\gamma = 66^\circ, 0^\circ$  because of the third symmetry mentioned above, and BGO 2 of longitudinal polarization with  $\theta_\gamma, \phi_\gamma = 110^\circ, 180^\circ$  is equivalent for the same reason to  $\theta_\gamma, \phi_\gamma = 70^\circ, 0^\circ$ .) For normal polarization the data behaves opposite from the trend in the DW81 prediction, since its average value decreases whereas the average value of the DW81 predictions increases. In the other cases the data also does not seem to follow the trends of the predictions.

As mentioned in Chapter 1, Hicks *et al.* have measured the coincidence analyzing

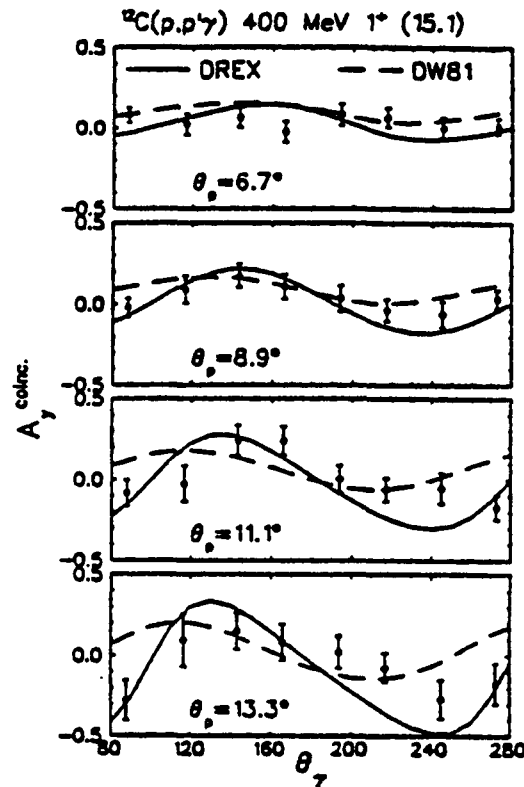


Figure 5-10: Data of Hicks *et al.* The BGO's are in the horizontal plane and  $\theta_\gamma$  is in the lab frame measured from the beam direction (counter-clockwise looking down). The proton is scattered to the left.

power  $A_y^{\text{coinc}}$  (equivalent to our  $A_n^{\text{coinc}}$  for scattering to the left) for normal polarization at several  $\theta_p$  angles using a magnetic spectrometer. Their data is presented in Figure 5-10. Their data shows a definite variation with polar angle  $\theta_p$  and thus raises questions about our procedure of averaging over the angular range of S2. Their data was not available when our experiment was performed, and also, as mentioned in section 4.2.3, we were originally intending to be able to distinguish smaller angular bites both in  $\theta_p$  and  $\phi_p$ , but were led to combine parts of the data that could be distinguished by S2 because of the need for better statistics. However, the theoretical predictions have also been averaged over the angular range of S2 and so should still give an indication of the agreement (or lack of it) of our data with the two different models.

In summary, the coincident analyzing-power measurements are of about the same

average magnitude as the predictions for both the nonrelativistic and relativistic reaction models, but do not show agreement in detail when compared with either model.

## APPENDIX A

### Evaluation of the Polarization Averaging Approximation

In computing the asymmetries, we have used the average value of the inverse of the polarization,  $\overline{\frac{1}{p}} = \frac{1}{N} \sum (\frac{1}{p})_i$ , so that our asymmetry is  $A' = \overline{A} \cdot \overline{(\frac{1}{p})}$ , where  $\overline{A} = \frac{1}{N} \sum (\frac{N_i - R_i}{N_i + R_i})$ , instead of  $A' = \frac{1}{N} \sum \frac{N_i - R_i}{p_i(N_i + R_i)}$ , where the  $i$ 's refer to the hourly divisions for which we have polarization readings. In this appendix we will establish the validity of this use.

Letting  $x = A$ ,  $y = \frac{1}{p}$ , the question is:

$$\frac{1}{N} \sum_{i=1}^N f(x_i, y_i) \stackrel{?}{=} f(\overline{x}, \overline{y}) \quad (\text{A} - 1)$$

Taylor expanding and keeping only terms up to second order (higher derivatives are 0),

$$f(x_i, y_i) = f(\overline{x}, \overline{y}) + \frac{\partial f}{\partial x} \Delta x_i + \frac{\partial f}{\partial y} \Delta y_i + \frac{1}{2} \frac{\partial^2 f}{\partial x^2} (\Delta x_i)^2 + \frac{1}{2} \frac{\partial^2 f}{\partial y^2} (\Delta y_i)^2 + \frac{\partial^2 f}{\partial x \partial y} \Delta x_i \Delta y_i$$

Let  $\Delta$  be the difference between the left-hand and right-hand sides of equation 1. Then

$$\begin{aligned} \Delta &= \frac{1}{N} \sum f(x_i, y_i) - f(\overline{x}, \overline{y}) \\ &= \{f(\overline{x}, \overline{y}) + \frac{1}{N} [\frac{\partial f}{\partial x} \sum \Delta x_i + \frac{\partial f}{\partial y} \sum \Delta y_i \\ &\quad + \frac{1}{2} \frac{\partial^2 f}{\partial x^2} \sum (\Delta x_i)^2 + \frac{1}{2} \frac{\partial^2 f}{\partial y^2} \sum (\Delta y_i)^2 + \frac{\partial^2 f}{\partial x \partial y} \sum \Delta x_i \Delta y_i]\} \\ &\quad - f(\overline{x}, \overline{y}) \\ &= \frac{1}{N} [\frac{1}{2} \frac{\partial^2 f}{\partial x^2} \sum (\Delta x_i)^2 + \frac{1}{2} \frac{\partial^2 f}{\partial y^2} \sum (\Delta y_i)^2 + \frac{\partial^2 f}{\partial x \partial y} \sum \Delta x_i \Delta y_i] \end{aligned}$$

since the average deviations  $\Delta x_i$  and  $\Delta y_i$  from the mean are zero. Also in our case

$f = xy$  and  $\frac{\partial^2 f}{\partial x^2} = \frac{\partial^2 f}{\partial y^2} = 0$  and  $\frac{\partial^2 f}{\partial x \partial y} = 1$  and so

$$\Delta = \frac{1}{N} \sum \Delta x_i \Delta y_i = \frac{1}{N} \sum \Delta A_i \Delta (\frac{1}{p})_i$$

If  $A$  and  $\frac{1}{p}$  were uncorrelated this difference  $\Delta$  would be zero on the average. But these quantities are correlated in our case. However, we can get an estimate for how big this deviation is, for example, for the normal polarization data of fall of 1985. The root-mean-square deviation of  $\frac{1}{p}$  is given from the LAMPF polarimeter hourly readings as .09389. We do not have access to the values of  $A_i$  since we only have one value for each asymmetry computed for all the fall 1985 normal polarization data, and not an asymmetry for each hour as we do for the polarization readings. However, the analyzing power is some value  $\alpha$  and we measure an asymmetry  $A_i$ , then assuming a linear relationship between  $A_i$  and  $p_i$

$$\alpha = \frac{1}{p_i} A_i \quad .$$

Using the maximum analyzing power (taking into account combining of data using symmetries) of .14 measured for normal polarization (this is also the largest we measured for any direction of polarization) for  $\alpha$ , the  $\Delta A_i \leq \Delta p_i \times .14$ , and using the root-mean-square  $\Delta p_i$  of .058, which we can obtain from the polarization readings, a reasonable approximation for  $\frac{1}{N} \sum \Delta A \Delta (\frac{1}{p})$  will be  $(\Delta \frac{1}{p}) \Delta p_i \times .14 = .094 \times .058 \times .14 = .00076$ . Since this is much less than  $\bar{A} \cdot \overline{(\frac{1}{p})}$ , which is approximately .14, our original approximation is warranted, and  $A' \cong \bar{A} \cdot \overline{(\frac{1}{p})}$ .

## APPENDIX B

### The Monte Carlo Program BGOPIOMC

This program, which is described in section 4.2.3.8, calculates the energy spectrum for  $\gamma$ 's decaying from  $\pi_0$ 's for the geometry of this experiment. The program incorporates EGS4 [NHR85], and is written in MORTRAN, for which information is available in Ref. [NHR85]. Other references are [Per82b], [Gol80], [Per82a], and [BW64].

```
PROGRAM BGOPIOMC;
"STEP 1 USER-OVER-RIDE-OF-EGS-MACROS"
REPLACE {$MXMED} WITH {1}
REPLACE {$MXREG} WITH {4}
REPLACE {$MXSTACK} WITH {15}
REPLACE {$MXPLNS} WITH {2}
REPLACE {$DETRAD} WITH {1.5}
"REPLACE {$DIST} WITH {7.875}"
REPLACE {$DIST} WITH {8.4375}
REPLACE {$DETLNG} WITH {3.}
REPLACE {$EBIN} WITH {200}
REPLACE {$MXCYLS} WITH {75}
REPLACE {$DELCYL} WITH {1.0E-4}
REPLACE {;COMIN/EDGE/;} WITH
  {;COMMON/EDGE/IEDGFL($MXREG), $LGN(EKALPH,EKBETA,BKR1,BKR2($MXMED));}
REPLACE {;COMIN/RANDOM/;} WITH {;COMMON/RANDOM/ISEED;}
REPLACE {$RANDOMSET#;} WITH
  {{P1}=RAN(ISEED);}
;COMIN/EDGE,BOUNDS,MEDIA,MISC,PLADTA,DEBUG,CYLDTA,THRESH,RANDOM/;
$ENERGY PRECISION E,EI;
CHARACTER*1 LINE(48);
DIMENSION EBIN($EBIN);
DIMENSION IBGOG1(4),IBGOG2(4),IPDH5(16);
DIMENSION IPADIF(32),IPAD(16),IBGOP5(4);
COMMON /SCORE/EHIST;

"STEP 2 PRE-HATCH-CALL-INITIALIZATION"
$TYPE MEDARR(24) /$S'BGO',21*' '/;
DO I=1,24[MEDIA(I,1)=MEDARR(I);]
NREG=4; "NUMBER OF REGIONS (LOCAL VARIABLE)"
NMED=1; "NUMBER OF MEDIA"
MED(1)=0;
MED(2)=1; ECUT(2)=0.611; PCUT(2)=0.001;
MED(3)=0;
```

```

MED(4)=0;
BWIDTH=150./$EBIN;
DUNIT=1; "EVERYTHING IS IN CM"
IRAYLR(2)=1; "TURN ON THE RAYLEIGH SCATTERING"
IRAYLR(1)=0; IRAYLR(3)=0; IRAYLR(4)=0;
"IEDGFL(2)=0; TURN ON THE FLUORESCENCE PHOTON (13=AL, 29=CU)"
"IEDGFL(1)=0; IEDGFL(3)=0;"
"NBGO=1;BGTH=295.;"
NBGO=4;BGTH=145.;
DO J=1,4[IBGOG1(J)=0;IBGOG2(J)=0;IBGOP5(J)=0;]
DO J=1,16[IPDH5(J)=0;IPAD(J)=0;]
DO J=1,32[IPADIF(J)=0;]
"RECOIL PROTON K.E. FIXED AT 100 MEV"
ISEED=123456;T1=318.;PI=3.1415927;T3=100.;
IHITBG=0;DR=PI/180.;
CBG=COS(BGTH*DR);SBG=SIN(BGTH*DR);
"RECOIL PROTON POLAR ANGLE FIXED AT 7 DEG"
TH3=7.*DR;CTH3=COS(TH3);STH3=SIN(TH3);
XM1=938.28;XM2=XM1;XM3=XM1;XM4=134.96;XM5=XM1;
XMP2=XM1*XM1;XMPI2=XM4*XM4;
E3=XM3+T3;P1=SQRT(T1*(T1+2*XM1));P2=0.;
E1=T1+XM1;E2=XM2;EB=E1+E2;
"FIND CM LORENTZ PARMS"
ES=SQRT(EB**2-P1**2);
GB=EB/ES;XNB=P1/ES;BB=XNB/GB;
P3=SQRT(E3**2-XMP2);P3PARC=GB*(P3*CTH3-BB*E3);P3PERP=P3*STH3;
P3C2=P3PARC**2+P3PERP**2;P3C=SQRT(P3C2);
TH3C=ACOS(P3PARC/P3C);TH3C=PI-TH3C;SXC=SIN(TH3C);CXC=COS(TH3C);
SB1=SIN(TH3C);CB1=COS(TH3C);
E3C=SQRT(P3C2+XMP2);EX=ES-E3C;PX=P3C;
"CAF1 USED LATER IN ROTATING FROM PX TO CM FRAMES"
CAF1=PX/P3PERP;
XMX2=EX**2-PX**2;
"FIND LIMITS OF PIO ENERGY IN CM"
E452=XMX2+XMPI2-XMP2;
E4RG=EX**2+E452**2-XMX2*(E452**2+4*PX*PX*XMPI2);
IF(E4RG.LT.0.)[OUTPUT E4RG;(' E4RG ',E12.5);]
E4RAD=SQRT(E4RG);
E4ONE=(EX*E452+E4RAD)/2/XMX2;E4TWO=(EX*E452-E4RAD)/2/XMX2;
IF(E4ONE.GT.E4TWO)[E4MAX=E4ONE;E4MIN=E4TWO;]
ELSE[E4MAX=E4TWO;E4MIN=E4ONE;]
OUTPUT E4ONE,E4TWO,E4MAX,E4MIN;(' 1,2,MAX,MIN',/1X,4(1X,E12.5));

"STEP 3 HATCH-CALL"
CALL HATCH;

"STEP 3.1 SET UP K_EDGE PARAMETERS NEEDED BY "
" SUBROUTINE PHOTON "
"CALL EDGSET; "

"STEP 4 INITIALIZATION-FOR-HOWFAR"
DO I=1,$MXPLNS

```

```

[DO J=1,2
  [PCOORD(J,I)=0.0;
  PNORM(J,I)=0.0;]]
CYRAD2(1)=(2.54*$DETRAD)**2;PCOORD(3,1)=$DIST*2.54;PNORM(3,1)=1.;
PCOORD(3,2)=$(DIST+$DETLNG)*2.54;PNORM(3,2)=1.;

"STEP 5  INITIALIZATION-FOR-AUSGAB"

"STEP 6  DETERMINATION-OF-INCIDENT-PARTICLE-PARAMETERS"
NCASES=1000000;
IXXIN=123456789;
IXX=IXXIN;
IQI=0;  "INCOMING PHOTON"
/XI,YI,ZI/=0.0;
IRI=1;
WTI=1.0;
ISHOW=0;NCCOUN=0;KHUNCT=0;

"STEP 7  SHOWER-CALL"
DO ICASE=1,NCASES
[EHI=0.;NCCOUN=NCCOUN+1;IF(NCCOUN.EQ.100000)[KHUNCT=KHUNCT+1;
  OUTPUT KHUNCT;(1X,I2,' HUNDRED THOUSAND EVENTS');NCCOUN=0;]
"PICK RECOIL PROTON PHI ANGLE, DETERMINE SECTOR"
IFLAG5=0;PHI3=2*PI*RAN(ISEED);IP=.5+PHI3/.3927;IPHI=16-IP;
IF(IPHI.EQ.0)IPHI=16;
"PICK PIO ENERGY IN CM"
E4C=RAN(ISEED)*(E4MAX-E4MIN)+E4MIN;
P4C2=E4C**2-XMPI2;
IF(P4C2.LT.0.)[OUTPUT P4C2;(' P4C2 ',E12.5);P4C2=0.;]
P4C=SQRT(P4C2);
"PICK AZIMUTH ANGLE OF PIO AROUND SUM VECTOR (PX)
  OF PIO AND TARGET PROTON"
PH4X=2*PI*RAN(ISEED);
E5C=EX-E4C;P5C2=E5C**2-XMP2;P5C=SQRT(P5C2);
"FIND ANGLE OF PIO WITH PX"
TH4XAR=(PX**2+P4C2-P5C2)/(2*PX*P4C);
IF(TH4XAR.LT.-1..OR.TH4XAR.GT.1.)[OUTPUT TH4XAR,PX,P4C2,P5C2,P4C;
(' TH4XAR,PX,P4C2,P5C2',/1X,5(1X,E12.5));]
IF(TH4XAR.LT.-1.)TH4XAR=-1.;IF(TH4XAR.GT.1.)TH4XAR=1.;]
TH4X=ACOS(TH4XAR);
PHXC=PHI3+PI;
STX=SIN(TH4X);CTX=COS(TH4X);SPX=SIN(PH4X);CPX=COS(PH4X);
"PREPARE TO ROTATE FROM SUM VECTOR FRAME TO CM FRAME"
CA1=CAF1*SIN(PHXC)*SXC;SA1=SQRT(1-CA1**2);
IF(-COS(PHXC)*SXC.GT.0)SA1=-SA1;
"ROTATE FROM PX TO CM FRAME AND BOOST TO LAB FRAME"
X=P4C*(CA1*CPX*STX+CB1*SA1*SPX*STX+SB1*SA1*CTX);
Y=P4C*(-SA1*CPX*STX+CB1*CA1*SPX*STX+SB1*CA1*CTX);
ZC=P4C*(-SB1*SPX*STX+CB1*CTX);ZL=GB*(ZC+BB*E4C);
"OUTPUT X,Y,ZL;(' PIO X,Y,Z',/1X,3F10.5);"
"FIND PX (SUM VECTOR) COORDS IN CM"
PXX=PX*COS(PHXC)*SXC;PXY=PX*SIN(PHXC)*SXC;PXZ=PX*CTX;

```

```

"FIND TARGET PROTON LENGTH, COORDS, ANGLES IN CM AND LAB"
P5X=PXX-X; P5Y=PXY-Y; P5ZC=PXZ-ZC; P5ZL=GB*(P5ZC+BB*E5C);
P5L=SQRT(P5X**2+P5Y**2+P5ZL**2); P5TH=ACOS(P5ZL/P5L);
P5PH=ATAN2(P5Y, P5X); IF(P5PH.LT.0.) P5PH=P5PH+2*PI;
"DID P5 HIT S2?"
IF(P5TH.GE..06536.AND.P5TH.LE..20339) [IFLAG5=1; IP5=.5+P5PH/.3927;
  IPHI5=16-IP5; IF(IPHI5.EQ.0) IPHI5=16;
  IND=IPHI-IPHI5+16; IPADIF(IND)=IPADIF(IND)+1;
  IPAD(IPHI5)=IPAD(IPHI5)+1;]
"DID P5 HIT A BGO?"
CALL BGOHIT(P5TH, P5PH, IFP5, IBGO);
IF(IFP5.EQ.1) IBGOP5(IBGO)=IBGOP5(IBGO)+1;
"PIO LENGTH AND ANGLES"
P4L=SQRT(X**2+Y**2+ZL**2); TH4L=ACOS(ZL/P4L); PH4L=ATAN2(Y, X);
IF(PH4L.LT.0.) PH4L=PH4L+2*PI;
"LORENTZ PARMS OF PIO REST FRAME"
E4L=SQRT(P4L**2+XMPI2); GPI=E4L/XM4; BPI=SQRT(1-1/GPI**2);
"PICK ANGLES OF GAMMAS IN REST FRAME"
THG1PR=ACOS(-1.+2*RAN(ISEED)); PHG1P=2*PI*RAN(ISEED);
THG2PR=PI-THG1PR; PHG2P=PHG1P+PI; GEN=67.48;
"FIND LAB ANGLES IN ROTATED FRAME (Z ALONG PIO MOM)"
CT1=(COS(THG1PR)+BPI)/(1+BPI*COS(THG1PR));
IF(CT1.GT.1..OR.CT1.LT.-1.) [OUTPUT CT1; (' CT1=', E12.5);
IF(CT1.GT.1.) CT1=1.; IF(CT1.LT.-1.) CT1=-1.;]
ST1=SQRT(1-CT1*CT1);
CT2=(COS(THG2PR)+BPI)/(1+BPI*COS(THG2PR));
IF(CT2.GT.1..OR.CT2.LT.-1.) [OUTPUT CT2; (' CT2=', E12.5);
IF(CT2.GT.1.) CT2=1.; IF(CT2.LT.-1.) CT2=-1.;]
ST2=SQRT(1-CT2*CT2);
SP1=SIN(PHG1P); CP1=COS(PHG1P);
SP2=SIN(PHG2P); CP2=COS(PHG2P);
"FIND LAB ENERGIES"
EG1=GPI*GEN*(1+COS(THG1PR)*BPI);
EG2=GPI*GEN*(1+COS(THG2PR)*BPI);
"EULER ANGLES FOR ROTATION FROM PIO"
CAF2=P4L/SQRT(P4L**2-ZL**2);
CA=CAF2*SIN(TH4L)*SIN(PH4L);
IF(CA.GT.1..OR.CA.LT.-1.) [OUTPUT CA; (' CA=', E12.5);
IF(CA.GT.1.) CA=1.; IF(CA.LT.-1.) CA=-1.;]
SA=SQRT(1-CA*CA); IF(-COS(PH4L)*SIN(TH4L).GT.0.) SA=-SA;
SB=SIN(TH4L); CB=COS(TH4L);
"ROTATE TO REGULAR LAB COORDS"
X1=CA*CP1*ST1+CB*SA*SP1*ST1+SB*SA*CT1;
Y1=-SA*CP1*ST1+CB*CA*SP1*ST1+SB*CA*CT1;
Z1=-SB*SP1*ST1+CB*CT1;
X2=CA*CP2*ST2+CB*SA*SP2*ST2+SB*SA*CT2;
Y2=-SA*CP2*ST2+CB*CA*SP2*ST2+SB*CA*CT2;
Z2=-SB*SP2*ST2+CB*CT2;
"OUTPUT X1, Y1, Z1; (' G1 X, Y, Z', /1X, 3F10.5);
OUTPUT X2, Y2, Z2; (' G2 X, Y, Z', /1X, 3F10.5);"
THG1L=ACOS(Z1); PHG1L=ATAN2(Y1, X1);
IF(PHG1L.LT.0.) PHG1L=PHG1L+2*PI;

```

```

CALL BGOHIT(THG1L,PHG1L,IFG1,IBGO);
IF(IFG1.EQ.1)IBGOG1(IBGO)=IBGOG1(IBGO)+1;
THG2L=ACOS(Z2);PHG2L=ATAN2(Y2,X2);
IF(PHG2L.LT.0.)PHG2L=PHG2L+2*PI;
CALL BGOHIT(THG2L,PHG2L,IFG2,IBGO);
THG1LD=THG1L/DR;PHG1LD=PHG1L/DR;THG2LD=THG2L/DR;PHG2LD=PHG2L/DR;
"OUTPUT THG1LD,PHG1LD,THG2LD,PHG2LD;
(' TH1 PH1',2F9.3,' TH2 PH2',2F9.3);"
"IF(IFG1.EQ.1)[OUTPUT;(' *');]
IF(IFG2.EQ.1)[OUTPUT;(' **');]"
IF(IFG2.EQ.1)IBGOG2(IBGO)=IBGOG2(IBGO)+1;
DO I=1,2 [IF(I.EQ.1)[EI=EG1;UI=X1;YY=Y1;ZZ=Z1;]
ELSE [EI=EG2;UI=X2;YY=Y2;ZZ=Z2;]
VI=CBG*YY+SBG*ZZ;WI=-SBG*YY+CBG*ZZ;THETA=ACOS(WI);
"OUTPUT EI,THETA/DR;(' E=',F9.3,1X,'TH='F9.3);
OUTPUT P4C,P4L,GPI;(' P4C=',F9.3,'P4L=',F9.3,'GPI='F9.3);
OUTPUT X1,Y1,Z1,SBG,CBG;(' XYZSINCOSBG',5F9.4);"
IF(THETA.LE..1882)[IHITBG=IHITBG+1;
CALL SHOWER(IQI,EI,XI,YI,ZI,UI,VI,WI,IRI,WTI);
IF(IFLAG5.EQ.1)IPDH5(IPHIS)=IPDH5(IPHIS)+1;
IBIN=MINO(IFIX(EHIST/BWIDTH+.999),$EBIN);
IF(IBIN.NE.0)EBIN(IBIN)=EBIN(IBIN)+1;]]]

"STEP 8 OUTPUT-OF-RESULTS"
"DO I=1,3 [DO J=1,30 [IENSUM(I)=IENSUM(I)+IENBIN(I,J);]]]"
"DO I=1,31 [A=-3+0.2*(I-1); ENBIN(I)=10**A;]"
BINMAX=0.;DO J=1,$EBIN [BINMAX=MAX(BINMAX,EBIN(J));]
OUTPUT IHITBG;(' MAIN BGO EVENTS',/1X,I7);
OUTPUT (IPDH5(J),J=1,16);(' EVENTS WITH GAMMA IN MAIN BGO',
'AND ALSO P5 IN A PADDLE',/(1X,I5));
OUTPUT (IPAD(J),J=1,16);(' EVENTS WITH P5 IN A PADDLE',
/(1X,I5));
OUTPUT (IPADIF(J),J=1,32);(' IPADIF:',/(1X,I5));
OUTPUT (IBGOG1(J),J=1,4);(' EVENTS IN EACH BGO FROM 1ST GAMMA',
/(1X,I5));
OUTPUT (IBGOG2(J),J=1,4);(' EVENTS IN EACH BGO FROM 2ND GAMMA',
/(1X,I5));
OUTPUT (IBGOP5(J),J=1,4);(' EVENTS IN EACH BGO FROM P5',/(1X,I5));
OUTPUT NCASES,NBGO; (' RESPONSE FUNCTION FOR',
I8,/' PIOS GENERATED AND INCIDENT ON BGO DETECTOR',I1);
DO J=1,48 [LINE(J)=' '];]
DO J=1,$EBIN [ICOL=IFIX(EBIN(J)/BINMAX*48+.999);
LINE(ICOL)='*';
" OUTPUT BWIDTH*J,EBIN(J)/FLOAT(NCASES),LINE;"
" (F10.2,F10.4,48A1); LINE(ICOL)=' '];]"
OUTPUT BWIDTH*J,EBIN(J);
(F10.2,F10.4);]

STOP;
END; "END OF THE MAIN PROGRAMME"

SUBROUTINE HOWFAR;
COMIN/EPCONT,PLADTA,STACK,CYLDTA/;

```

```

IRL=IR(NP);
"OUTPUT IRL,U(NP),V(NP),W(NP),X(NP),Y(NP),Z(NP);(I5/6(2X,F8.5));"
IF(IRL.EQ.4.OR.IRL.EQ.3)[IDISC=1;RETURN;]
ELSEIF(IRL.EQ.1.AND.W(NP).LE.0.)[IDISC=1;RETURN;]
ELSEIF(IRL.EQ.1)[$PLANE1(1,1,IHIT,TVAL);
  IF(IHIT.EQ.0)[IDISC=1;RETURN;]
  RAD=TVAL*SQRT(1-W(NP)**2);
  IF(RAD.GT.$DETRAD*2.54)[$CHGTR(TVAL,3);]
  ELSEIF(RAD.LE.$DETRAD*2.54)[$CHGTR(TVAL,2);];RETURN;]
ELSEIF(IRL.EQ.2)[$PLAN2P(2,4,1,1,1,-1);
  $CYLNDR(1,1,IHIT,TCYL);IF(IHIT.EQ.1)[$CHGTR(TCYL,3);]]
RETURN;
END; "END OF SUBROUTINE HOWFAR"

```

```

SUBROUTINE AUSGAB(IARG);
COMIN/EPCONT/;
COMMON /SCORE/EHIST;
IF(IARG.LE.2 .OR. IARG.EQ.4) [EHIST=EHIST+EDEP;]
RETURN;
END; "END OF SUBROUTINE AUSGAB"

```

```

SUBROUTINE BGOHIT(THET,PHI,IFLAG,IBGO);
IFLAG=0;IBGO=0;IT1=0;IP1=0;IT2=0;IT3=0;IP3=0;IT4=0;IP4=0;
IF(THET.GE..9462.AND.THET.LE.1.3227)IT1=1;
IF(PHI.GE.1.3826.AND.PHI.LE.1.759)IP1=1;
IF(THET.GE.1.7316.AND.THET.LE.2.1081)IT2=1;
IF(THET.GE.1.2927.AND.THET.LE.1.6395)IT3=1;
IF(PHI.GE.4.5390.AND.PHI.LE.4.8858)IP3=1;
IF(THET.GE.2.3548.AND.THET.LE.2.7067)IT4=1;
IF(PHI.GE.4.53645.AND.PHI.LE.4.8883)IP4=1;
IF(IT1*IP1.EQ.1)IBGO=1;IF(IT2*IP1.EQ.1)IBGO=2;
IF(IT3*IP3.EQ.1)IBGO=3;IF(IT4*IP4.EQ.1)IBGO=4;
IF(IBGO.GT.0)IFLAG=1;
RETURN;
END;

```

## APPENDIX C

### The Monte Carlo Program NEUPNAD

This program, which is described in section 4.2.3.8, calculates the momentum and angular distributions of neutrons knocked out of  $^{12}\text{C}$ . The events are weighted by the free pn cross section. The neutron energy has a uniform distribution in the center of mass [Per82b]. Euler transformations are used in the program [Gol80]. Other references are [Per82a] and [BW64].

```
PROGRAM NEUPNAD
DIMENSION W(19)
DATA W/10.,8.,5.2,4.,3.,2.3,2.,1.7,2*1.6,1.8,2.,2.3,
*3.,3.8,5.,6.,8.,10./
COMMON//HMEMOR(80000)
C
CALL HLIMIT(80000)
SUMWT=0.
SUMBG=0.
SUMS2=0.
P1=835.3862
T1=318.
PI=3.1415927
OT=1./3.
XM1=938.28
AMU=931.481
XM2=12*AMU
XM3=11*AMU+10.65
XM4=939.5731
XM5=XM1
XMP2=XM1*XM1
XMN2=XM4*XM4
XM32=XM3*XM3
E1=T1+XM1
DEGRAD=PI/180.
BGANG=-69.
WRITE(6,5)BGANG
5 FORMAT(' NEUTRON PN ADJUSTED MONTE CARLO FOR BGO AT ANGLE',F5.0)
FROT=BGANG*DEGRAD
CF=COS(FROT)
SF=SIN(FROT)
ANGBG=10.78*DEGRAD
```

```

ISEED=1234567
CALL HBOOK1(2,'3B2 PROTON THETA$',36,0.,180.,0.)
CALL HBOOK1(3,'3B3 PROTON PHI$',72,0.,360.,0.)
CALL HBOOK1(4,'3B4 PROTON MOMENTUM$',100,0.,1000.,0.)
CALL HBOOK1(5,'3B5 NEUTRON MOMENTUM$',100,0.,1000.,0.)
CALL HBOOK2(6,'3B6 PROTON THET VS PHI$',72,0.,360.,36,0.,180.,0.)
CALL HBOOK2(7,'3B7 PROTON THET VS MOM$',100,0.,1000.,36,
*0.,180.,0.)
CALL HBOOK2(8,'3B8 PROTON PHI VS MOM$',100,0.,1000.,
*72,0.,360.,0.)
CALL HBOOK2(9,'3B9 PROT MOM VS NEUT MOM$',100,0.,1000.,
*100,0.,1000.,0.)
CALL HBOOK2(10,'3B10 PROT THET VS NEUT MOM$',100,0.,1000.,
*36,0.,180.,0.)
CALL HBOOK2(11,'3B11 PROT PHI VS NEUT MOM$',100,0.,1000.,
*72,0.,360.,0.)
CALL HBOOK2(12,'3B12 PROTON THET VS PHI IN S2$',72,0.,
*360.,20,0.,20.,0.)
CALL HBOOK2(13,'3B13 PROT PHI VS NEU MOM IN S2$',100,0.,
*1000.,72,0.,360.,0.)
NCCOUN=0
DO 100 I=1,1000000
NCCOUN=NCCOUN+1
IF (NCCOUN.EQ.100000) THEN
KHUNCT=KHUNCT+1
WRITE(6,10)KHUNCT
10  FORMAT(1X,I2,' HUNDRED THOUSAND EVENTS')
NCCOUN=0
END IF

C
C  CHOOSE FERMI MOMENTUM
C
fp=51777407.*ran(iseed)
p2=(.75*fp/pi)**ot
P22=P2*P2

C
C  KINEMATICAL QUANTITIES
C
E3=SQRT(P22+XM32)
E2=XM2
EB=E1+E2
ES=SQRT(EB**2-P1**2)
XNB=P1/ES
BB=XNB/GB
TH3=ACOS(-1.+2.*RAN(ISEED))
CTH3=COS(TH3)
STH3=SIN(TH3)
P3=SQRT(E3**2-XM32)
P3PARC=GB*(P3*CTH3-BB*E3)
P3PERP=P3*STH3
P3C2=P3PARC**2+P3PERP**2
P3C=SQRT(P3C2)

```

```

TH3C=ACOS(P3PARC/P3C)
THXC=PI-TH3C
SXC=SIN(THXC)
CXC=COS(THXC)
SB1=SIN(THXC)
CB1=COS(THXC)
E3C=SQRT(P3C2+XM32)
EX=ES-E3C
PX=P3C
XMX2=EX**2-PX**2
C
C FIND ENERGY RANGE OF NEUTRON IN CM
C
E452=XMX2+XMN2-XMP2
E4RG=EX**2+E452**2-XMX2*(E452**2+4*PX*PX*XMN2)
E4RAD=SQRT(E4RG)
E4ONE=(EX*E452+E4RAD)/2/XMX2
E4TWO=(EX*E452-E4RAD)/2/XMX2
IF (E4ONE.GT.E4TWO) THEN
E4MAX=E4ONE
E4MIN=E4TWO
ELSE
E4MAX=E4TWO
E4MIN=E4ONE
END IF
PHI3=2*PI*RAN(ISEED)
C
C CHOOSE NEUTRON CM ENERGY WITH A UNIFORM DISTRIBUTION
C
E4C=RAN(ISEED)*(E4MAX-E4MIN)+E4MIN
P4C2=E4C**2-XMN2
IF (P4C2.LT.0.) THEN
WRITE(6,20)P4C2
20  FORMAT(' P4C2 ',E12.5)
P4C2=0.
END IF
P4C=SQRT(P4C2)
C
C PICK PHI ANGLE AROUND PX, THE SUM OF NEUTRON AND PROTON CM MOMENTA
C
PH4X=2*PI*RAN(ISEED)
E5C=EX-E4C
P5C2=E5C**2-XMP2
TH4XAR=(PX**2+P4C2-P5C2)/(2*PX*P4C)
IF (TH4XAR.LT.-1..OR.TH4XAR.GT.1.) THEN
WRITE(6,30)TH4XAR,PX,P4C2,P5C2,P4C
30  FORMAT(' TH4XAR,PX,P4C2,P5C2',/1X,5(1X,E12.5))
IF(TH4XAR.LT.-1.)TH4XAR=-1.
IF(TH4XAR.GT.1.)TH4XAR=1.
END IF
TH4X=ACOS(TH4XAR)
PHXC=PHI3+PI

```

```

      STX=SIN(TH4X)
      CTX=COS(TH4X)
      SPX=SIN(PH4X)
      CPX=COS(PH4X)
      if(p3perp.ne.0.)go to 40
      x=p4c*stx*cpx
      y=p4c*stx*spx
      zc=p4c*ctx
      go to 70
C
C  FIND CM NEUTRON MOMENTUM COORDS USING EULER TRANSFORMATION
C
40  caf1=px/p3perp
      CA1=CAF1*SIN(PHXC)*SXC
      SARG=1.-CA1**2
      IF(SARG.GE.0)GO TO 60
      WRITE(6,50)SARG
50  FORMAT(1X,'SARG= ',E12.5)
      SARG=0.
60  CONTINUE
      SA1=SQRT(SARG)
      IF(-COS(PHXC)*SXC.GT.0)SA1=-SA1
      X=P4C*(CA1*CPX*STX+CB1*SA1*SPX*STX+SB1*SA1*CTX)
      Y=P4C*(-SA1*CPX*STX+CB1*CA1*SPX*STX+SB1*CA1*CTX)
      ZC=P4C*(-SB1*SPX*STX+CB1*CTX)
70  ZL=GB*(ZC+BB*E4C)
      PXX=PX*COS(PHXC)*SXC
      PXY=PX*SIN(PHXC)*SXC
      PXZ=PX*CXC
      P5X=PXX-X
      P5Y=PXY-Y
      P5ZC=PXZ-ZC
      P5ZL=GB*(P5ZC+BB*E5C)
      P5L2=P5X**2+P5Y**2+P5ZL**2
      P5L=SQRT(P5L2)
      E5L=SQRT(P5L2+XMP2)
      P5TH=ACOS(P5ZL/P5L)
      P5PH=ATAN2(P5Y,P5X)
      IF(P5PH.LT.0.)P5PH=P5PH+2*PI
      PHI2=PHI3+PI
      TH2=PI-TH3
      P2X=P2*COS(PHI2)*SIN(TH2)
      P2Y=P2*SIN(TH2)*SIN(PHI2)
      P2Z=P2*CTH2
C
C  TOTAL MOMENTUM VECTOR
C
      PTZ=P2Z+P1
      PT=SQRT(PTZ**2+P2X**2+P2Y**2)
      THTOT=ACOS(PTZ/PT)
C
C  CM FRAME LORENTZ PARAMETERS

```

```

C
  BETA=PT/EB
  GAM=1/SQRT(1.-BETA**2)
C
C EULER ANGLES FOR ROTATION
C
  P=PHI2-PI/2.
  T=-THTOT
  SP=SIN(P)
  CP=COS(P)
  ST=SIN(T)
  CT=COS(T)
C
C ROTATE INITIAL PROTON MOMENTUM AND BOOST TO CM
C
  P1YRL=ST*P1
  P1ZRL=CT*P1
  P1ZRC=GAM*(P1ZRL-BETA*E1L)
  P1C2=P1YRL**2+P1ZRC**2
  P1C=SQRT(P1C2)
C
C ROTATE FINAL PROTON MOMENTUM AND BOOST TO CM
C
  P5XRL=CP*P5X+SP*P5Y
  P5YRL=-CT*SP*P5X+CT*CP*P5Y+ST*P5Z
  P5ZRL=ST*SP*P5X-ST*CP*P5Y+CT*P5Z
  P5ZRC=GAM*(P5ZRL-BETA*E5L)
  P5C2=P5XRL**2+P5YRL**2+P5ZRC**2
  P5C=SQRT(P5C2)
C
C FIND ANGLE BETWEEN INITIAL AND FINAL PROTON MOMENTUM
C
  DOT=P1YRL*P5YRL+P1ZRC*P5ZRC
  THPN=ACOS(DOT/P1C/P5C)*RADDEG
  IF(THPN.NE.180.)GO TO 80
  WT=W(19)
  GO TO 90
80  IA=THPN/10.
  IB=IA+1
C
C ASSIGN WEIGHT FROM PN CROSS SECTION
C
  WT=(THPN/10.-IA)*(W(IB)-W(IA))+W(IA)
90  CONTINUE
  SUMWT=SUMWT+WT
  P4L=SQRT(X**2+Y**2+ZL**2)
  THETA1=P5TH*RADDEG
  PHI1=P5PH*RADDEG
  TH4L=ACOS(ZL/P4L)
  PH4L=ATAN2(Y,X)
  E4L=SQRT(P4L**2+XMPI2)
C

```

C ROTATE NEUTRON SO Z AXIS POINTS TO BGO

C

```
P4BGZ=-SF*Y+CF*ZL
THBG=ACOS(P4BGZ/P4L)
IF(THBG.GT.ANGBG) GO TO 100
SUMBG=SUMBG+WT
CALL HFILL(2,THETA1,YDUM,WT)
CALL HFILL(3,PHI1,YDUM,WT)
CALL HFILL(4,P5L,YDUM,WT)
CALL HFILL(5,P4L,YDUM,WT)
CALL HFILL(6,PHI1,THETA1,WT)
CALL HFILL(7,P5L,THETA1,WT)
CALL HFILL(8,P5L,PHI1,WT)
CALL HFILL(9,P4L,P5L,WT)
CALL HFILL(10,P4L,THETA1,WT)
CALL HFILL(11,P4L,PHI1,WT)
IF(THETA1.GE.3.7.AND.THETA1.LE.11.7)CALL HFILL(12,PHI1,THETA1,WT)
IF(THETA1.GE.3.7.AND.THETA1.LE.11.7)CALL HFILL(13,P4L,PHI1,WT)
IF(THETA1.GE.3.7.AND.THETA1.LE.11.7)SUMS2=SUMS2+WT
100 CONTINUE
WRITE(6,110)SUMWT,SUMBG,SUMS2
110 FORMAT(' SUMWT=',F15.3,/1X,'SUMBG=',F15.3,/1X,'SUMS2=',F15.3)
CALL HSTORE(0,10)
CALL HINDEX
STOP
END
```

## APPENDIX D

Tables of Asymmetries Measured

BGO	$\phi_p$	Normal 1985		Sideways 1985		Longitudinal 1986		Normal 1986	
		asym	error	asym	error	asym	error	asym	error
BGO 1	0	-14.94	11.05	-3.65	5.57				
	45	-9.88	11.42	8.18	6.47				
	90	-11.18	10.99	15.55	8.72				
	135	-1.26	9.44	1.07	6.65				
	180	-19.90	8.40	1.67	5.72				
	225	-34.96	9.76	11.45	7.00				
	270	-7.06	15.16	12.27	7.28				
	315	-13.22	8.91	-1.26	6.55				
BGO 2	0	0.44	3.89	2.69	5.49	-4.36	3.79	13.85	6.07
	45	6.70	4.78	0.08	7.62	1.23	5.08	1.66	9.08
	90	13.03	5.25	0.93	7.77	-2.17	6.04	28.41	11.08
	135	-6.63	4.26	3.24	5.11	-11.39	4.22	-1.18	8.34
	180	-3.02	3.49	2.92	4.21	-0.95	3.62	3.26	7.20
	225	-7.41	4.13	2.25	5.12	7.68	4.34	11.43	7.84
	270	2.95	4.74	12.80	6.45	6.64	5.52	8.09	9.12
	315	6.37	4.40	10.91	6.63	-1.34	4.30	9.76	7.43
BGO 3	0	4.30	5.02	5.23	3.74	-8.23	6.00		
	45	-3.13	5.90	-0.18	4.64	-8.34	9.00		
	90	4.44	7.72	-1.43	5.49	-20.50	11.47		
	135	-1.75	5.96	3.56	4.19	-9.60	9.72		
	180	-5.03	4.73	5.68	3.37	-0.64	6.35		
	225	-8.44	5.96	4.41	3.83	-6.36	7.64		
	270	-2.18	7.97	15.61	5.11	-4.33	12.58		
	315	2.57	5.89	10.15	4.01	-6.77	7.88		
BGO 4	0	1.24	4.43	3.06	3.21	8.40	5.84	6.97	6.76
	45	-7.75	5.22	6.42	3.64	4.73	6.53	18.73	7.83
	90	-9.44	6.37	-1.52	4.15	-12.58	8.13	8.06	8.35
	135	-10.62	5.63	2.58	3.86	-9.28	7.84	-2.52	8.65
	180	-5.13	5.01	3.83	3.59	1.75	6.78	-5.61	7.86
	225	2.53	5.82	7.07	3.73	-11.66	7.19	1.68	7.98
	270	2.47	6.23	5.88	4.10	-9.29	7.88	9.99	7.58
	315	1.92	4.91	4.49	3.35	0.79	5.76	2.87	6.86

Table D-1: These are the asymmetries or coincidence analyzing powers measured in the experiment.

BGO	$\phi_p$	Normal 1985		Sideways 1985		Longitudinal 1986		Normal 1986	
		asym	error	asym	error	asym	error	asym	error
BGO 1	0	-14.94	11.05	-3.65	5.57				
	45	-11.79	6.86	4.69	4.54				
	90	-9.37	9.02	0.42	5.55				
	135	-18.14	6.91	-5.15	4.77				
	180	-19.90	8.40	1.67	5.72				
BGO 2	0	0.44	3.89	2.69	5.49	-4.36	3.79	13.85	6.07
	45	6.54	3.23	-5.86	4.95	1.29	3.26	6.30	5.76
	90	7.72	3.47	-6.51	4.91	-4.60	4.04	16.73	7.01
	135	-7.03	2.94	0.49	3.53	-9.51	2.99	5.66	5.64
	180	-3.02	3.49	2.92	4.21	-0.95	3.62	3.26	7.20
BGO 3	0	4.30	5.02	5.23	3.74	-8.23	6.00		
	45	-0.17	4.14	-5.56	2.93	-0.17	5.91		
	90	1.05	5.52	-8.82	3.66	-8.80	8.47		
	135	-5.17	4.22	-0.62	2.71	-0.52	6.01		
	180	-5.03	4.73	5.68	3.37	-0.64	6.35		
BGO 4	0	1.24	4.43	3.06	3.21	8.40	5.84	6.97	6.76
	45	-2.75	3.53	0.64	2.33	1.78	4.30	9.90	5.18
	90	-3.25	4.43	-3.76	2.80	-1.26	5.63	9.10	5.56
	135	-3.84	4.05	-2.39	2.56	1.98	5.28	-0.25	5.82
	180	-5.13	5.01	3.83	3.59	1.75	6.78	-5.61	7.86
BGO A	0	10.17	4.63	-0.89	4.80				
	45	12.34	3.82	-5.28	4.02				
	90	8.54	4.84	-0.81	4.64				
	135	2.38	3.73	3.94	3.79				
	180	5.96	5.80	3.52	4.64				

Table D-2: These are the parity-combined asymmetries or coincidence analyzing powers measured in the experiment (except that the points for  $0^\circ$  and  $180^\circ$  are not combined). BGO A is a composite of BGO's 1 and 2 as described in the text.

## References

- [Ajz85] F. Ajzenberg-Selove. *Nuclear Physics A*433:1, 1985.
- [Ama82] R.D. Amado. *Phys. Rev. C*26:270, 1982.
- [AR] R.A. Arndt and L.S. Roper. code SAID, unpublished.
- [BBB\*89] J.A. Bakken, L. Barone, J.J. Blaising, T. Boehringer, B. Borgia, D. Boutigny, J.P. Burq, M. Chemarin, R. Clare, G. Coignet, P. Denes, D. de Notaristefani, M. Diemoz, C. Dionisi, H. Elmamouni, P. Extermann, S. Falciano, F. Ferroni, G. Gratta, B. Ille, P. Kaaret, Y. Karyotakis, P. Klok, P. Lebrun, P. Lecoq, P.J. Li, E. Longo, D. Luckey, L. Luminari, M. Maire, J.P. Martin, M. Micke, U. Micke, G. Morand, S. Morganti, J. Ossmann, P.A. Piroue, C. Rondinini, W. Ruckstuhl, G. Sauvage, T.P. Schaad, D. Schmitz, M. Schneegans, D.P. Stickland, R.L. Sumner, C. Taylor, E. Valente, M. Vivargent, L. Vuilleumier, W. Walk, R. Weil, and T. Wynen. *Nuclear Instruments and Methods in Physics Research A*280:25, 1989.
- [BIPL] R. Brun, I. Ivanchenko, P. Palazzi, and D. Lienart. HBOOK Users Guide. Data Handling Division, CERN, CH 1211, Geneva 23, Switzerland; HFIT is a modified form of the fitting program from MINUIT, by F. James and M. Roos.
- [BW64] D. Blumenthal and C. Watson. 1964. SREL Handbook.
- [CG52] G.F. Chew and M.L. Goldberg. *Phys. Rev.*, 87:778, 1952.
- [CK65] S. Cohen and D. Kurath. *Nuclear Physics*, 73:1, 1965.
- [CMF\*82] J.R. Comfort, G.L. Moake, C.C. Foster, P. Schwandt, and W.G. Love. *Phys. Rev. C*26:1800, 1982.
- [FH74] H. Frauenfelder and E.M. Henley. *Subatomic Physics*. Prentice Hall, Inc., Englewood Cliffs, N.J., 1974.
- [FL85] M.A. Franey and W.G. Love. *Phys. Rev. C*31:488, 1985.
- [FWA\*87] D. Frekers, S.S.M. Wong, R.E. Azuma, T.E. Drake, J.D. King, L. Buchmann, R. Schubank, R. Abegg, K.P. Jackson, C.A. Miller, S. Yen, W.P. Alford, R.L. Helmer, C. Broude, S. Mattsson, and E. Rost. *Phys. Rev. C*35:2236, 1987.
- [Gol80] H. Goldstein. *Classical Mechanics*. Addison-Wesley Publishing Co., Reading, Massachusetts, second edition, 1980.
- [HAC\*88] K.H. Hicks, R. Abegg, A. Celler, R.S. Henderson, O. Hausser, N.W. Hill, K.P. Jackson, R.G. Jeppesen, N.S.P. King, M.A. Kovash, R. Liljestrang, C.A. Miller, G.L. Morgan, J.R. Shepard, A. Trudel, M. Vetterli, and S. Yen. *Phys. Rev. Lett.*, 61:1174, 1988.

- [HHA\*88] K.H. Hicks, O. Hausser, R. Abegg, W.P. Alford, A. Celler, R.L. Helmer, R.S. Henderson, K.P. Jackson, J. Lisantti, C.A. Miller, R. Sawafta, J.R. Shepard, and S. Yen. *Physics Letters B* 201:29, 1988.
- [Hic88] K.H. Hicks. Spin-Observables for the ( $\bar{p}, p'\gamma$ ) Reaction at 400 MeV. In Horowitz, Goodman, and Walker, editors, *Spin Observables of Nuclear Probes*, Plenum, New York, 1988.
- [HJL\*88] K.H. Hicks, R.G. Jeppesen, C.C.K. Lin, K.P. Jackson R. Abegg, O. Hausser, J. Lisantti, C.A. Miller, R. Sawafta E. Rost, M.C. Vetterli, and S. Yen. *Phys. Rev. C* 38:229, 1988.
- [HLAK83] O. Hausser, M.A. Lone, T.K. Alexander, and S.A. Kushneriuk. *Nuclear Instruments and Methods*, 213:301, 1983.
- [Hor85] C.J. Horowitz. *Phys. Rev. C* 31:1340, 1985.
- [Joy82] D. Joyce. *Positive Pion Scattering on  $^{24}\text{Mg}$* . PhD thesis, The College of William and Mary, 1982.
- [LF81] W.G. Love and M.A. Franey. *Phys. Rev. C* 24:1073, 1981.
- [LK80] T.-S.H. Lee and D. Kurath. *Phys. Rev. C* 21:293, 1980.
- [LM70] W.O. Lock and D.F. Measday. *Intermediate Energy Nuclear Physics*. Melthuen & Co. Ltd., London, 1970.
- [LM85] B.J. Lieb and J.R. Mackenzie. 1985. unpublished.
- [MSW83] J.A. McNeil, J.R. Shepard, and S.J. Wallace. *Phys. Rev. Lett.*, 50:1439, 1983.
- [MWZ86] N. Mobed, S.S.M. Wong, and X. Zhu. *Nuclear Physics A* 456:644, 1986.
- [NHR85] W.R. Nelson, H. Hirayama, and D.W.O. Rogers. *The EGS4 Code System*. Technical Report 265, SLAC, 1985.
- [Ohl72] G.G. Ohlsen. *Rep. Prog. Phys.*, 35:717, 1972.
- [PAS85] J. Piekarewicz, R.D. Amado, and D.A. Sparrow. *Phys. Rev. C* 32:949, 1985.
- [Per82a] C.F. Perdrisat. *Cinematique Relativistique et son Application aux Reactions Nucleaires*. Technical Report, l'Institute de Physique Nucleaire, Orsay, 1982.
- [Per82b] D.H. Perkins. *Introduction to High Energy Physics*. Addison-Wesley Publishing Co., Reading, Massachusetts, second edition, 1982.
- [PFTV86] W.H. Press, B.P. Flannery, S.A. Teukolsky, and W.T. Vetterling. *Numerical Recipes*. Cambridge University Press, Cambridge, 1986.
- [Pie89] J. Piekarewicz. 1989. private communication.
- [PRS90] J. Piekarewicz, E. Rost, and J.R. Shepard. *Phys. Rev. C* 41:2277, 1990.
- [Ros] E. Rost. code DREX, unpublished.

- [RS77] J. Raynal and R. Schaeffer. 1977. Computer code DW81, a version of DWBA70 modified by J.R. Comfort, unpublished; Computer code DWBA70, J. Raynal and R. Schaeffer, unpublished.
- [RS87] E. Rost and J.R. Shepard. *Phys. Rev. C***35**:681, 1987.
- [RT67] L.S. Rodberg and R.M. Thaler. *Introduction to The Quantum Theory of Scattering*. Academic Press, New York, 1967.
- [Sat80] G.R. Satchler. *Introduction to Nuclear Reactions*. John Wiley & Sons, 1980.
- [She] J.R. Shepard. code ACOR, unpublished.
- [SMW83] J.R. Shepard, J.A. McNeil, and S.J. Wallace. *Phys. Rev. Lett.*, 50:1443, 1983.
- [SRP84] J.R. Shepard, E. Rost, and J. Piekarewicz. *Phys. Rev. C***30**:1604, 1984.
- [vD90] O.B. van Dyck. 1990. private communication (LAMPF).
- [Wol56] L. Wolfenstein. "Polarization of Fast Nucleons." In *Annual Review of Nuclear Science*, Annual Reviews, Inc., Palo Alto, California, 1956.

## VITA

### Christopher Robinson Lyndon

Born in the U.S. zone in Panama, November 27, 1950. Graduated from Langley High School in McLean, Virginia, June 1968. B.S. from the College of William and Mary in mathematics in May 1976. Entered the graduate physics program of the College of William and Mary in January 1984.